UNIVERSITÀ DEGLI STUDI DI TRIESTE

UNIVERSITÀ DEGLI STUDI DI TRIESTE

XXXVI CICLO DEL DOTTORATO DI RICERCA IN

NANOTECNOLOGIE

Borsa finanziata dal Dipartimento di Fisica su fondi CERIC-ERIC

ADVANCED APPROACHES TO INVESTIGATE IMMUNE AND REPRODUCTIVE TOXICITY OF NANOPLASTICS

Settore scientifico-disciplinare: FIS07/BIO10

DOTTORANDA
FEDERICA ZINGARO

COORDINATORE
PROF. ALBERTO MORGANTE

SUPERVISORI DI TESI
Dr. ALESSANDRA GIANONCELLI
Dr. LORELLA PASCOLO

ANNO ACCADEMICO 2022/2023

TABLE OF CONTENTS

ABSTRACT (En)

Although the significant and novel applications offered by the scientific advance in nanotechnology, there is an urgent need to shed a light on the possible harmful effects of general exposure to nanomaterials.

To this aim, my Ph.D. research contributed to this branch by investigating the toxicological accumulation of polymeric nanoparticles distributed in the environment in two cell line models, representative of the immune and the reproductive systems. Different physiochemical properties may influence the nanomaterials' toxicity outcomes, and this work was conceived to unravel the effects of a new persistent environmental pollutant: nanoplastics on human health. It was worth noting that it has been recently demonstrated that polymer-based nanoparticles might induce macromolecular homeostasis impairment.

The research activity was carried out using advanced, synchrotron-based X-ray microscopy and fluorescence (μXRM, and XRF), together with Fourier Transform Infrared micro-spectroscopy (FTIR) and imaging, conventional techniques (light fluorescence microscopy), and laboratory tests (cell viability, lipid staining).

We performed imaging based and spectroscopic analyses by using Scanning Transmission X-ray Microscopy (STXM) coupled with Low-Energy X-ray Fluorescence (LEXRF), and FTIR techniques operating at TwinMic and Chem-SISSI beamlines, Elettra Synchrotron Trieste, Italy, respectively. The aim was to set up both a model of environmental nanoplastics and an *in vitro* model, monocytes-activated-macrophages (THP-1 cell line) to investigate the toxicity in the immune system when cells were exposed to representative experimental concentrations of cadmium selenide quantum dots (CdSe-QDs) labelled polypropylene, and polyvinyl chloride nanoplastics (PP-, PVC-NPs), a novel model chemically synthetized and characterised by the Joint Research Centre (JRC), Ispra, Italy.

Although the cell viability was not significantly compromised by the experimental concentrations and time exposure conditions, nanoplastics were responsible for the morphological and lipid metabolism alterations in macrophages.

LEXRF mode allowed to track the selenium L-line of the CdSe-QDs, labelling nanoplastics, by exciting the specimen at 1.7 keV energy, a compromise to visualise the Se distribution map, and other low-Z elements. The analyses permitted to follow the

NPs across the cells at sub-micron spatial resolution, whose localisation was in good agreement with the light fluorescence microscopy, and provided the cell status interpretation of Na, C, O, Mg elemental maps.

The macrophages (phenotype M1) treated with polypropylene and polyvinyl chloride, compared to the control, showed a severe morphological alteration, visible through absorption and phase contrast images and it was clearly related to the nanoparticles' phagocytosis. This study also found out that nanoplastics exposure caused an increase of lipid droplet contents in the form of bright vesicles in imaging techniques, a hallmark of macrophagic activation and oxidative stress. These results were confirmed by performing a laboratory staining test for lipid droplets in all the treatment conditions.

The results obtained with this multidisciplinary approach allowed to pave the way for a deeper understanding of the toxicological accumulation of a rising nanopollutant in human cell models.

An additional experiment was performed at ID21 beamline, European Synchrotron Radiation Facility (ESRF), Grenoble, France, operating at an energy range complementary to that of TwinMic beamline. The XRF microscope operated at an energy suitable to excite the Cd L-line for PVC-NPs visualisation in ovarian cell line (SK-OV-3). Interestingly, these results highlighted the co-localisation of Cd (QDs), and chloride (NPs) at nanometric resolution. According to the concentration used for the specimens, it seemed that lower concentration of nanoplastics were prone to accumulate at the plasma membrane, by contrast higher amount at the intracellular level. This evidence is beyond significant to deeper investigate the capability of ovarian cells to interact with nanoplastics, leading to possible consequent effects for the reproductive medicine.

To develop other synthetic skills handling nanomaterials, in accordance with my supervisors, I spent part of my research activity at the Department of Chemical Sciences, Dublin, Ireland as part of Silvia Giordani's research team, in the frame of Doctor Europeus. During these months, I synthetised an alternative model for polypropylene nanoplastics for our analyses, by producing a green, fluorescent probe: carbon dots. Thus, carbon dots were synthetised by a top-down approach and fully characterised before the labelling to the nanoplastics trough the oil-in-water emulsion technique. The as-produced products will be further characterised (Transmission Electron Microscopy, Attenuated Transmission Reflectance micro-spectroscopy) to be utilised in *in vitro* cell lines as an alternative and good biocompatible nanoplastics model.

ABSTRACT (It)

Nonostante le significative e nuove applicazioni offerte dal progresso scientifico delle nanotecnologie, è urgente fare luce sui possibili effetti nocivi dell'esposizione generale ai nanomateriali.

A questo scopo, la mia ricerca di dottorato ha contribuito in questo settore studiando l'accumulo tossicologico di nanoparticelle polimeriche distribuite nell'ambiente in due modelli di linea cellulare, rappresentativi del sistema immunitario e di quello riproduttivo. Le diverse proprietà fisico-chimiche possono influenzare gli effetti della tossicità dei nanomateriali e questo lavoro è stato concepito per svelare gli effetti sulla salute umana di un nuovo inquinante ambientale persistente: le nanoplastiche. È stato dimostrato di recente che le nanoparticelle a base di polimeri possono indurre un'alterazione dell'omeostasi macromolecolare.

L'attività di ricerca è stata condotta utilizzando la microscopia a raggi X e la fluorescenza (μXRM e XRF) avanzate, con luce di sincrotrone, insieme alla micro-spettroscopia e all'imaging FTIR (Fourier Transform Infrared microspectroscopy), a tecniche convenzionali (microscopia a fluorescenza) e a test di laboratorio (vitalità cellulare, colorazione lipidica).

Abbiamo eseguito analisi di imaging e spettroscopiche utilizzando tecniche STXM (Scanning Transmission X-ray Microscopy) accoppiate a LEXRF (Low-Energy X-ray Fluorescence) e FTIR rispettivamente presso le linee di luce a TwinMic e Chem-SISSI, Elettra Sincrotrone Trieste, Italia. L'obiettivo è stato quello di sintetizzare sia un modello di nanoplastica ambientale sia un modello *in vitro*, monociti attivati in macrofagi (linea cellulare THP-1), per studiare la tossicità sul sistema immunitario quando le cellule sono state esposte a concentrazioni sperimentali rappresentative di polipropilene e cloruro di polivinile marcate con quantum dots di cadmio selenuro (CdSe-QDs PP-NPs, CdSe-QDs PVC-NPs), un nuovo modello sintetizzato e caratterizzato dal Joint Research Centre (JRC), Ispra, Italia.

Sebbene la vitalità cellulare non sia stata significativamente compromessa dalle concentrazioni sperimentali e dalle condizioni di esposizione temporale, le nanoplastiche hanno indotto delle alterazioni morfologiche e del metabolismo lipidico nei macrofagi.

La modalità di fluorescenza a raggi X a bassa energia ha permesso di tracciare la linea L del selenio dei CdSe-QDs, legati alle nanoplastiche, eccitando il campione a

un'energia di 1,7 keV, un compromesso per visualizzare la mappa di distribuzione del Se, e altri elementi a basso peso atomico. Le analisi hanno permesso di seguire le NPs attraverso le cellule con una risoluzione spaziale sub-micrometrica, la cui localizzazione era in buon accordo con la microscopia a fluorescenza ottica, e hanno fornito l'interpretazione dello stato cellulare delle mappe elementari di Na, C, O, Mg.

I macrofagi (fenotipo M1) trattati con polipropilene e cloruro di polivinile, rispetto al controllo, hanno mostrato una grave alterazione morfologica, visibile attraverso immagini di assorbimento e contrasto di fase, chiaramente correlata alla fagocitosi delle nanoparticelle. Questo studio ha anche scoperto che l'esposizione alle nanoparticelle ha causato un aumento del contenuto di gocce lipidiche sotto forma di vescicole bianche nelle tecniche di imaging, un segno distintivo dell'attivazione dei macrofagi e dello stress ossidativo. Questi risultati sono stati confermati eseguendo un test di colorazione di laboratorio per le goccioline lipidiche in tutte le condizioni di trattamento.

I risultati ottenuti con questo approccio multidisciplinare permettono di fare luce ad una comprensione più profonda dell'accumulo tossicologico dei nano inquinanti emergenti in modelli cellulari umani.

Un esperimento addizionale è stato effettuato presso la linea di fascio ID21, ESRF, Grenoble, Francia, che copre un range energetico complementare a quello di TwinMic. Il microscopio XRF è stato settato ad un'energia adatta ad eccitare la linea L del Cd per la visualizzazione delle PVC-NPs nella linea cellulare ovarica (SK-OV-3). È interessante notare che questi risultati hanno evidenziato la co-localizzazione di Cd (QDs) e cloruro (NPs) a risoluzione nanometrica. In base alla concentrazione utilizzata per i campioni, sembrava che le nanoplastiche a bassa concentrazione fossero inclini ad accumularsi a livello della membrana plasmatica, mentre ad una quantità maggiore a livello intracellulare. Questa evidenza è oltremodo significativa per approfondire la capacità delle cellule ovariche di interagire con le nanoplastiche, portando a possibili effetti conseguenti per la medicina riproduttiva.

Per sviluppare altre competenze sintetiche relative ai nanomateriali, in accordo con i miei supervisori, ho trascorso parte della mia attività di ricerca presso il Dipartimento di Scienze Chimiche di Dublino, in Irlanda, come parte del gruppo di ricerca guidato dalla Professoressa Silvia Giordani, nell'ambito del Dottorato Europeo. Durante questi mesi, ho sintetizzato un modello alternativo per le nanoplastiche di polipropilene per le nostre analisi, producendo una sonda verde e fluorescente: i carbon dots. Questi ultimi sono stati sintetizzati con un approccio top-down e caratterizzati completamente prima

della marcatura delle nanoplastiche attraverso la tecnica dell'emulsione olio-acqua. I prodotti così ottenuti saranno ulteriormente caratterizzati (Transmission Electron Microscopy, Attenuated Transmission Reflectance micro-scpectroscopy) per essere utilizzati in linee cellulari *in vitro* come modello alternativo e più biocompatibile di nanoplastica.

ACKNOWLEDGMENTS

This Ph.D. work has been supported by the Central European Infrastructure Consortium (CERIC) in the frame of Integra's Project. CERIC is a research infrastructure integrating and providing open access to facilities in Europe to help science and industry advance in the fields of materials, biomaterials and nanotechnology.

At this point of my Ph.D. journey, I would like to thank my supervisors, Dr. Alessandra Gianoncelli and Dr. Lorella Pascolo, for supporting and guiding me in the research activity, allowing me to enrich my scientific knowledge with their multidisciplinary backgrounds.

I would like to acknowledge Dr. Chiara Agostinis, for the biological skills she taught me at the Dipartimento Scienze della Vita, University of Trieste, thanks to the hospitality of Prof. Roberta Bulla.

Thanks to Dr. Giacomo Ceccone, Dr. Domenico Cassano, Dr. Rita La Spina at the Joint Research Centre (JRC), Ispra, Italy for their constant support with the experimental part discussed in Chapter 2.

I am thankful to Dr. Paola Storici for allowing me to use the Structural Biology Laboratoy at Elettra Sincrotrone Trieste, during the cell sample preparation and all the colleagues.

My gratitude goes to Dr. Fulvio Celsi for the support in the fluorescence microscope analysis, and Prof. Giuseppe Ricci for the possibility to attend the IRCCS Burlo Garofolo Trieste, when needed, during the three years.

The multidisciplinary research activity in Nanotechnology included brilliant experts and researchers from several institutions.

Thanks to Dr. Giovanni Birarda for contributing to the studies conducted at the Chem-SISSI beamline and Dr. Valentina Bonanni at TwinMic beamline at Elettra Sincrotrone Trieste.

In the frame of CERIC proposals, I would like to thank Dr. Iva Božičević Mihalić and Dr. Georgios Provatas for supervising me during the month spent at the Laboratory for ion beam interactions at the Ruđer Bošković Institut, Zagreb, Croatia and for contributing to obtain Particle Induced X-ray Emission (PIXE) results shown in Appendix A1.

Thanks also to Dr. Francesco D'Amico (IUVS Beamline, Elettra Sincrotrone Trieste) for the preliminary analyses of Raman Spectroscopy shown in Appendix B1.

I am beyond grateful to have had the possibility to join the Professor Silvia Giordani's group at the Department of Chemical Sciences, Dublin City University, Ireland for the title of Doctor Europeus. I am grateful for that part of research activity discussed in Chapter 3, which shaped me both academically and personally. Thanks to the team members, Hugh Mohan, and Michal Bartkowksi.

I would like to acknowledge Barbara Vergani at the Milano Bicocca University, Italy for carrying out Transmission Electron Microscopy (TEM) measurements.

To conclude, thanks to whoever taught me something useful during this time and to my family, and friends who never stopped cheering me up.

CHAPTER 1 – GENERAL INTRODUCTION

1.1 Nanotoxicology: the dark side of Nanotechnology

Nanotechnology refers to a multidisciplinary field of science, which deals with and manipulates matter at nano scale aiming at providing revolutionary and beneficial approaches or solutions to a wide range of health, environmental and electronic applications [1].

The modern nanotechnology's pioneer is the physicist Richard Feynman, Nobel Prize for Physics in 1965, who presented a brilliant lecture titled *"There's Plenty of Room at the Bottom"* during the American Physical meeting at the California Institute of Technology, Pasadena in 1959. This outstanding idea paved the way for novel ways of thinking in nanoscience.

Fifteen years after Feynman's lecture, Norio Taniguchi, a Japanese scientist, coined for the first time the term "nanotechnology" to describe semiconductor processes which occurred at nanometre scale. He promoted the idea of nanotechnology as the process, separation, consolidation, and deformation of materials by a single atom or molecule [2].

In 1986, K. Eric Drexler introduced the concept of molecular technology in his book titled *"Engines of Creation: The Coming Era of Nanotechnology"*, in which he proposed the use of nanoscale "assemblers", capable of moving and precisely positioning or arranging atoms by producing almost anything existing in nature [3].

In the 21st century, nanotechnology still represents an expanding and promising group of technologies useful for multiple applications. It encompasses a several number of methods, techniques, and processes, including X-ray fluorescence microscopy, atomic force microscopy, lithography, transmission-, and scanning- electron microscopy, chemical vapor deposition [4].

According to the European Food Safety Authority, *"Nanotechnology is a field of applied sciences and technologies involving the control of matter at the atomic and molecular scale, normally below 100 nanometres. Nanomaterials may exhibit different physical and chemical properties compared with the same substances at normal scale,*

such as increased chemical reactivity due to greater surface area; or in the United States, the National Nanotechnology Initiative (NNI) defines Nanotechnology as *"a science, engineering, and technology conducted at the nanoscale (1 to 100 nm), where unique phenomena enable novel applications in a wide range of fields, from chemistry, physics and biology, to medicine, engineering and electronics"* [5].

There are two approaches to nanoscale in nanotechnology: a) the **"top-down"** way, starts from a bulk material which is reduced to form nanosized components; by contrast, b) the **"bottom-up"** approach, involves the assembling process of nanoscopic molecules and atoms, to build a larger structure. Nanomaterials (NMs) are characterised by physiochemical properties, which are different from their bulk components, illustrated in Figure 1.

Nanomaterials are defined as materials with at least one of their dimensions in the range of 1 to 100 nm, and their properties can be precisely controlled to obtain engineered nanomaterials with outstanding practical applications [6].

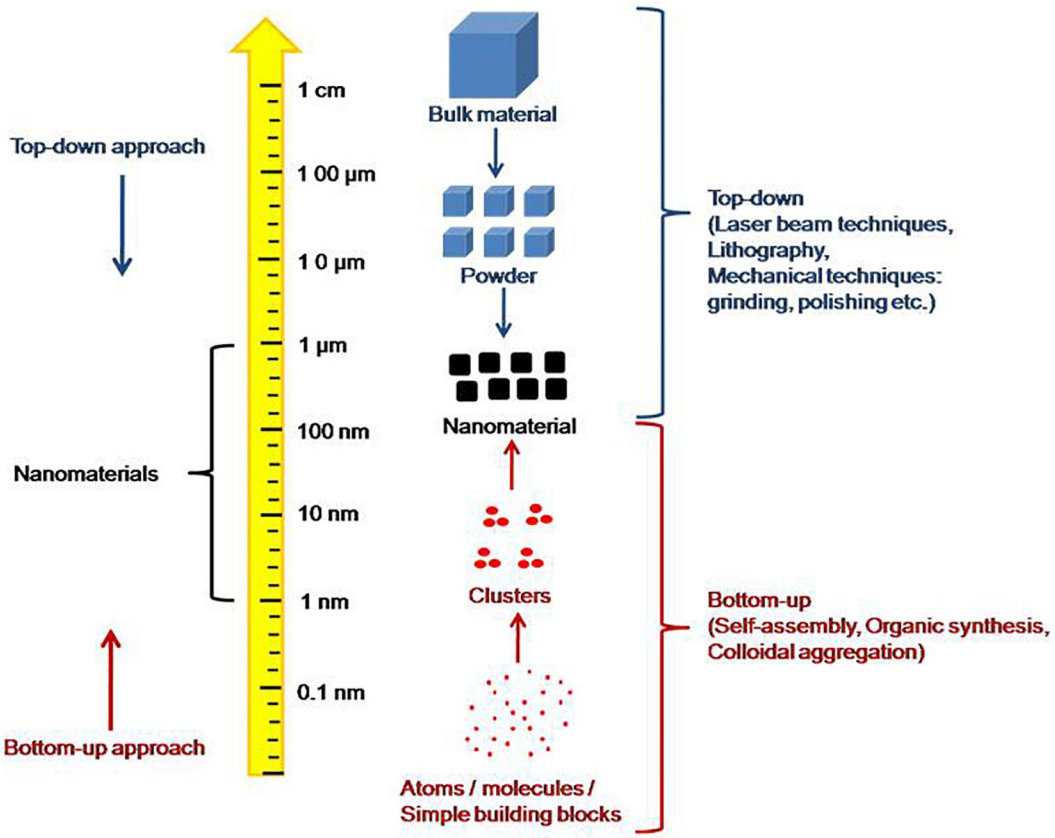

Figure 1. "Top-down" and "bottom-up" approaches used in the synthesis of nanomaterials [7].

The unique attributes of nanomaterials, which includes quantum dots, nanotubes, carbon dots, are exploited in several fields of science, engineering, technology, medicine, and environmental science [8].

Although nanomaterials' undisputed pivotal role in the marketplace, the long-term human exposure triggers potential adverse health and environmental consequences. In this regard, there is a new area of study that deals with NMs toxicological or biological effects: **nanotoxicology**. Nanotoxicity or nanotoxicological studies are intended to investigate whether the quantum size effects and large surface area to volume ratio of NMs may present a risk for the environment and living organisms [9].

Due to the nano size, NMs may enter the human body by three main exposure routes: inhalation, ingestion, skin contact, and potentially interact with intracellular components and macromolecules leading to toxicological effects, including inflammation, genotoxicity, carcinogenesis (Figure 2) [10].

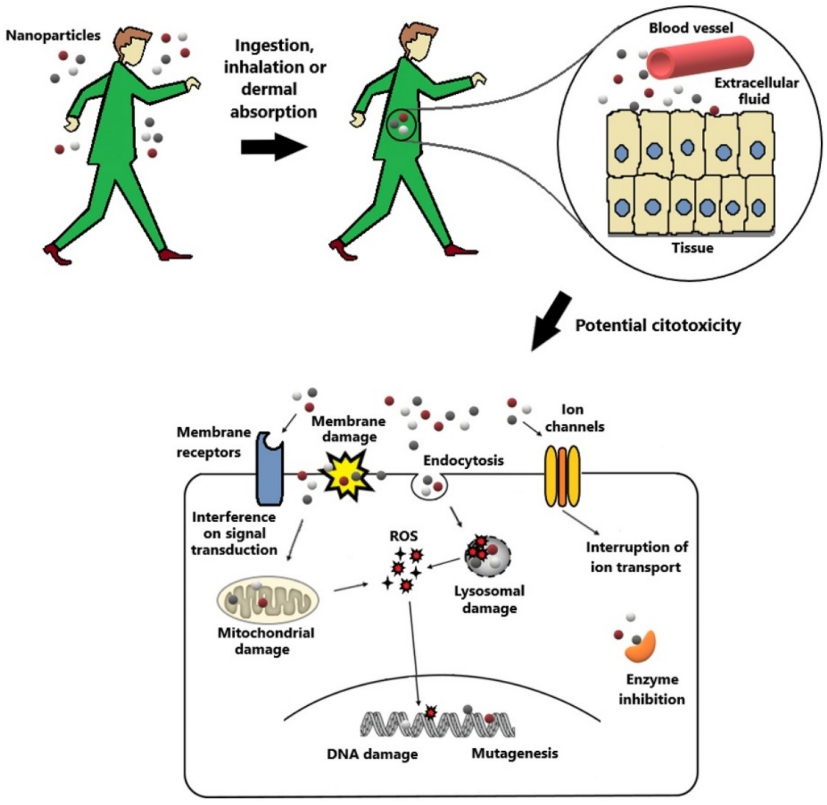

Figure 2. Human exposure to nanoparticles through inhalation, ingestion, or skin contact and consequent uptake by higher organisms. Cellular internalization may lead to passive or receptor-mediated transport across the cell membrane with consequent toxicological impacts [11].

Based on these scientific concerns, the Ph.D. work aimed at investigating the toxicological accumulation of the emerging nano-environmental pollutants, nanoplastics, in the immune and reproductive systems cell lines.

1.1.1 The impact of physiochemical properties of nanomaterials on biological system

Despite NMs have exerted an imperative role in the past decades in a multitude of fields due to their unique properties compared to micromaterials or bulk materials, studies assessing the potential hazardous impacts of NMs interaction with cells are yet limited [12].

Nanomaterials toxicity may originate from different factors: size, surface area, composition, and shape.

The interaction of nanomaterials with the biological system may depends on the **particle size** and **surface area**: decreasing the size results in an increase of the surface area to volume ratio, making the nanomaterial surface more reactive. It has been demonstrated that the size is one of the main factors to determine the type of endocytosis, cellular uptake and efficiency of the pathway that occurs. The **aspect ratio** determines the surface to volume ratio, and it has been observed that the toxicity of a particle increases with a higher aspect ratio [13].

The influence on NMs toxicity is also correlated to the **chemical composition**: a) organic nanoparticles (NP), which can be made of proteins, carbohydrates, lipids, polymers; b) carbon-based nanoparticles, i.e., fullerenes, carbon quantum dots, nanotubes; c) inorganic NP, such as metals, ceramics, and semiconductors [12].

Nanomaterials occur in different **shapes**: fibres, rings, tubes, spheres, and planes, which influences the membrane wrapping processes *in vivo* during endocytosis, and phagocytosis pathways [13].

1.1.2 Immune system response to nano-environmental pollutants

The immune system protects the human body from foreign antigens, such as microbes, viruses, cancer cells, nano-pollutants. It plays this role through two lines of defence: innate immunity, and adaptive immunity. The innate immunity is responsible for the

recognition of pathogens, cell stressors or death indicators. It includes dendritic cells, monocytes, macrophages, granulocytes, and natural killer T cells. The innate immune system recognises the pathogen-associated molecular patterns (PAMPs), such as lipopolysaccharides (LPS), aldehyde-derivatized proteins, mannans, teichoic acids, denatured and bacterial DNA. They can bind to the pathogen-recognition receptors (PRR), which are involved in phagocytosis, inflammatory signalling pathways, apoptosis, and activation of complement or coagulation cascades.

Another important group of receptors are called Toll-like receptors (TLR), typical of immune cells, endothelial and epithelial cells, and fibroblasts. The TLR-microbial ligands binding triggers the activation of phagocytes to the site of infection or inflammation, clearance of the non-self-agent, and the production of pro-inflammatory cytokines and chemokines (tumour necrosis factor, interleukins 1 and 6).

The adaptive immune system components instead, are T and B lymphocytes, which are capable to maintain the "memory" of the previously encountered pathogens, by responding quicker and more efficiently in the following events [14], [15] (Figure 3).

Among the innate immune system, macrophages play an important role in homeostasis, metabolic function, clearance of debris, tissue repairing and remodelling. Macrophages can differentiate in phenotype M1, and M2. M1 macrophages are polarized *in vitro* by interferon-γ (IFN- γ) and lipopolysaccharide (LPS) from bacteria, and mediate pro-inflammatory pathways; by contrast, M2 macrophages are polarized by interleukins 2, and 10, and are involved in tissue repairing, or anti-tumour responses [16].

Nanoparticles' effects on monocytes/macrophages can be multiple: a) modulation of the bone marrow activation, b) monocytes mobilisation and recruitment, c) increase of the microvascular permeability and d) modulation of the macrophage's polarization. Nanoparticles can also use monocytes/macrophages to improve their efficacy towards the target and bypass the immune system clearance [17].

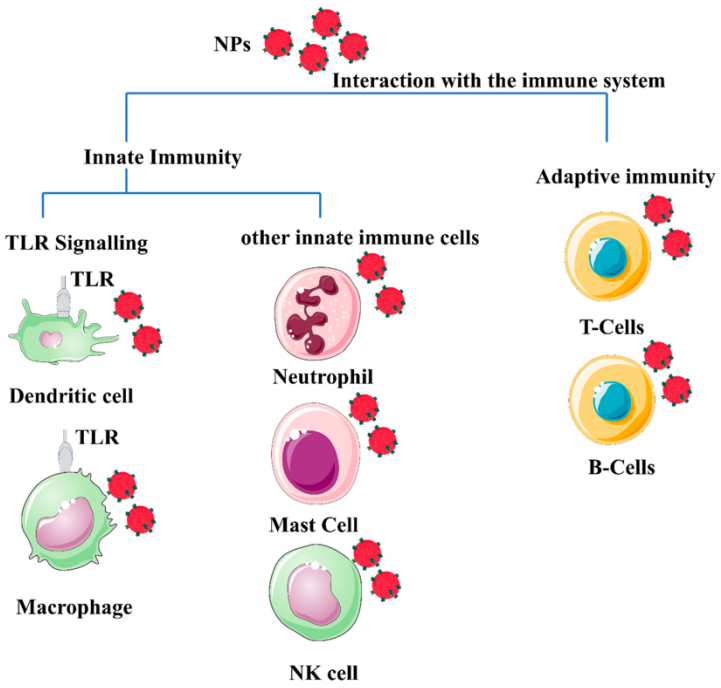

Figure 3. The different nanoparticles (NP)-immune cell response (innate, and adaptive immunity) [18].

The cells in our body may internalize nanoparticles through some of the processes involved in the cellular uptake of nutrients, signalling molecules, or ions, by the energy-dependent transport endocytosis (Figure 4). They can be classified into non-specific, such as macro-pinocytosis and pinocytosis and specific, i.e., endocytosis (clathrin- and caveolin-mediated) and phagocytosis. The phagocytotic process is mediated by professional phagocytes (macrophages, dendritic cells, and neutrophils), which may express different receptors: mannose, complement, scavenger mediated or FCγ receptor. This process leads to the internalization of particles larger than 500 nm in size [19].

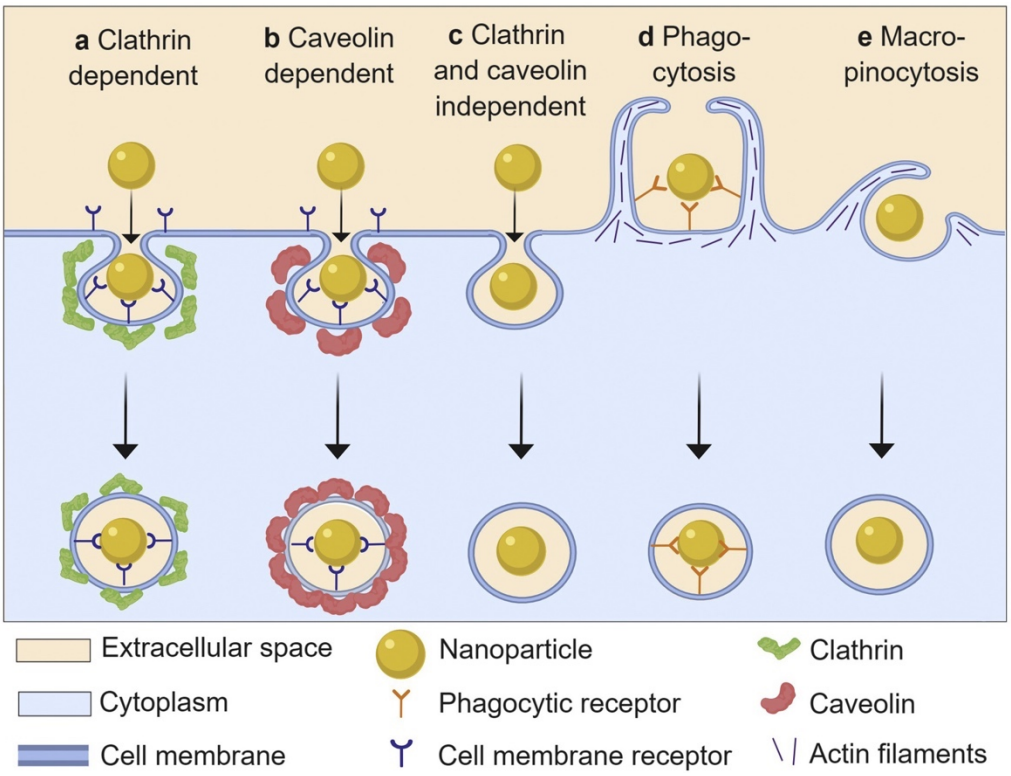

Figure 4. Schematic overview of specific (clathrin- and caveolin-mediated endocytosis and phagocytosis) and non-specific (macro-pinocytosis and pinocytosis) nanoparticles endocytosis pathways in cells [20].

1.1.3 The impact of nanotoxicity on reproductive health

Nanotechnology demonstrated to play an imperative role in several application fields, including biomedical science, catalysis, and electronics. Although it provides excellent solutions, the exposure to NP in humans and animals has gained a growing attention concerning their harmful impacts on toxicity. Being NP very small in size, it makes them easier to penetrate the human barriers, where they can aggregate, and bind to human cells impairing the normal homeostasis. These adverse effects can impact the reproductive system at the clinical, cellular, and molecular levels, compromising the fertility, reproduction, and foetal development.

In vitro studies showed that silver (Ag) NP induce the germ cells' alteration and somatic cells' function in adult male, mainly due to cell apoptosis, DNA and/or mitochondrial damage, oxidative stress, membrane peroxidation [21]–[23].

Similarly, the reproductive female could be affected by nanoparticles' adverse effects. The reproductive anatomy is composed by the hypothalamic-pituitary-gonadal axis and reproductive organs (ovary, oviducts, uterus, vagina, external genitalia) [24].

Titanium dioxide (TiO_2) NP demonstrated to cause ovarian development disorders of rats using *in vitro* rat preantral follicle culture system. The study showed that 25 nm TiO_2 ($\geq$ 25 μg/mL) can inhibit the follicle development of rat and the oocyte maturation *in vitro*. Interestingly, at micrometre size, the same dose of TiO_2 did not show to cause any toxic effect on the same case model, underling the major toxicological concern towards NP [25].

In another study, the toxicity of cerium dioxide nanoparticles (CeO_2 NP), which are widely used due to their catalytic and oxidative properties, was tested during *in vitro* fertilization. A statistic number of oocytes (1272) were exposed to a very low concentration of 7 nm sized CeO_2 NP (10 μg/mL), which evidenced to decrease by 15% the fertilization rate compared to the control oocytes in the culture medium. It might be caused by the NP a) genotoxicity effects on gametes, b) oxidative stress, or c) mechanical effect, disrupting gamete interaction [26].

Nanotoxicity could also arise from particulate matter (PM) exposure in pregnant women compromising the foetus development, in term of low birth weight, preterm birth, and preeclampsia, as reported by Pedersen *et al.* [27].

In principle, NMs can impair the foetal growth through:

a) a direct pathway: NP are capable to cross the placental barrier from the maternal blood and may induce inflammation and reactive oxygen species generation (ROS) and consequently damage the foetal tissue due to their high surface reactivity [28];
b) or an indirect pathway: after exposure via inhalation, ingestion, or skin contact, NP accumulated in maternal tissue barriers can interfere with the foetal development in an indirect way, meaning without directly interacting with the foetal tissue. In the maternal mediated development toxicity, inflammatory mediators or soluble signalling factors produced in response to oxidative stress can reach the placenta and the foetus causing potential toxic effects [29].

Based on this evidence, it is beyond important to provide a comprehensive understanding of the NMs origin and accumulation in animals and humans, in order to unravel the toxicological adverse effects in regard to the reproductive health.

1.2 Micro- and Nano- plastics: an emerging health concern

Micro-/nano-plastics (MNPs) are emerging pollutants which have gained tremendous attention due to their persistence and accumulation in the environment, posing a threat for human health exposure.

Plastics are defined as polymeric particles in combination with additives to obtain the required properties for commercial purposes (mechanical properties, solar or bacterial resistance, colour). Plastic debris are released in the environment and can break down into different size fractions, i.e., nanoplastics [30] (Figure 5).

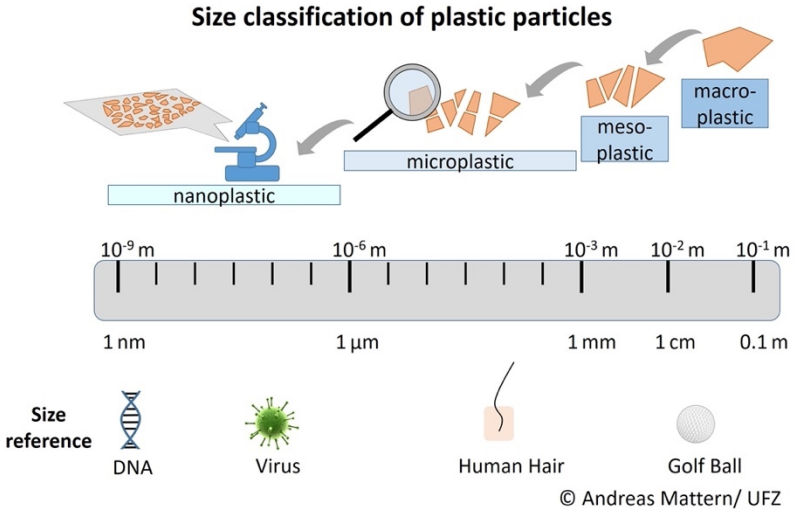

Figure 5. The classification of plastics based on their size. ©Andreas Mattern

Microplastics are classified according to different criteria: a) size, b) origin, c) shape, d) chemical composition:

a) Based on their **size**, plastics can be classified in four classes: nanoplastics are smaller than 1 nm; MPs are below 5 mm in diameter; mesoplastics fall in a range of 0.5-5 cm; macroplastics are 5-50 cm in size [31].
b) **Primary MPs** are directly manufactured for commercial purposes, and they can be found in cosmetic and skin care products (i.e., microbeads in scrub gels, body, and facial cleaners). By contrast, **secondary MPs** derive from the fragmentation of larger plastics (rope, packaging), abrasion of tires during the driving, or laundering synthetic clothes and represent 70-80 % of MPs released in the environment [32].

c) MPs can vary in **shape** and can occur as cylindrical, disks, flat, ovoid, spheroids pellets; rounded, angular for fragments; or irregular, elongated, rough [33].

d) The chemical composition is related to the source of the material and the most common polymers in the environments are based on polyethylene (PE), polypropylene (PP), polystyrene (PS), polyvinylchloride (PVC), nylon (PA), cellulose acetate (CA), and thermoplastic polyester (PET) [34].

The widespread production, consumption and wasting of MNPs presents a risk for human health being exposed to these emerging pollutants through ingestion, skin contact, and inhalation. The MNPs presence has been detected in drinking water, seafood or other food items, atmospheric fallout, which may cause inflammation, oxidative stress, and particle toxicity in humans. Nonetheless, the high surface to volume ratio may lead to the absorption of other organic pollutants or microbes present in the environment, increasing the potential toxicological impacts on the target [35].
Although the abundance of MNPs in the environment and the demonstrated traces in living organisms, the toxicological studies are still limited. Moreover, nanoplastics are difficult to be characterized with respect to microplastics, decreasing and making challenging the number of biological studies (Figure 6).

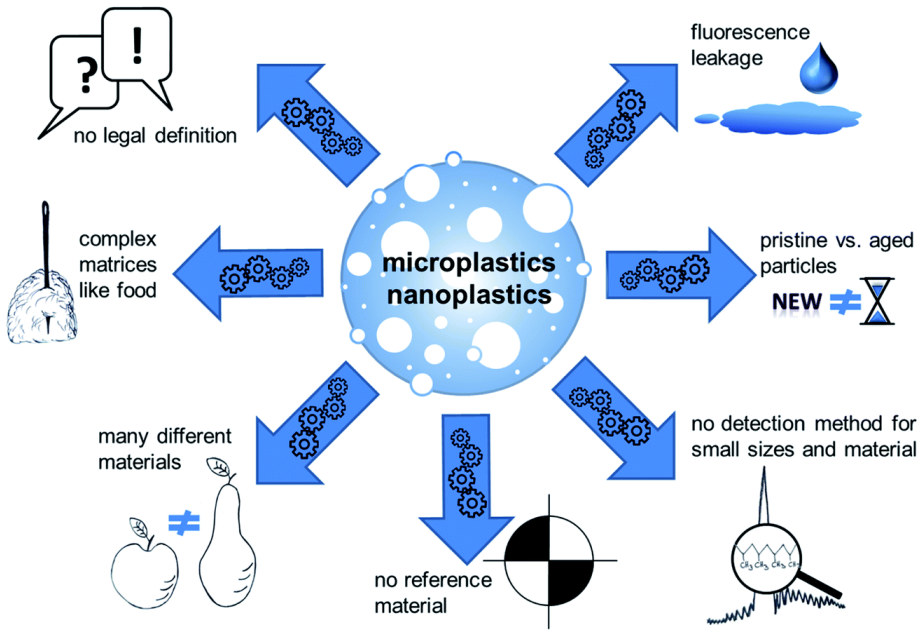

Figure 6. Challenges in the detection of micro- and nano-plastics [36].

1.2.1 Nanoplastics toxicity and biological barriers

Nanoplastics can interact with the biological barriers and be translocated to the cellular compartments in living organisms. They are found at low concentrations, causing the accumulation and consequent adverse health effects of nanoplastics in humans [37].
Three are the main human exposure routes to MNPs: a) ingestion, b) inhalation, c) skin contact, as depicted in Figure 7:

a) The **digestive tract** is considered the main way of human exposure to MNPs. After ingestion, the Peyer's patches of the ileum of the small intestine, which are part of the gut-associated lymphoid tissues, can translocate 0.1-10 μm sized particles from the intestine to the mucosal lymphoid tissues. The MNPs can encounter and bind to the specific antigens that are present along the mucosal surfaces, thus initiating the immune responses. Larger particles, above 130 μm in diameter, are up taken by the gastro-intestinal tract through persorption of the epithelial layer [38].
b) Once MNPs are inhaled, from the **respiratory epithelium** they may translocate via diffusion, direct cellular penetration, or active cellular transport via endocytic and phagocytic pathways. Phagocytosis is the most common process for the particles in size between 1 and 3 μm, whereas smaller particles could passively be transported via diffusion across membrane pores [39].
c) The **dermal exposure** comes from the several personal care products that humans use daily, such as scrubbing powder cleaners, shampoo, make-up. Schirinzi *et al.* demonstrated that polystyrene, differently from polyethylene, caused reactive oxygen species (ROS) generation on human epithelial cells, underling the importance of the different chemical composition on adverse health effects [40].

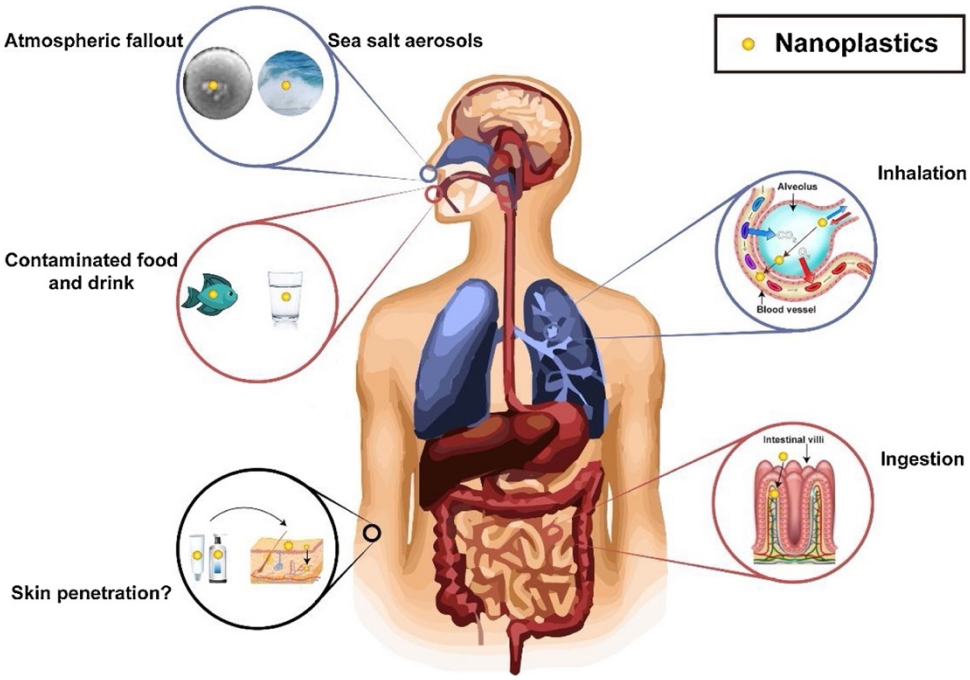

Figure 7. Human exposure to plastic: inhalation (blue), ingestion (red), skin contact (black) [41].

Cells can internalize micro- and nano- particles through two main ways:

a) **Passive transport:** small molecules and particles are transported according to a concentration gradient across the plasma membrane without energy consumption.
b) **Active transport:** substances are transported against the concentration gradient and requires the consumption of ATP.

In vitro and *in vivo* studies demonstrated that nanoplastics internalised into cells can interact with several organelles, such as mitochondria, lysosomes, and endoplasmic reticulum, by triggering further toxicological mechanisms [42]

1.2.2 Model nanoplastics

Most laboratory studies investigated the toxicity of nanoplastics using polystyrene nanospheres commercially available. Although these synthetised plastics can be tuned in size, surface area and functionalisation, they are not representative of the

environmental nanoplastics since they are monodispersed, spherical, and chemically different compared to the manufactured plastics for industrial and domestic applications. To overcome this gap, model nanoplastics are being synthetised in laboratories through the **"bottom-up"** or **"top-down"** approaches.

The **bottom-up** approach includes the methods of the colloidal chemistry, such as conventional dispersed media (emulsions and nanoprecipitation). The synthesis of the plastics allows to calibrate the sample with the desired features for the experimental plan, i.e., chemical functionality, size, concentration, addition of components. Nanoplastics are also used for biological studies to evaluate their uptake and accumulation at the cellular level. To this aim, isotopic or metallic tracer or fluorophores, i.e., Nile red, or Rhodamine, can be embedded in the core of plastics [43]. Model nanoplastics can also be obtained by fragmentating macro- and micro- plastics samples at the nanometre size by different approaches, such as laser ablation [44], photodegradation [45], ultra-sonication [46], or mechanical degradation [47]. However, this **top-down** process allows to produce only nanoplastics with irregular shape, surface defects, and at a very low concentration.

Given the real biological hazard raised from micro- and nano-plastics, it is urgent to standardize a representative model nanoplastics suitable for laboratory studies.

The scientific literature did not report a controlled and fully characterized polypropylene, and polyvinylchloride nanoplastics. Only a few groups have described the synthesis of 60 nm sized polypropylene plastics, through the polymerization reaction with the Ziegler-Natta catalyst [48], [49].

Although the described synthetic route maintains the high molecular weight of polypropylene at nanoscale, this approach is time consuming, and requires the use of dangerous solvents in high-pressure reactors up to 15 MPa, by working at temperatures up to 170 °C. In addition, a purification process must be performed on the synthetised nanoplastics, to separate both the metallic catalyst and the unreacted propylene monomer.

D. M. Mitrano *et al.*, proposed a method to synthetize nanoplastics doped with a metal embedded in the polymer layers, to be used as a tracker in the detection of the nanoparticles in biological media, in more accurate and sensitive approach [50]. In addition, other researchers proposed the labelling of 50-100 nm sized polystyrene nanoplastics with the Nile Red dye, characterised by the solvatochromic and fluorescence properties. However, the linker is bond on the surface of the polymer and

might suffer from leakage when in contact with the biological media, not allowing a precise methodical study [51].

Based on the described limits, D. Cassano *et al.*, proposed a novel synthesis approach for polypropylene and polyvinylchloride nanoplastics, through an oil-in-water emulsion precipitation with the use of a biosurfactant, sodium cholate. The synthetic route lasts around 3 h and the inorganic species (quantum dots, gold nanoparticles, platinum octaethylporphyrin) are entrapped in the polymeric core. The NPs are in a size range between 80 and 350 nm, water dispersible and stable in biological media [52].

1.2.3 Vibrational and microscopy techniques in assessing exposure risk to nanoplastics

The detection and characterization of nanoplastics in toxicological studies still presents a scientific challenge due to their small size (nm), low concentration, and co-presence of additives, i.e., dyes, and biomolecules, polymer based as nanoparticles, which interfere with the analytical detection [53].

The analysis of nanoplastics includes the following steps: a) sampling, b) sample preparation, c) analysis.

Several **microscopic** and **spectroscopic** techniques have been exploited to characterize the size, chemical composition, concentration, morphology, and accumulation of nanoplastics in biological samples, even though with several limitations (Figure 8).

The visualisation of nanoplastics often requires the use of advanced imaging techniques, such as Scanning Electron Microscopy (SEM), Energy Dispersive Spectroscopy (EDS), Transmission Electron Microscopy (TEM), Atomic Force Microscopy (AFM) [54].

SEM-Energy Dispersive Spectroscopy detects the scattered electron (Auger electron) with later resolution of 1 μm and 1-2 μm in depth. EDS detects the X-rays generated from the material surface bombarded with the electron beam, able to resolve chemical information at a later resolution of over 1 μm. Operating at over 5 kV, **SEM** or **TEM** are capable to image the nanoplastics, but it gets challenging to precisely characterize the type or chemical composition of nanoplastics, especially if in cells or tissues [53].

Atomic Force Microscopy has been widely exploited to identify nanoparticles, i.e., polymeric membranes, engineered NPs, by producing a high resolved image at few nanometres in a non-destructive way. However, AFM may produce artifacts from the

damage due to the tip-sample interaction, or it is not able to prevent external factors, i.e., contaminations. In addition, adhesive polymers could lead to the release of fragments providing an incorrect image of the sample. Therefore, AFM is combined with other techniques, such as FTIR or Raman spectro-microscopies [55].

Fourier Transform Infrared Microscopy is an established tool to characterize polymer-based nanoparticles, as it provides the molecular composition of the sample. However, FTIR analysis is challenging in biological matrix containing NPs, due to the interference of the organic matter made of similar chemical groups as the polymers. Being the biomolecules at higher concentrations with respect to the nanoplastics, their related vibrational bands will become the major contribution in the final spectrum.

Since it is extremely hard to discriminate the nanoplastics signals from the biological matrix, observations related to the indirect modification on macromolecules (lipids, proteins, nucleic acids) induced by the exposure to nano-pollutants can be obtained [56].

Micro-Raman technique allows a non-destructive analysis of the biological samples containing particles up to 1 μm in size. It is often combined with an optical microscope that permits the visualisation and detection of the region of interest. The spatial resolution of the technique depends on the wavelength of the laser and the numerical aperture of the objective of the microscope, implying that Raman cannot detect nanoplastics smaller than few hundreds of nanometres [57].

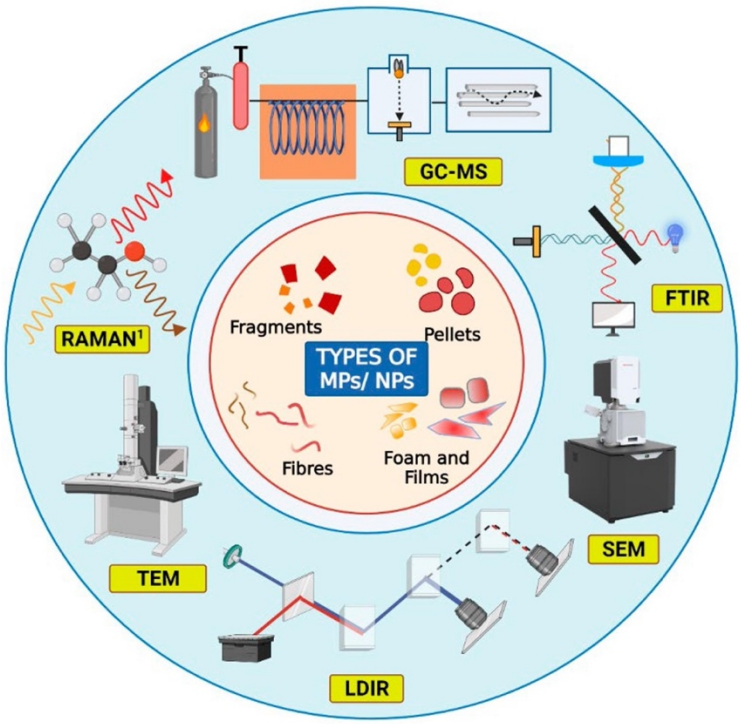

Figure 8. Types and characterization of MNPs. Gas Chromatography-Mass Spectroscopy (GC-MS), Fourier Transform Infrared Spectroscopy (FTIR), Scanning Electron Microscopy (SEM), Laser Direct Infrared Spectroscopy (LDIR), Transmission Electron Microscopy (TEM), Raman Spectroscopy (RAMAN) [58].

1.2.4 New approaches for Nanotoxicology: imaging and elemental analysis by Synchrotron-based X-ray Fluorescence

Synchrotron Radiation facilities are becoming a promising approach in life science research, allowing the possibility to apply multiple techniques to the experimental sample, which enriches the scientific knowledge of biological aspects at micro- and nano- spatial resolution.

The interaction of X-rays with the matter is used in several techniques providing different information about the sample, such as the morphology in the imaging mode, or the elemental distribution in X-ray Fluorescence, or chemical status by X-ray absorption near edge spectroscopy.

In the present research, Scanning Transmission X-ray microscopy (STXM) coupled with X-ray Fluorescence (LEXRF) were performed on nanoplastics and cell samples.

The X-ray beam is generated by the undulator and collimated into a plane-grating monochromator, to select the photon energy required for the experimental plan. The beam is then focused through several optical elements, into a secondary source, an array aperture of different diameters (15, 25, 35, 50, 75,100 or 150 μm), which defines the size of the beam delivered to the end-station.

In STXM mode, the incoming photo beam is focused through a Fresnel Zone Plate (ZP), and the specimen is raster-scanned across the microprobe. The beam size is the image of the secondary source size through the Zone plate optics. To reduce the contribution of unwanted diffraction orders, an order-sorting aperture (OSA) is placed downstream of the ZP, while a central stop on the ZP absorbs zeroth-order radiation. At TwinMic beamline in Elettra Sincrotrone Trieste, the detection system collects the transmitted photons from the specimen with a fast-redout CCD camera *via* a visible-light-converting system, composed of a phosphor screen, a lens, a mirror placed at 45° and an objective lens (Figure 9) [59].

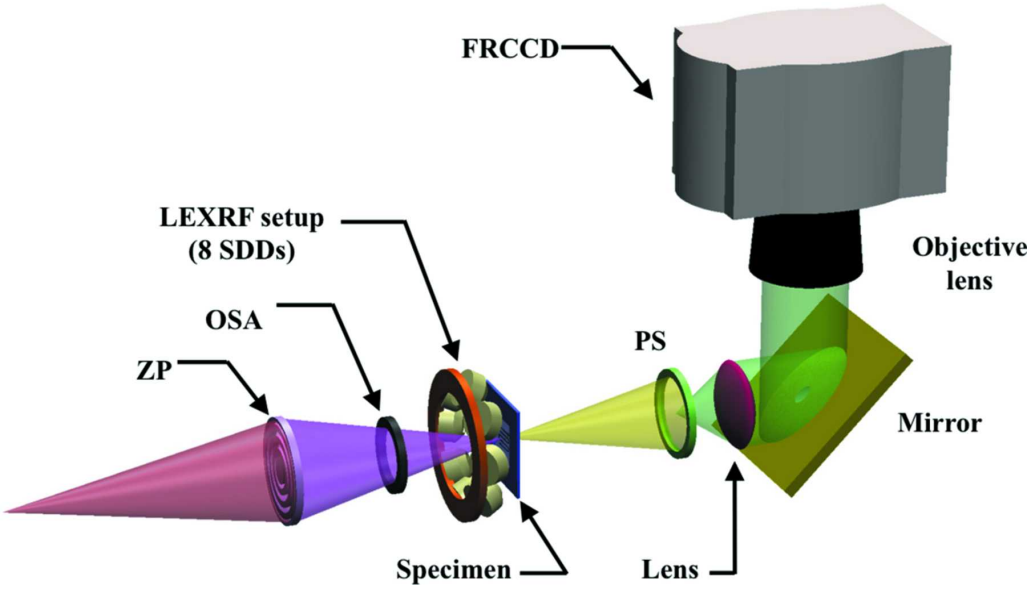

Figure 9. STXM and LEXRF setup at TwinMic beamline, Elettra Sincrotrone Trieste [59]

The absorption and phase contrast images obtained through the STXM mode provide topographic information of the samples at sub-micron spatial resolution [60].

At the same time, it is possible to collect the X-ray fluorescence signals: when the sample is illuminated by the primary X-ray beam, characteristic X-ray fluorescence lines are emitted by the sample's atoms and the XRF photons are collected by eight silicon drift detectors mounted circularly around the sample, to provide the chemical map distributions of the scanned area (Figure 9).

Marmorato P. *et al.* described the intracellular distribution of cobalto ferrite ($CoFe_2O_4$) nanoparticles across Balb/3T3 mouse fibroblasts, exploiting the synchrotron radiation X-ray and fluorescence microscopy. The study revealed the potentiality of the technique to both investigate the spatial distribution of NPs across the fibroblast and monitor the changes of NPs elemental composition in response to intracellular interactions [61].

In another work, A. Gianoncelli *et al.*, supported the advances in folliculogenesis in the reproductive medicine field, by the improvement of the visualisation of ovary structure in bovine tissues with different staining protocols. The combination of X-ray Fluorescence with another synchrotron technique, microtomography, allowed to confirm the benefit of using phosphotungstic acid staining, presenting an increased contrast efficiency because of its higher penetrance in tissues, by following the Tungsten (W) elemental distribution [62].

1.3 General conclusions

Nanotechnology is a flourishing field, which enables the development of new materials with novel properties. The inevitable exposure of subjects to nanomaterials is expected to increase by the years, contributing to the hazardous effects on human health and safety.

The toxicological profile of NMs on humans depends on many factors:

a. **Exposure factors**, i.e., penetration route, duration of exposure, and concentration of NMs.
b. **Characteristics of the exposed organism**, i.e., individual susceptibility, activity at time of exposure, distribution of NMs in the targeted body.
c. **Intrinsic NMs toxicity**, i.e., catalytic activity, composition, electronic structure, surface area, ability to bind or coat surface species.

Over the decade, a growing attention has been focused on the possibility of nanoparticles to bind and interact with biological membranes, including the blood-brain, blood-testis, placenta, and respiratory barriers. It is extremely important the understanding of the uptake mechanisms, transportation, and distribution of NMs via systemic vessels to secondary organs, which most of the times induce consequent effects at the cellular level.

Among many environmental nano-pollutants, plastics are a worldwide emerging risk, with around 5 billion tons of waste dispersed in the environment. It results from a long-term durability, scale-up production, but also inadaptable waste management systems and unsustainable usage. Environmental microplastics is considered as persistent pollutant, durable from hundreds of years to decades. The potential and common fragmentation of larger plastics into smaller pieces, nanoplastics at nanometre sized, pose a major concern on human exposure since at their size they can easily cross and interact with the cellular compartments.

A growing body of literature investigates the ecotoxicological effects of MNPs in marine models, water, and food, being a few the *in vitro* and *in vivo* case studies. It mainly depends on the lack of efficient analytical techniques, capable to visualise and characterize nanoplastics in a complex matrix. In addition, most scientific studies use polystyrene nanobeads, commercially available, even though it is not the most abundant

plastic in the environment. Based on the recent hazardous impacts of nanoplastics on oxidative stress, lipid metabolism, reproductive toxicity, the evaluation through *in vitro* studies to investigate the distribution of nanoplastics and its effects on inflammatory and macromolecular components is becoming crucial.

In general, the toxicity of nanoplastics is determined by their chemical composition, bio-persistence, and the probability to carry on their surface other organic pollutants or microbes/viruses adsorbed from the environment. Model nanoplastics used to study the toxicological effects of NPs on human cell lines must be representative of the environmental pollution (polyvinylchloride, polypropylene) and, possibly, to avoid issues related to the fluorophores nanoplastics (photobleaching, aggregation) in biological media.

To solve the issue related to the incompatible and not-informative analytical tools in the detection of NPs in biological matrix, a combination of advanced techniques could be promising to unravel the toxicity of NMs on human system. In this work, Scanning Transmission X-ray microscopy, X-ray fluorescence microscopy and Fourier Transformed spectromicroscopy allowed a more complete interpretation of nanoplastics at the cellular level. Specifically, synchrotron-based X-ray permitted to image the inorganic species labelled to the polymeric material, and thus the presence of labelled NPs in cells exposed to nanomaterials, at high spatial resolution, and correlated with morphological information. In addition, FTIR spectro-microscopy allowed for an evaluation of their effects on the cellular biochemistry.

Therefore, nanotoxicity aim at unrevealing potential hazardous effects of nanomaterials on living and not living subjects. The multidisciplinary approach will contribute to solve the limits of using one technique by enriching the scientific results with a wider technical point of view in cellular models.

1.4 Aims of the research

My Ph.D. work aimed at contributing to the field of nanotoxicity by unravelling the possible toxicological effects and macromolecular metabolisms impairments induced by two types of nanoplastics (NPs), polypropylene (PP), and polyvinylchloride (PVC) labelled with inorganic species, CdSe-QDs, in two *in vitro* models: immune system cells and ovarian cells.

The research aimed at using a model environmental nanoplastic, which is a representative polymer, and it is labelled to trackable species, allowing a clear discrimination of the nanomaterials across the biological matrix.

Appropriate cell line models were used to investigate the accumulation and effects of these nanomaterials.

My project exploited a combination of advanced analytical techniques, synchrotron based XRF coupled with STXM, FTIR micro-spectroscopy, Particle PIXE, as well as more conventional imaging tools, such as fluorescence microscope, to overcome the difficulties in the analytical detection of polymeric particles in a biological system. The specimens were further measured at the ID21 Beamline, European Synchrotron Radiation Facility, Grenoble to complete the characterization of NPs at nanometric spatial resolution.

Moreover, during the Ph.D. visiting period at the Department of Chemical Sciences at the Dublin City University, a new model of environmental nanoplastics was synthetised starting from Carbon Nano Onions/graphene oxide derived Carbon Dots, allowing the labelling and production of green, fluorescent nanoplastics. The chemical products were analysed by multiple techniques: Dynamic Light Scattering, UV-Visible spectroscopy, fluorescence microscopy, and Transmission Electron Microscopy. The as-described alternative linkers for the synthesis of model NPs were chosen as Carbon Dots are an emerging fluorescent nanomaterial with excellent optical properties, low toxicity, good biocompatibility and recommended for bioimaging *in vitro* toxicity studies.

CHAPTER 2 – Morphological and lipid metabolism alterations in macrophages exposed to model environmental nanoplastics traced by high resolution synchrotron techniques

Based on the considerations discussed in the general introduction, and the techniques that will be explained in this chapter, I will present a toxicological study conducted on human monocyte-activated-macrophagic cell line (THP-1) exposed to two model environmental nanoplastics: Cadmium Selenide Quantum Dots labelled polypropylene, and polyvinylchloride. The two types of nanoparticles effects were investigated using the same material and method described in 2.1 section. The results section (2.2 section) will include a critical interpretation of the data obtained through several analytical approaches for the two types of nanoparticles.

2.1 Material and Methods

2.1.1 Synthesis of Cadmium Selenide Quantum Dots labelled nanoplastics

Polymeric labelled nanoplastics were synthetised at the Joint Research Centre, Ispra, Italy as illustrated in the cited paper [52].

Polypropylene, polyvinyl chloride nano-plastics (PP-, PVC-NPs) were prepared by the oil-in-water emulsion technique by dissolving 30 mg of plastic polymers (Sigma-Aldrich) in 3 g of toluene in an 50 mL-flask, mixed at 100 °C for 1 hour to dissolve the pellets. 200 μL of QdotTM 655 ITKTM (ThermoFisher) organic quantum dots were added to the toluene solution. Afterwards, a boiling ultra-pure MilliQ water solution (27 mL) containing 7.5 mg of the dissolved surfactant sodium cholate (Sigma-Aldrich) was added to the hydrophobic phase and the two separating phases were homogenized using an Ultra-Turrax T25 (IKA) at 16 000 rpm for 2 minutes, ultrasonicated (Vibra-Cell Ultrasonic Liquid Processors, vCX 130) at 40% amplitude for 2.5 minutes, and cooled in an ice-water bath for 3 minutes. The reaction product was filtered by 5 μm poly ether

sulfone membrane syringe filters to obtain the desired NPs size, while the organic phase was successfully evaporated using the rotavapor. The synthetic yield was calculated by weighing the freeze-dried powder. QDs-NPs were dispersed in MilliQ and stored at 4°C in dark condition.

2.1.2 Cell culture and sample preparation

Human monocytic THP-1 cells (ATCC TIB-202) were maintained in a sub-confluent state in complete culture medium, RPMI 1640 (Life Technologies, MI, Italy) supplemented with 10% (v/v) foetal bovine serum (FBS) (Life Technologies, MI, Italy), 1% (v/v) penicillin/streptomycin (Life Technologies, MI, Italy) under standard cell culture conditions (37°C, 5% CO_2 and 95% humidity). The cells were cultured in 75-cm^2 Falcon flask for 2-3 days, then seeded onto silicon carbide membranes (SiC) with 200-nm-thick (Silson Ltd, Warwickshire, UK) contained in 24 multi-well plates. For THP-1 polarization, cells were seeded at $1x10^5$ cells/mL in the complete culture medium with phorbol 12-myristate 13-acetate (PMA) (Thermo Fisher Scientific, MA, USA) to a final concentration of 15 ng/mL. They were incubated at 37 °C, 5% CO_2 for 48 hours, to be activated into resting macrophages (RM), washed with phosphate buffered saline, Dulbecco's formula (PBS) supplemented with Ca^{++} and Mg^{++} (Thermo Fisher Scientific, Kandel, Germany), and the CM (complete medium) was replaced with a PMA-free CM to control the macrophages differentiation. RM were polarized into M1 macrophages by the addition of the following stimuli: IFN-γ (500 U/ml) and LPS (100 ng/mL) (PeproTech, London, UK) for 24 hours. The different conditioned cells were incubated with CM containing the two different NPs labelled with CdSe-QDs at a final concentration of 20 μg/ml for 72 hours. Control M1 cells were grown under the same conditions but were not exposed to NPs. The samples were then fixed at room temperature with a 4% aqueous solution of paraformaldehyde for 20 minutes in the dark and washed with PBS and Milli-Q water before the analyses.

2.1.3 Cell viability test (MTT assay)

Cells were seeded in a 96-wells Falcon plate and treated with different concentrations of labelled and not labelled PP-, PVC-NPs (0, 1, 5, 20, 50 μg/mL), and Staurosporine

2µM (Sigma Aldrich, Milan, Italy) as positive control. After 24 hours of incubation, they were activated and polarized into M1 phenotype and then treated with the testing concentrations of NPs for 72 hours. 10 µL of MTT reagent (3-(4,5-dimethylthiazol-2-yl)-2,5-diphenyl tetrazolium bromide) (Sigma-Aldrich, MI, Italy) was added to each conditioned well in triplicate, incubated for 4 hours at 37 °C, 5% CO_2. The formazan crystals were visible through light microscope, so they were dissolved in dimethyl-sulfoxide (DMSO) (Euroclone, MI, Italy), and the correspondent absorbance was read using ELISA Microplate Reader (Bio-Rad, Hercules, CA, USA) at 570 nm wavelength (Figure 10). The data were collected for triplicate of each condition, subtracted the negative control of the reagent used (MTT) and normalized for the control cells (100%) using GraphPad software.

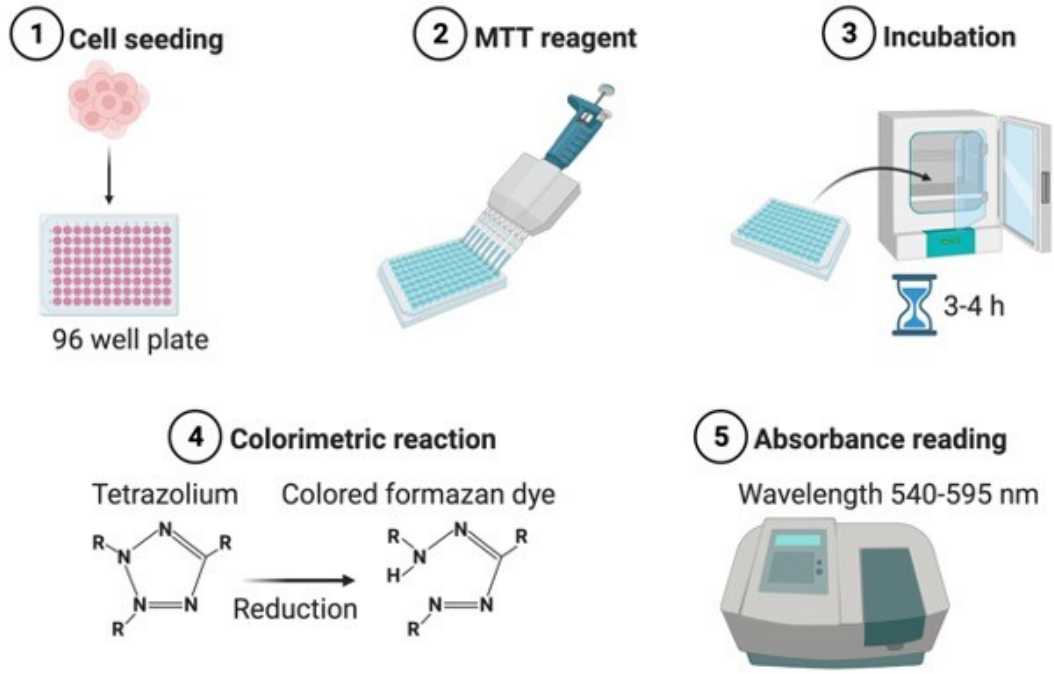

Figure 10. Schematic MTT assay protocol.

2.1.4 Oil Red O staining

THP-1 cells (10^4 cells/mL) were seeded in a 96-wells plate and treated with different concentrations of CdSe-QDs PP-, PVC-NPs (0, 5, 10, 20, 50, 100 µg/mL). After 24 hours of incubation, monocytes were activated and polarized into M1 phenotype and then treated with the testing concentrations of NPs for 24, and 72 hours. At this point, cells were washed twice with PBS, and 100 µL of paraformaldehyde (PFA) 4% in PBS

was added to each well and let for 20 minutes in the dark. Then, sterile water was gently rinsed into the wells. 100 µL of Isopropanol was added to each well and let sit for 2-5 minutes. 100 µL of the Oil Red O (Acros Organics, Geel, Belgium) working solution was added to the wells and the multi-well was slowly rotated to favour the spreading of the solution along the cells. After 5 minutes, the wells were washed with sterile water until the water ran clear. 200 µL of Isopropanol was added to each well, whose 150 µL was transferred to a new 96 well-plate for quantification. The correspondent absorbance was read using ELISA Microplate Reader (Bio-Rad, Hercules, CA, USA) at 450 nm wavelength.

2.1.5 Light fluorescence Microscopy

For each experimental condition, two to three cells among the samples grown on the same or different SiC windows were selected by performing light fluorescence microscopy, to be afterwards analysed by X-Ray Microscopy at Elettra Sincrotrone Trieste. SiC windows were mounted on the sample holder for Fluorescence Microscopy (BioTek Cytation 5 Cell Imaging Multimode Reader, Agilent,CA, USA), operating both in bright field mode and with Texas Red ® filter cube (excitation wavelength 560 $\pm$ 55 nm and emission wavelength 645 $\pm$ 75 nm). Images were acquired at 10X, 20X magnification objective for each experimental condition and were carried out using FiJi software [63].

2.1.6 Scanning Transmission X-ray Microscopy (STXM) and Low-Energy X-Ray Fluorescence (LEXRF)

Scanning Transmission X-ray Microscopy (STXM) and Low-Energy X-Ray Fluorescence (LEXRF) were performed at the TwinMic beamline at Elettra Sincrotrone Trieste, Italy [59], [64]. The TwinMic microscope was operated in the scanning transmission mode (STXM), where the beam is focused on the sample through a zone plate (600 µm diameter and 50 nm outermost zone width), delivering a micrometric or sub-micrometric probe size. Samples were raster-scanned perpendicularly to the incoming monochromatic beam, while a fast readout charge-coupled device (CCD)

camera collected the transmitted X-rays [60], and an 8-silicon drift detector-based XRF system acquired the emitted fluorescence photons [59], [65].

The obtained absorption and phase contrast images outlined the morphological sample features at sub-micrometre length scales, while the simultaneous detection of LEXRF correlated the elemental distribution to the morphology. Elemental distribution has been obtained with PyMCA software [66], by deconvolving and fitting the XRF spectra. For high resolutions images operating in the STXM mode, a photon energy 1.2 keV was used, with a spot size of about 200 nm and a CDD dwell time of 60 ms. Parameters were then changed to acquire XRF maps on a smaller area, using a photon energy of 1.7 keV to excite and obtain optimal emission conditions for the element of major interest, Se, with a spot size of 490 nm and a dwell time of 10 seconds per pixel for XRF mapping, and a CCD dwell time of 60 ms per STXM imaging. Each map lasted approximately 8−12 h, depending on the dimensions of the scanned area. We mapped about 2-3 cells per SiC window.

2.1.7 Fourier Transform Infrared Micro-Spectroscopy (FTIR) and Imaging

FTIR micro-spectroscopy measurements were performed at the Chemical and Life Science branch of the SISSI-Bio beamline, Elettra Sincrotrone Trieste (Trieste, Italy) [67], using a Hyperion 3000 Vis-IR microscope (15X condenser/objective) and a MCT detector coupled with a Vertex 70v interferometer (Bruker Optics GmbH, Ettlingen, Germany). FTIR measurements were collected in transmission mode in the MIR region (4000-800 cm^{-1} at 4 cm^{-1} spectral resolution). For each condition, 40 to 300 single spectra (averaging 512 scans per each spectrum and 1 minute per spectrum) were acquired, in both cytoplasmatic and nuclear regions. Background spectra were collected for each measure in a cell-free area with the same parameters. In addition, cellular imaging was performed using a 64x64 pixels Focal Plane Array (FPA) detector, collecting 2-3 maps spanning multiple tiles per condition averaging 256 scans (20 minutes per image) with 4 cm^{-1} spectral resolution and a pixel size of 2.6 micron (15X condenser/objective). Data analyses were carried out using OPUS software (Bruker Optics, Billerica MA, US), for water vapor correction and then Quasar (http:\\quasar.codes) for spectra processing: baseline correction, cut, normalization

when required, calculation of the band integrals and ratios, and principal component analysis. To filter the pixels belonging to empty areas that could affect the results an intensity filter on the peak at 1650 cm^{-1} was applied. Then, statistical analysis was carried out using OriginPro 2023 (Originlabs). For univariate analysis the following band integrals were calculated: 2800-3000 cm^{-1} for lipids, peak height at 2925 cm^{-1} for the CH_2 asymmetric stretching, and at 2960 cm^{-1} for the CH_3 asymmetric stretching, 1710-1765 cm^{-1} for carbonyl group (CO), 1716 cm^{-1} for free fatty acids (FFAs), 1740 cm^{-1} for triacylglycerols (TAGs), and 1700-1480 cm^{-1} for the amide bands of proteins. Multivariate analysis was carried out using Quasar. Second order derivative of absorbance spectra was calculated using Savitzky-Golay algorithm using 21 points of smoothing, 3rd degree fitting polynomial function. Then the data were normalized using vector normalization and principal component analysis (PCA) was performed using 10 components. The results are shown as scatterplot of PC1 vs PC2 vs PC3 and line plots of the respective loadings.

2.2 Results

2.2.1 Cell viability studies (MTT assay)

In Figure 11, the results obtained from the cell viability studies are reported, using the MTT assay, to study the cytotoxicity of not labelled (PP-, PVC-NPs) and labelled NPs (CdSe-QDs PP-, PVC-NPs) on M1 phenotype macrophages after 72 h of incubation with concentrations ranging from 0 to 50 μg/mL. The cell viability was kept around 70% till the highest used NPs concentration (50 μg/mL) with no significant difference in the two polymers, in line with what reported in literature [68].

As expected, the presence of QDs did not increase the toxicity of NPs, as shown in Figure 11A-B. The apoptotic factor, Staurosporine, was used as positive control, demonstrating to decrease the cell survival down to 40%. Based on the cell viability tests, the concentration corresponding to 20 μg/mL of CdSe-QDs PP-, and PVC-NPs was selected for the uptake analyses.

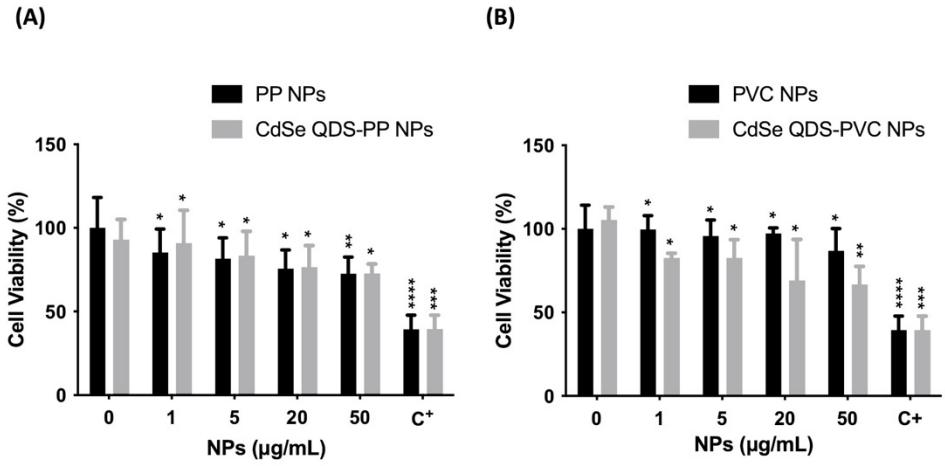

Figure 11. Analysis of cytotoxicity induced by NPs. Cellular viability percentage normalized over the controls (monocyte-macrophages M1 polarized) as a function of increased concentration (0-50 µg/mL) of not labelled and labelled PP-NPs A) and PVC-NPs, B) respectively. The positive control (C^+) refers to the Staurosporine, apoptotic factor 2 µM (1:200). *p < 0.05, **p < 0.01, ***p < 0.001, ****p < 0.0001, black * (t-test method) versus untreated (0 µg/ml).

2.2.2 Oil Red O Staining

To investigate the lipid metabolic response of M1 macrophages exposed to increased concentration of CdSe-QDs PP-, PVC-NPs [61], the Oil Red O staining was performed to possibly identify a peculiar increase of lipid droplet (LD) formation. At the selected concentrations, ranging from 0 to 100 µg/mL of CdSe-QDs PP-, PVC-NPs, (Figure 12A-B, respectively), the above-mentioned staining was used to quantify the vesicles presence, with respect to the control, unexposed cells. After 24 h of incubation, the results show that all concentrations of NPs enhanced the LDs contents with a slight, but statistically significant, linear increase from 100% in control cells to 130% in cells exposed to 100 µg/mL of CdSe QDs PP-, PVC-NPs. The LD quantification was performed also after 72 h of CdSe QDs PP-, PVC-NPs cell incubation, which revealed a linear consistency in the LD increase up to 20 µg/mL NPs, with a p value <0.05. On the contrary, starting from 20 µg/mL of NPs concentration, an inversion occurred. It can be hypothesized that a more complex metabolic response takes place, such as apoptotic pathways activation. Again, the data confirmed that the 20 µg/mL concentration was the best compromise to further characterize those lipid macromolecular changes (FTIR).

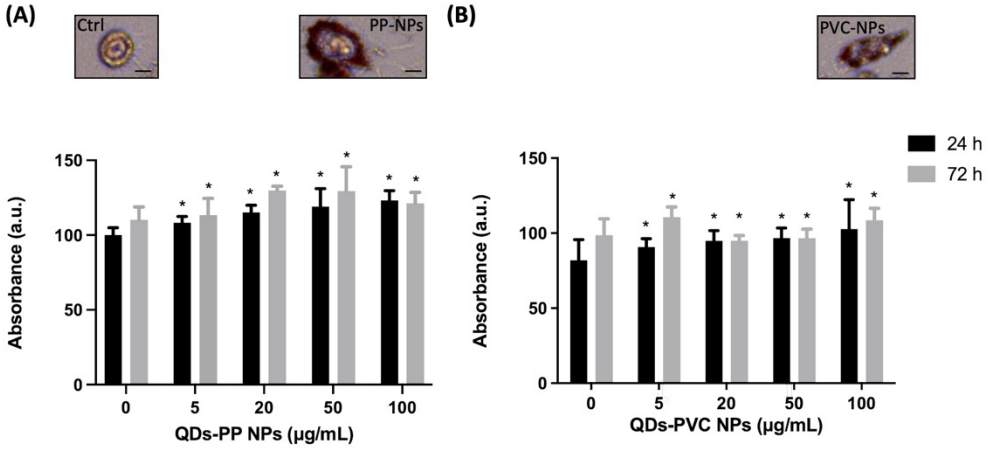

Figure 12. Analysis of lipid contents by Oil O Red staining. Absorbance measured at 450 nm of the Oil Red O normalized over the controls (monocyte-macrophages M1 polarized) as a function of increased concentration (0-100 µg/mL) of CdSe-QDs PP-NPs and CdSe-QDs PVC-NPs, respectively. *p < 0.05, black * (t-test method) versus untreated (0 µg/ml). Insets show the red fluorescence images in the red range of selected cells as an example for the three treatment conditions. The scale bar is 5 µm.

2.2.3 Light fluorescence Microscopy

The light fluorescence images in Figure 13A and Figure 13F, respectively, show the specific bright red emitting property of CdSe-QDs-PVC, and -PP drops (1 mg/mL) deposited on 200 nm thickness SiC windows, acquired with the Texas Red filter cube (excitation 560 ± 55 nm and emission 645 ± 75 nm). Thus, the presence of this nano-sized CdSe-QDs confirmed to be an optimal labelling strategy to track NPs in cell samples, by conferring to the polymers to be visible under light fluorescence images due to CdSe-QDs intrinsic red emitting property [52].

Although a slight artefactual autofluorescence (red) of macrophages incubated with CdSe-QDs-PVC, or -PP, appreciable in Figure 13B and Figure 13G, respectively, the QDs labelled NPs can be identified by the red spots at the highest brightness as depicted in panels Figure 13C-E, and Figure 13H-L. The light fluorescence images were extremely supportive and used as a preliminary guide in the selection of 2-3 cell per sample to be analysed at higher spatial resolution by synchrotron-based technique, specifically LEXRF, to confirm the presence of NPs by following the emission L line of Se, one of the two components linked to NPs.

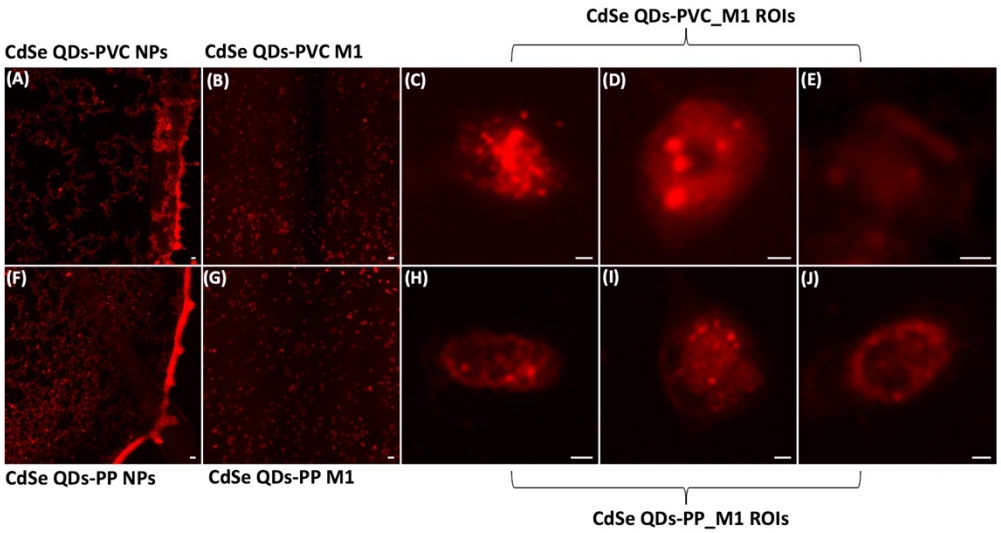

Figure 13. Fluorescence images characterize NPs localisation. Fluorescence images of CdSe-QDs PVC-NPs (A), PP-NPs (F), on silicon carbide windows 200 nm thickness acquired with Texas Red filter cube (excitation 560 ± 55 nm and emission 645 ± 75 nm) fluorescence microscope, 10X magnification. Scale bar is 10 μm. Panels (B) and (G) present the M1 macrophagic cells exposed to 20 μg/mL of PVC-NPs and PP-NPs respectively. Scale bar is 50 μm. Panels (C-E) and (H-J) show the selected cells further analyzed. Brighter spots indicate the presence of PVC-NPs and PP-NPs, 20X magnification. Scale bar is 5 μm.

2.2.4 Scanning Transmission X-ray Microscopy (STXM) and Low-Energy X-Ray Fluorescence (LEXRF)

The monocyte-polarized-macrophages topographic information before and after the 72-h incubation of cells with NPs have been provided by STXM absorption and phase contrast images visible in the Figures 14-15, respectively for CdSe-QDs-PP, and -PVC NPs. In Figure 14A and Figure 15A, the morphology of unexposed cell is shown, with a more absorbent nuclear region. Instead, when cells were exposed to NPs, especially PP, the formation of bright vesicles was often observed in the absorption and phase contrast images, like those reported in Figure 14C-D. Note that the contrast in the differential image of Figure 14A is different from the one presented in Figure 15A due to beam brightness/beam fluctuations. Based on already published studies [61], the bright vesicles evidenced by STXM are clearly suggestive of LDs, that frequently localize perinuclearly and at the plasma membrane. On the contrary, both absorption and phase contrast images, compared to those in visible light, do not evidence the presence of NPs aggregates at the cell surface.

More importantly, the LEXRF analyses performed at 1.7 keV demonstrated to be a suitable tool to track a label of NPs, the Selenium. This component is shown in the third column of Figure 14 and Figure 15. The chemical map distribution of low-Z elements (C, O, and Na) was acquired and shown in the same Figure. In this way, both the cellular integrity and the specific localization of the NPs in the cells can be monitored.

The cells images reported in the Figure 14B-D and Figure 15B-D are the same of the fluorescence image insights reported in the Figure 13, whose red spots (NPs) localization are in good agreement with the Selenium (QDs) distribution across the cell. Moreover, a possible internalisation of NPs at submicron spatial resolution can be observed. Although the STXM coupled with LEXRF is not a 3D microscopy, the peculiar distribution of Selenium in nanometric spots across the cells is suggestive of a cellular cytoplasmatic accumulation, with no evidence of interaction with the LDs.

As a negative control, the same measurement conditions were used to acquire unexposed cells, which revealed no Se-related peak, analysing the fitting process. These results do confirm the specificity of the Se signal for NPs presence. To note, the hotspot appearing in Figure 14A, Se XRF map, corresponds to the Al contamination on the sample, as Se L-line falls on the shoulder of Al K-line.

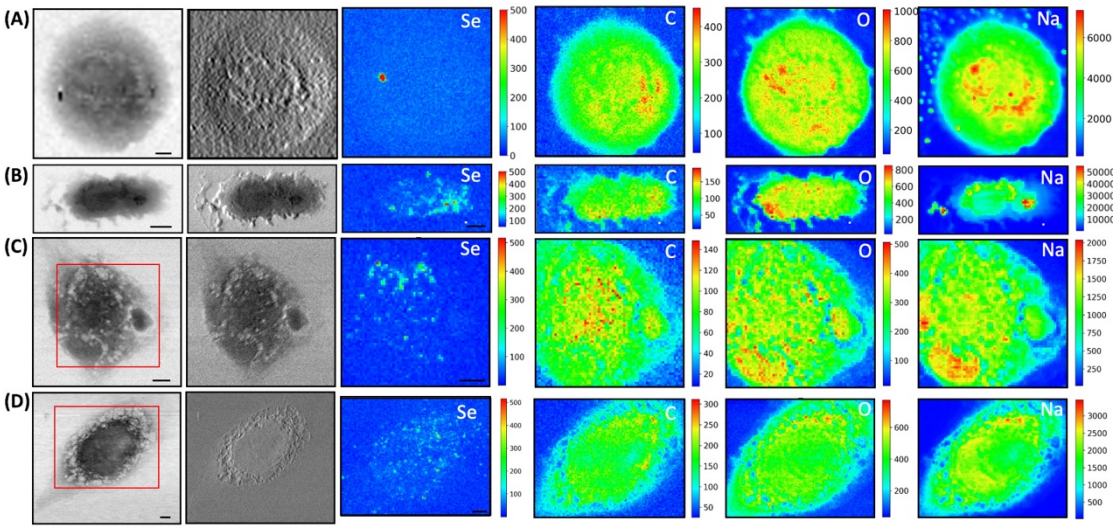

Figure 14. STXM absorption and phase contrast together with μXRF maps of Se, C, O and Na of monocyte-polarized M1 macrophages controls A) and 20 μg/mL of CdSe-QDs PP-NPs exposed B-D). The absorption and phase contrast images were measured at TwinMic beamline with 1.7 keV photon energy and 450 nm spatial resolution. The XRF maps show the elemental map distribution on selected areas (red square). Scale bars are 5 μm.

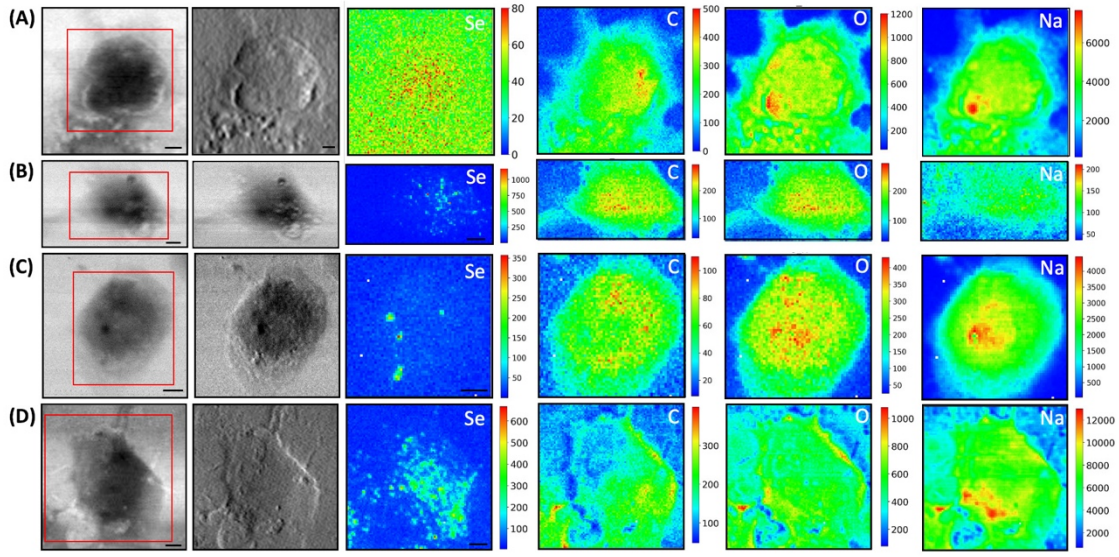

Figure 15. STXM absorption and phase contrast together with μXRF maps of Se, C, O and Na of monocyte-polarized M1 macrophages controls A) and 20 μg/mL of CdSe-QDs PVC-NPs exposed B-D). The absorption and phase contrast images were measured at TwinMic beamline with 1.7 keV photon energy and 450 nm spatial resolution. The XRF maps showing the elemental map distribution on selected areas (red square). Scale bars are 5 μm.

2.2.5 Fourier Transform Infrared Micro-Spectroscopy (FTIR) and Imaging

FTIR microscopy was employed for the characterization of macromolecular changes in the cell samples exposed to NPs. To evaluate the spectral profiles of the different populations of cells and the values of specific band ratios univariate analysis was used. In Figure 16A**,** the normalized average spectra of the three groups of treated (PP_M1, PVC_M1) and not treated cells (Ctrl_M1) are shown (solid lines), compared with the spectra acquired on the labelled polymeric nanoparticles drops (dashed lines), prepared separately.

Specific signals from the NPs and the cells are highlighted in Figure 16, as vertical dashed lines, and listed in Table 1 for reference. Based on that, in our analyses, it was not possible to identify the NPs characteristic bands in the treated cells average spectra by looking at the solid orange line spectra for PP_M1, and the solid blue line spectra for PVC_ M1, with respect to the Ctrl_ M1 in black, since the NPs size goes below the resolution limit for FTIR microscopy and their concentration within the samples is low. Thus, one must disentangle the FTIR vibrational changes of the polymeric material from

those due to the cellular characteristic peaks of lipids (3050-2800 cm^{-1}), proteins (1700-1480 cm^{-1}), and nucleic acids (1300-900 cm^{-1}).

In Figure 16B**,** a zoom in the 3050-2800 cm^{-1} range, characteristic of the stretching C-H vibrations of aliphatic chains, is reported with the spectra of the NPs (dashed lines) overlapping those of the cells (solid lines). The spectra of the cells are characterized by a different absorbance: PP_M1 cells show a higher intensity band in this spectral region, but no CH_3 signals from the plastic can be directly appreciated (Table 1). PVC_M1 cells instead, show signals with a lower intensity than the Ctrl_M1 and the PP_M1 cells.

In Figure 16C is presented the 1800-1700 cm^{-1} spectral range, where it is possible to clearly identify the signal from C=O groups, either from the polar heads of lipids or from eventual oxidation by-products: I) 1737 cm^{-1} comes from C=O of esters of TAGs [69], while II) 1716 cm^{-1} signal refers to the C=O of the free fatty acids (FFAs) and/or aldehydes, and ketones [70].

From Figure 16C it is possible to appreciate that both NPs have no distinctive signals in this spectral region. In PP_ M1 spectra there is an increase of ~1737 cm^{-1} component of the C=O band in respect to the control cells, whereas in PVC_M1 there is an increase of ~1716 cm^{-1} band. Any unbalance between the carbonyl signal at ~1737 cm^{-1} and the ones from the aliphatic chains (C-H_x stretching) at 3050-2800 cm^{-1} could be caused by the presence of oxidative processes caused by the NPs exposure [71].

As previously described in Figure 16A-B**,** PVC_M1 cells are characterized by a lower intensity of the lipid bands (solid blue line at 3050-2800 cm^{-1}) with respect to the Ctrl_ M1 (solid black line), confirmed in Figure 16D where, the amides to lipids ratio is shown. The values of the ratio for PVC_ M1 is significantly higher than the one of Ctrl_M1. The present evidence can be better explained by observing Figure 17: from both optical image and FTIR maps, it is possible to notice that PVC_M1 cells look rounder and slightly thicker in the nuclear area. Instead, PP_M1 condition shows a slightly, yet significant (Table 2A), decrease of the amide/lipid ratio, with respect to the Ctrl_ M1. From Figure 17 the Ctrl_M1 are more adherent and spread onto the SiC windows (our substrate), thus the decrease of the amide/lipids ratio can be associated to an enhanced lipid synthesis [72].

In Figure 16E, the boxplot of the carbonyl/lipids ratio show that PP_M1 are characterized by a slightly higher value of the CO/Lipids ratio (check Table 2B for statistical significance of the data) that might be linked to oxidative stress conditions [71], [73], [74].

PVC_ M1 instead, revealed a lower ratio value than the one of the Ctrl_ M1, explained by the lower content of triacylglycerols (TAGs, band height at ~1737 cm^{-1}) with respect to free fatty acids (FFAs band height at ~1716 cm^{-1}). Indeed, in Figure 16F**,** the boxplot of the FFAs/TAGs ratio, for the tree conditions, has the opposite trend of the one in Figure 16E: lower value of the mean of PP_M1 (Table 2C for statistical significance of the data), could be due to a higher formation of TAGs, as confirmed by the Oil Red O staining, whereas PVC_M1 contain more FFAs.

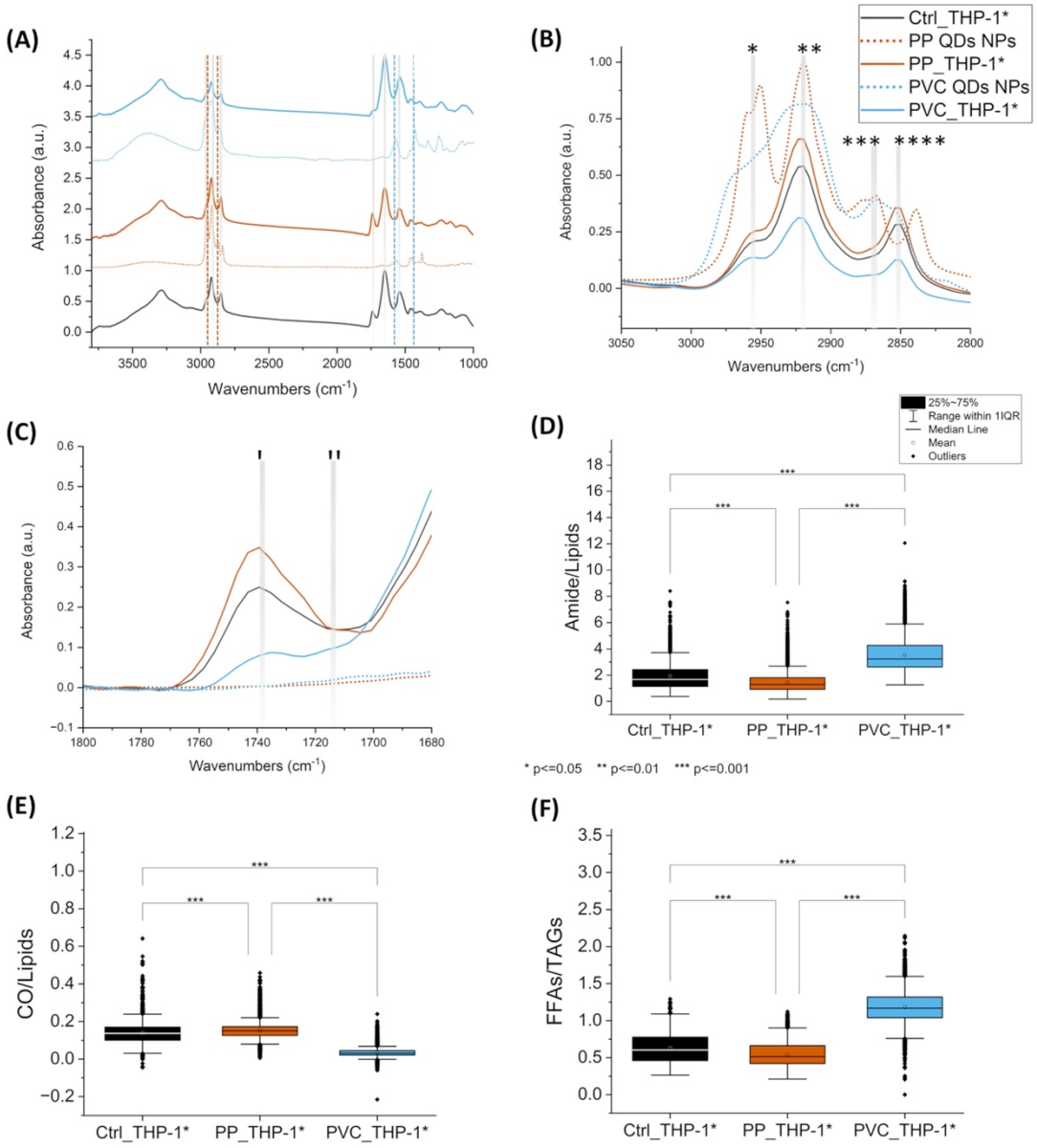

Figure 16. Average spectra of 10 µL of QDs-NPs (dashed lines) compared with average spectra of M1 macrophage cell (solid lines) treated with different QDs-NPs, offset for clarity, the dashed vertical lines represent the characteristic signals of the PP-QDs-NPs at 2950 cm^{-1} and 2870 cm^{-}

[1], in orange, and at 2920 cm^{-1} at 1568 cm^{-1} and at 1425 cm^{-1} for PVC-QDs-NPs, in light blue, that do not overlap strongly with those of the cells. Spectra normalized from 0 to 1 over the whole range A). Detail of the 3050-2800 cm^{-1} range, cut from panel A without offset, characteristic of lipids aliphatic chains signals: * CH_3 asymmetric stretching, ** CH_2 asymmetric stretching, *** CH_3 symmetric stretching and **** CH_2 symmetric stretching. Same color code of panel A B). Detail of the 1800-1680 cm^{-1} range, cut from panel A without offset, characteristic of lipids C=O ester signals: (I) ~1737 cm^{-1} C=O of esters of TAGs and (II) ~1716 cm^{-1} signal of the C=O of TAGs and/or aldehydes, same color code of the previous panels, solid lines spectra from cells and dashed lines polymers C). Box plot of the FTIR interested bands of the Amides over Lipids D), CO over Lipids E), and FFAs over TAGsF), $p < 0.001$, black *** and lines indicate significant differences calculated with Tukey method. Data are presented as box 25-75% range of the data, whiskers range within the 1st quartile, line: median line, square: mean, black diamonds: outliers.

Spectral range [cm^{-1}]	**Assignment**	**Corresponded biomolecule**	**Reference**
~2950	$v_{as}(CH_3)$	CH_3 asymmetric stretching PP-NPs	[75], [76]
~2870	$v_s(CH_3)$	CH_3 symmetric stretching PP-NPs	[75], [76]
~2920	$v_{as}(CH_2)$	CH_2 asymmetric stretching PVC-NPs	[77]
~1568	δ(C-H)	CH_2 bending PVC-NPs	[77]
~1425	δ(C-H)	CH_3 symmetric bending PVC-NPs	[77]
2945-2955	$v_{as}(CH_3)$	CH_3 asymmetric stretching mainly from lipids of THP-1_M_1	[78]
2920-2930	$va_s(CH_2)$	CH_2 asymmetric stretching mainly from lipids of THP-1_M_1	[78]
2845-2855	$v_s(CH_2)$	CH_2 symmetric stretching mainly from lipids of THP-1_M_1	[79]

~1737	ν(C=O)	CO stretching the esters mainly from TAGs	[69]
~1716	ν(C=O)	CO stretching mainly from FFAs and ketones and aldehydes.	[80]
1670-1614	Amide I: ν(C=O), ν(C-N), δ(N-H)	proteins: β-sheet structure at 1632, random coil structure at 1647	[81]
1568-1527	Amide II: ν(C-N), δ(N-H)	proteins	[82]
1481-1431	$\delta(CH_2, CH_3)$	proteins, lipids	[83]
1264-1202	$\nu_{as}(PO_2^-)$	DNA/RNA backbone	[84]
1105-1069	$\nu_s(PO_2^-)$	DNA/RNA backbone	[85]

ν – stretching, δ – bending; *s* – symmetric, *as* – asymmetric

Table 1. Main FTIR bands assignments.

A.

Sample name	Mean	SD	SE of Mean	Significance
Ctrl_M1	1.9324	1.07902	$2.074 \cdot 10^{-2}$	***
PP_ M1	1.45807	0.75558	$7.42 \cdot 10^{-3}$	***
PVC_ M1	3.52528	1.17231	$1.175 \cdot 10^{-2}$	***

B.

Sample name	Mean	SD	SE of Mean	Significance
Ctrl_ M1	0.13871	0.05845	$1.12 \cdot 10^{-3}$	***
PP_ M1	0.15206	0.04302	$4.22696 \cdot 10^{-4}$	***

PVC_ M1	0.03447	0.02141	$2.14638 \cdot 10^{-4}$	***

C.

Sample name	Mean	SD	SE of Mean	Significance
Ctrl_ M1	0.62756	0.19848	$3.82 \cdot 10^{-3}$	***
PP_M1	0.54593	0.25694	$1.54 \cdot 10^{-3}$	***
PVC_ M1	1.181	0.20791	$2.08 \cdot 10^{-3}$	***

Table 2. Tables reporting the results of the ANOVA analyses for the selected bands' ratio amide/lipids A), CO/lipids B), FFAs/TAGs C), used to generate the boxplots in figure 6 D-F. (SD: standard deviation, SE: standard error, ***: p value ≤ 0.001).

The commented results can be more easily appreciated in Figure 17, where the chemical maps of FFAs and TAGs are displayed for several groups of cells for the three conditions. In Ctrl_M1 and PVC_M1, the two types of fatty acids demonstrated to be comparably distributed and only few differences can be appreciated; on the contrary, in PP_ M1 hotspots of FFAs tend to cluster at the cytoplasmic level whereas the highest concentration of TAGs tend to accumulate in the cellular outer edge (white arrows in panels in Figure 17), as previously observed in the absorption and phase contrast images (Figure 14D). These considerations are more evident in the Figure 17, where the related RGB composite is reported, which combines the three aforementioned signals using the same range of the intensities (see caption) of the three maps of FFAs, TAGs, and Amides, normalized from 0 to 1, to favour a direct comparison.

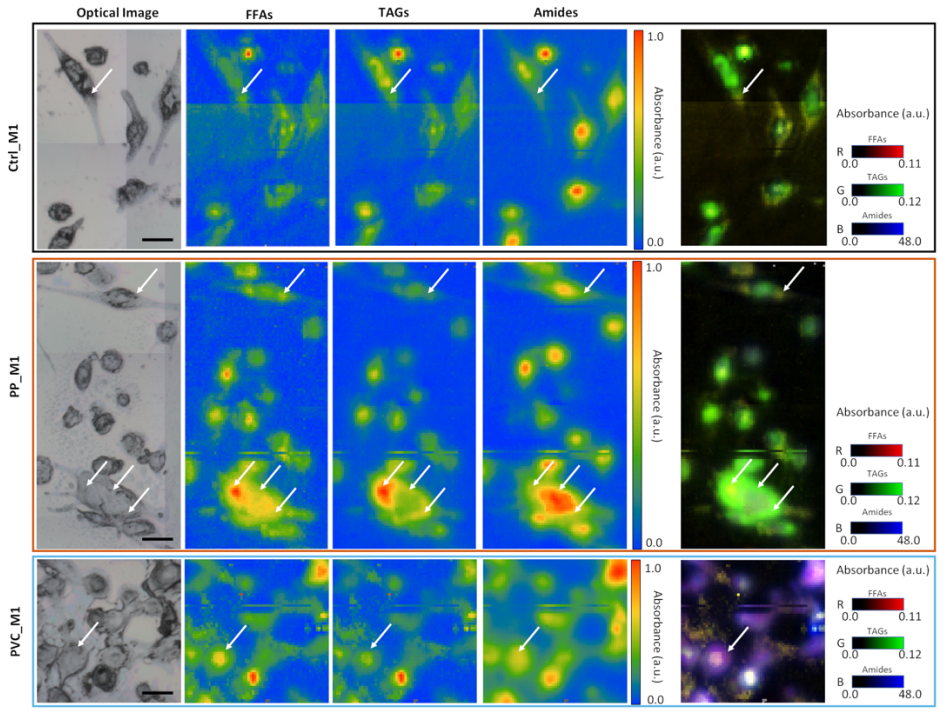

Figure 17 . Multipaneled figure representing some of the FTIR images acquired on the three samples. In the first line the CTRL_M1 cells (black border), in the second line the PP_M1 black, orange border) and in the third line the PVC_M1 cells (blue border). Each row has, from left to right, optical image of a sub area of the samples, chemical image of the free fatty acids (FFAs) obtained integrating the signal at 1716 cm^{-1}, chemical image of the distribution of triacyclglycerols (TAGs) obtained by calculating the peak height at 1737 cm^{-1} and the distribution of proteins, obtained by the integration of the amide I and II band in the 1700-1480 cm^{-1} range. For all these three (nine) panels the data have been normalized between 0 and 1 to better appreciate differences in distribution of the relative maxima (white arrows). In the fifth panel are placed the RGB composite images of the three channels previously described, not normalized, but presented with a common scale to better appreciate the variations of the relative intensities of the three signals. Scale bar is 50 µm.

To evaluate subtler differences induced by the treatments, not only due to variations on the content of specific chemical compounds, but also due to conformational or structural modifications, a PCA was performed on 2nd derivative of the absorbance spectra. In Figure 18A is presented the 3D scatterplot of the results of the PCA, with the scores plotted along PC1, PC2 and PC3. The Ctrl_ M1 are at the centre of the graph for all the axes, while PP_ M1 lean towards negative values for PC1 and PVC_M1 toward positive ones, respectively. The data separate mainly on PC1 as can be seen from Figure 18B; the graph was obtained by projecting all the points on PC1, allowing for a comparison of the mean values. The outcome shows that the three distributions are significantly different along PC1, which represents the 46.5% of the total variance of the dataset. Thus, the PCA analysis underlines a different response of macrophages according to the composition of NPs. In Figure 18C, the loading vectors, PC1 in red, PC2 in yellow, and

PC3 in blue are presented. The PC1 loading vector contains positive signals from lipids at 2920 and 2850 cm^{-1} in the CH stretching region, and at 1737 cm^{-1} of the C=O, meaning that they are stronger for PP_M1, average for Ctrl_M1 and lower for PVC_M1. PC1 showed protein related signals at 1647 cm^{-1} for amide I and at 1545 cm^{-1} for amide II, negative, meaning that their trend is the opposite of those of the lipids previously described. These protein signals can be assigned to unordered structures [86].

Even if of minor amplitude the three groups separate also along PC2 and PC3, which represent the 12.7% and 9.3% of the total variance of the dataset, respectively. PC2 separates mainly PP_M1 from the other two groups and the loading vector have the stronger signals in the protein region at ~1666 cm^{-1}, ~1568 cm^{-1} and the signal of the carbonyl at ~1743 cm^{-1}.

PC3 instead have the PVC_M1 in the negative hemispace and the PP_M1 in the positive one. The PC3 loading vector contains positive signals from lipids at 2927 and 2857 cm^{-1} in the CH stretching region, blue shifted in respect to those of PC1, possible attributed to less ordered lipids, more fluid membranes [79].

The signals in the C=O region are negative instead and are located at ~1737 cm^{-1} and ~1716 cm^{-1} of the C=O. PC3 contains proteins signals, as well, at 1632 cm^{-1} for amide I and at 1490 cm^{-1} for amide II, negative, which can be assigned to b-sheet structures [82], [86].

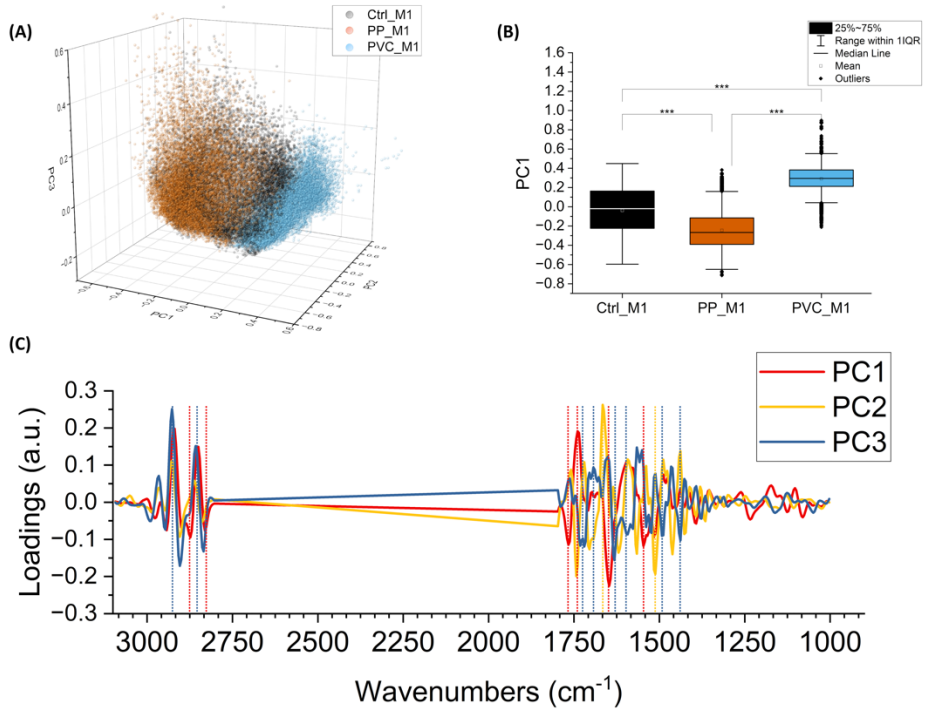

Figure 18. PCA analysis of components PC1, PC2 and PC3. PCA loading of the three components PC1, PC2, and PC3 (47.6 %, 12.0 % and 9.3 % of the samples variance, respectively). Ctrl_M1 are colored in black, 20 µg/mL QDs-PP and QDs-PVC exposed macrophage M1 cells in orange and light blue, respectively A). Boxplot of PC1 scores, same color code of the previous panel, ***p < 0.001, black * and lines indicate significant differences calculated with Tukey method. Data are presented as box 25-75% range of the data, whiskers range within the 1st quartile, line: median line, square: mean, black diamonds: outliers B). PC1, in red, PC2 in yellow, and PC3, in blue, loading vectors obtained from the PCA. Dashed lines represent the most relevant spectral features for each component C).

2.3 Discussion

Although occurrence of MNPs has been demonstrated in human blood [87], intestinal tract [88], immune system [89], [90], the toxicological accumulation mechanism in human cells is still poorly understood. This mainly depends on the difficulties in the identification, localization, and characterization of the polymeric particles due to the analytical interference with macromolecules, such as lipids, proteins, and nucleic acids, especially at small size (nm), and low concentration (µg/mL), making investigation of their related toxicological accumulation rather challenging.

For this reason, there is a high demand of both *in vitro* studies to develop the detection of fingerprints of toxicity as well as the synthesis/use of model environmental nanoplastics. Most of studies are currently using NPs labelled with fluorescent probes (gold nanoparticles, fluorophores, quantum dots) [51], that allow identifying NPs at the

cellular level by exploiting the optical properties of the linkers (i.e., fluorescence). The scientific literature rarely reports the synthetic procedures for the most common nanoplastics abundant in the environment (i.e., PP, PVC); in fact, nano-, and micro-polystyrene beads are often commercially purchased to conduct most laboratory studies [80], [91].

In the present study we propose the use of CdSe QDs labelled PP-, and PVC- NPs, as a suitable model for representative environmental NPs, and THP-1 cell line, surrogate of macrophages, for immune-toxicological studies [92]–[94].

Cassano *et al.* already demonstrated that these NPs can be tracked by the red bright fluorescence properties of QDs [52].

The light fluorescence microscopy was extremely supportive to visualize the NPs across the cell samples, by focusing on the bright, tuneable, red spots (Figure 13). However, a more sensitive and higher resolution combination of analytical techniques would be highly beneficial to overcome the cellular auto-fluorescence, typical of macrophages and exogenous material, that interferes with the detection, demonstrating that the use of fluorophores is not always a successful strategy for this aim [95].

To overcome that, Soft X-Ray Microscopy combined with LEXRF at TwinMic beamline (Elettra Sincrotrone Trieste, Italy), permits to acquire the X-ray fluorescence photons of Se, one of the two components labelling NPs, together with the chemical map distribution of low-Z elements (C, O, Na, and Mg) at sub-micron spatial resolution (Figure 14 and Figure 15). The simultaneous absorption and phase contrast images acquisition provided an additional information on the cellular morphology. At such chemical and sub-micron spatial resolution, it is possible to track the NPs, and identify their location across the cells. From the results reported in Figure 14 and Figure 15 it is possible to speculate that NPs of both compositions are up taken by macrophages, and heterogeneously dispersed intracellularly, apparently not forming substantial clusters onto the cell surface, excluding a simple NPs precipitation.

Although there is no significant difference in the NPs distribution dependent on the polymer composition, peculiar structural changes were evidenced after 72 h NPs-exposure in absorption and phase contrast images.

CdSe-QDs PP-NPs seemed to induce an increase of bright vesicles in the cytoplasm (Figure 14C) or at the plasma membrane level, better appreciated by the corona formation (Figure 14D). On the contrary, these bright vesicles were not visible in the CdSe-QDs PVC-NPs treated cells (Figure 15), but the presence of depressions across

the cytoplasm, with respect to the control (Figure 15A), underlines a different response of macrophages, based on the different polymer composing the NPs.

Those bright vesicles resulted to be LDs by performing a laboratory assay, the Oil Red O staining test (Figure 12), indicative of the phagocytosis activation and consequent oxidative stress, already demonstrated for this cell model [96].

On the other hand, although LDs were not clearly visible in the PVC-treated cells by phase contrast images, their increase content was inferred by the lipidic test.

The accumulation of lipids was quantified by measuring the absorbance at 450 nm after 24-72 h (Figure 12). At 24 h time point, the results interestingly report the gradually increase of lipid contents in accordance with the NPs concentration, ranging from 0 to 100 μg/mL, for both NPs. As expected, after 72 h, the enhancement of LDs was still occurring in treated cells, but above 20 μg/mL concentration of PP-, and PVC- NPs, the number of available macrophages is compromised by the apoptotic process and the higher quantity of NPs at this point starts to interfere with the results. This one more confirms the reason beyond the use of the selected concentration for the present studies (20 μg/mL). The results suggest the capacity of NPs to enhance the number of lipid droplets, which may be an early stage for further toxicological lipid metabolism impairment, even by not exerting a significant cellular cytotoxicity upon NPs incubation (Figure 11).

To support the observations described above, the FTIR technique was exploited to provide unique chemical vibrational information on lipids, protein structure, nucleic acids at a micrometric spatial resolution [97].

By the observation of the spectra in Figure 16A-C, it is difficult to directly identify the contributions of the polymeric NPs which, for example, are expected to have strong signals in the regions of aliphatic chains stretching absorption (3050-2800 cm^{-1}). Therefore, the aim of the present work consisted of investigating the effect of the polymeric materials, by looking for cellular macromolecular changes when in close contact with the NPs. The univariate data analysis showed indeed variations in lipids and proteins bands upon incubation with the different NPs (Figure 16A-C). By the analysis of the chemical images from Figure 17, it is possible to correlate also how these variations in intensity, correspond to different distribution of lipid and proteins components within the three population of cells, reflecting also changes in their morphology induced by the treatments. PVC_M1 appear rounder and thicker whereas

Ctrl_M1 and PP_M1 are thinner and adherent to the substrate; nevertheless, observing the TAGs distribution of this latter group is possible to observe the accumulation of lipid droplets in the outer edge of the cytoplasm. The lipid related chemical modifications was also evidenced with standard laboratory test (Oil Red O staining, Figure 12) and confirmed by advanced analytical tools such as STXM (Figure 15 and Figure 16). The treatment with NPs could cause the cell to respond with an increasing of oxidative processes. From the CO/lipids ratio depicted in Figure 16E, it can be slightly appreciated a high contribution of CO in PP_M1 cells, on the contrary a lower ratio in PVC_ M1 macrophages is demonstrated, which might be mainly related to an increased FFAs and membrane disruptive processes [98].

In Figure 16 panels C and F it is better represented the NPs impact on the FTIR bands of the carbonyl group at 1737 cm^{-1}. It is clearly evidencing the oxidation of the aliphatic chains of the i.e., phospholipidic bilayer, at different levels of oxidation process depending on the different NPs. The chemical formula of the NPs is surely determinant for the cellular response, in fact, the PVC-NPs is more hydrophobic, with respect to the PP-NPs, due to presence of the halogen (-Cl), which protects the nanoplastics from a potential hydroxyl radical attack, thus it seems to preferably attack the cellular membranes [99].

Based on that, the PVC_ M1 curve in Figure 16C, show the consequent effect in the increase of aldehydes and ketones products (1716 cm^{-1}). The PP_ M1 curve instead, suggests a more advanced oxidative stress, that leads to the formation of the CO in the cellular structures, a process confirmed by the high absorption band typical of carboxyl group (1737 cm^{-1}) [100].

From the multivariate analysis all the variations in the second derivative spectra are taken in consideration at one glance, therefore it is possible to appreciate finer changes in the macromolecules peaks that are caused by the NPs. From the scatterplot of the PCA analysis in Figure 18A-B it is possible to conclude that the two types of nanoplastics surely affect the cells, but causing different responses, as can be seen by the clear separation of the three datasets along PC1, with the controls in the centre. This component represents at the same time variations in lipid content and structure and in protein folding, since it can be appreciated the increase of random structures and β-sheet aggregates in treated cells, signals that often correlate with cellular suffering [101] and apoptotic processes [98].

In conclusion, advanced analytical techniques, XRF accurately detected the NPs presence across the macrophages at high spatial resolution and evidenced morphological changes which were further analysed by staining based- laboratory techniques. The chemical changes related to lipid metabolisms impairment induced by NPs were better resolved by FTIR spectro-microscopy.

2.4 Conclusions

Based on the growing scientific concern of environmental nanoplastics (NPs) human exposure and the challenging issues in the assessing of the polymeric material in biological samples, we propose the use of labelled CdSe QDs-polypropylene, polyvinyl chloride NPs (PP, PVC, respectively) as a model to investigate the NPs-immune system interactions.

To this aim, it has been crucial the use of advanced microscopy techniques, particularly X-ray fluorescence microscopy to accurately detect the NPs across the macrophages, by following the Se (L-line) X-ray emission peak, which was in good agreement with the observations of light fluorescence microscopy.

Besides, Scanning Transmission X-ray Microscopy imaging provided the cellular morphological changes in exposed macrophages M1, and unravelled the increase of bright lipidic vesicles mostly at the cellular plasma membrane, suggesting the involvement of lipid metabolism in the toxicological response. FTIR microscopy demonstrated to be an optimal tool to better disclose the NPs induced chemical modifications in macromolecular components of the cells, specifically in lipid response: the FTIR fingerprints clearly revealed the different response of PP- and PVC-NPs exposure, causing an increase of triacyclglycerols or free fatty acids in macrophages, respectively. In addition, PCA analysis on 2nd derivative of FTIR absorbance spectra evidenced subtler differences induced by the different treatments according to the chemical composition of the plastics, such as the structural changes in the protein components.

Based on the present results, a deeper study will be conducted to exactly characterize the NPs-lipids, and NPs-protein interactions approaching lipidomic and proteomic technologies. Moreover, the advanced multi-technique approach presented in this work,

will be a model for future *in vitro* investigations focused on further specific accumulation effects of prenatal and postnatal MNPs exposure.

Moreover, even if the proposed approach allows for a description of MNPs internalization and its chemical and structural consequences on the selected cell line (THP-1), a more comprehensive demonstration of MNPs cellular effects could be completed using 3D imaging techniques, such as tomography.

The present approach has been set up and finalised, thus it could be applied to further cell line models in the reproductive field.

CHAPTER 3 – Synthesis of Carbon Dots labelled polypropylene nanoplastics

In order to work with an additional model of polypropylene nanoplastics, it was decided to synthetize polypropylene nanoplastics labelled with carbon dots. This activity was performed during a Ph.D. period at the Department of Chemical Sciences, Dublin City University as part of the research group led by Professor Silvia Giordani. Specifically, Carbon Dots (CDs) and Boron-Nitrogen Carbon Dots (BN-CDs) were synthesized starting from Carbon Nano Onions (CNOs) and Boron-Nitrogen Carbon Nano Onions (BN-CNOs) already present in the laboratory, by following a top-down approach developed by some of the group members [102].

Based on the previous evidence of the effects of polypropylene nanoplastics on the immune system [103], this polymer was chosen to be used as an additional model of nanoplastics.

The as-produced CDs (CDs, BN-CDs) were characterized by the following described techniques to compare their properties and choose those that best fit our need: the synthesis of CDs-labelled Nano-plastics (NPs). To this aim, the CDs fluorescence properties were accurately measured to be exploited in imaging of NPs in biological matrix.

In particular, we expect that the presence of carbon dots will not alter the specific toxicity of nanoplastics. Those as-synthetized NPs would be ideal as NPs models to be used in both *in vitro* and *in vivo* studies, concerning endocytosis, accumulation, and related toxicological effects upon human exposure *via* inhalation, ingestion, and skin contact.

3.1 Carbon Dots

Carbon dots (CDs) are a promising class of carbon nanomaterials which have attracted attention in the fields of biomedicine [104], photocatalysis [105], sensing [106], optoelectronics [107], and energy conversion due to their fluorescent and luminescent properties [108].

CDs are typically smaller than 10 nm in size, and they are usually inexpensive to make, and have good biocompatibility and high photostability [109].
These properties give CDs excellent nanocarrier potential for anticancer drugs, and they showed potential advantages over other nanoparticles and liposomes.
Specifically, they are mostly composed by carbon, which is a nontoxic element, and it is also present in biological components, overcoming toxicological concerns in bio-applications. In addition, compared to other nanoparticles, CDs are characterised by a higher aqueous solubility, chemical inertness, easy surface modification and low tendency to photobleaching and photo blinking [110]. In fact, CDs are usually selected as optimal candidate for fluorescence probes to be tracked in cells under imaging technique, taking advantage of their characteristic fluorescence brightness at the individual dot level [111].
Carbon dots were synthetised for the first time in 2004 by Xu *et al*. in a research team at the Department of Chemistry and Biochemistry at the South Carolina University. During the purification of single-walled carbon nanotubes obtained from arc-discharge soot, and through an electrophoretic method they isolated a mixture of fluorescent nanoparticles [112]. Two years later, Ya-Ping *et al*. obtained carbon dots via laser ablation using water vapor and argon as carrier gas. The CDs were synthetised starting from a mixture of graphite powder and cement and they turned out to be nanoparticles in aggregates of different size [113].
CDs contain sp^2/sp^3 carbon and oxygen/nitrogen-based group or polymeric aggregations. Therefore, they can be classified into graphene quantum dots (GQDs), carbon nanodots (CNDs), and polymer dots (PDs). GQDs show one or more graphene layers with oxygen-based functional groups at the edge; CNDs are spherical and can be carbon nanoparticles, or CQDs, which are characterised by a crystal lattice. PDs instead, are prepared from polymers or monomers and can be aggregated or cross-linked. The carbon core and the linked polymer chains can form PDs by self-assembling [114].
Although the fluorescence mechanism of CDs is not fully explained, it has been widely accepted that during the multiple synthetic processes of the nanomaterials, such optical property can be achieved despite the fact that the starting material is usually not fluorescent [115]. Fluorescence can be attributed to the surface passivation with different ligands or additives [116], the presence of multi-emission centres [117], or the solvation interactions [118].

Among the proposed fluorescent-based mechanisms, it is stated that photoluminescence (PL) properties arise from the sp^2 hybridized carbons formed in the synthetic route, which create a conjugated π–domain. The band gaps transitions in the internal π region is described as "carbon core state" and are responsible of the fluorescence emission of CDs. The optical properties are dependent on the nanoparticle size as demonstrated by Lee *et al*. and resulted to go from UV towards visible and near infrared. Thus, it allows the selection of the CDs based on the scientific purpose [114].

Another strategy to control the CDs properties consists of linking CDs to the graphitic layers, which can lead to a red-shifted emission. As demonstrated by Hola *et al*., this was possible by gradually increasing the amount of nitrogen, which caused a higher graphitic nitrogen content into the CDs carbon lattices generating a defect band between the highest occupied molecular orbit (HOMO) and the lowest unoccupied molecular orbit (LUMO) band gaps [119]. In addition, the red-shifted PL emission of CDs can be achieved doping the nanoparticle surface with nitrogen and sulphur elements, as described by Do *et al.* [120].

The CDs' optical properties are additionally determined by the surface defects states, which refer to the spherical structure delimited by the separated internal CDs core. The as-called outer spherical shell may undergo surface passivation with functional groups, including oxygen-based. Different surface defects are created through a gradual oxidation of CDs, and this leads to the presence of emissive excitons, thus more emission sites [121]. Recently, Lin *et al.* synthetised three types of CDs with red, green, and blue colour of fluorescence staring from different carbon precursors [122]. Pang *et al.* obtained differently fluorescent CDs by adapting the reaction conditions [123].

CDs excitation wavelength-dependent emission allows for CDs use in optical bioimaging and bio-sensing [124], [125], overcoming the complex synthesis, poor photostability, and poor water solubility of organic fluorescent dyes, such as rhodamine, fluorescein, squaric acid, diketopyrrolo-pyrrole [126].

The outstanding applicability of CDs in cellular imaging *in vitro* models has been widely reported in the scientific literature. Zhang *et al*., used citric acid and propylene diamine as precursors to synthetise nitrogen doped CDs (N-CDs). The as-synthetised N-CDs showed a concentration-dependent multicolour photoluminescence, which was exploited in HeLa cell study, as fluorescent probe to image their penetrance in the nucleus. It resulted to be an optimal approach to track individual cells and image

nuclear-based processes, i.e., nuclear marker-based mitosis [126]. Moreover, Guo *et al*. synthetised fluorescent CDs through a microwave-assisted synthesis to be used as tool to investigate the cell viability *in situ*. Mitochondrial membrane potential (MMP) in healthy cells is negative, thus positive charged CDs accumulate in the organelles due to electrostatic interactions. In non-healthy conditions, the decrease in MMP levels triggers the CDs migration from the mitochondria to the nucleolus, where they bind the nuclei acids. Therefore, the distribution of CDs across the cellular organelles can be a direct information on the cellular survival state [127].

Based on these considerations, under the supervision of Prof. Silvia Giordani and in collaboration with her research group, the synthesis of two types of CDs, namely p-CNOs CDs and p-(BN)CNOs CDs, was performed with the aim of using them as fluorescent probes to label nanoplastics for *in vitro* accumulation studies by imaging techniques.

3.2 Synthetic strategies of Carbon Dots synthesis

There are two main approaches to achieve the synthesis of carbon dots: a) the top-down, and b) the bottom-up methods. The top-down way consists in the cleavage and exfoliation of larger carbon precursors like graphite, activated carbon, carbon nanotubes, carbon fibres, and coal to nano-size, through oxidative treatments [128], [129], electrochemical oxidation [130], [131], laser ablation [132], ultrasonication [133], [134], ball milling [135]–[137], and arc-discharge [112]. For instance, as mentioned above, in 2004, Xu *et al*. synthetised for the first-time carbon dots *via* the purification of single-walled carbon nanotubes obtained from arc-discharge soot. The top-down has two main advantages: the possibility to scale up the method for the CDs synthesis, and the possibility to produced homogenous CDs [138], [139]. On the other hand, the bottom-up methods involve the molecular precursors such as citric acid, glucose, fructose, which can undergo processes like microwave synthesis [140], ultrasonication [141], [142], electrochemical [143], hydrothermal [144]. However, these approaches may lead to the production of side products, which require further purification.
A summary of both top-down and bottom-up approached to synthesise CDs is depicted in Figure 19.

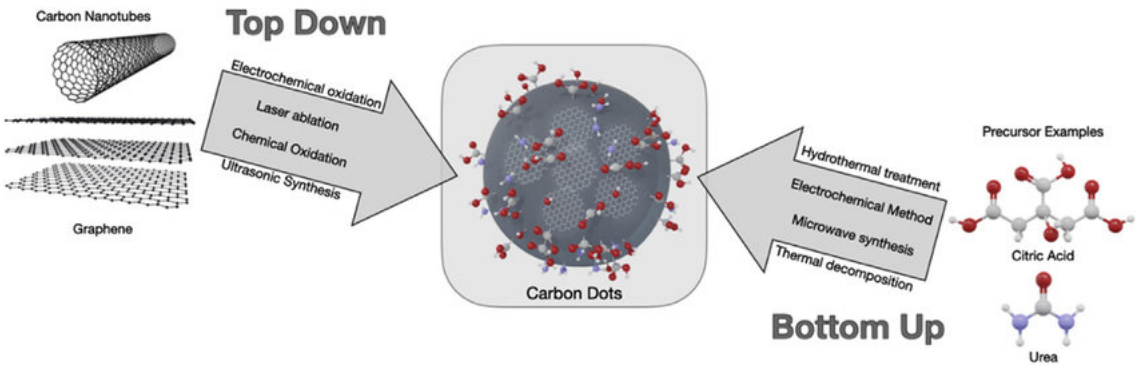

Figure 19. Illustration of top-down and bottom-up approaches to synthesise Carbon dots [145]

Among the several top-down methods, the chemical oxidation of carbon nanomaterials is one of the most common synthetic routes performed to obtain fluorescent CDs. The oxidative method is also known as oxidation cutting, and it involves the breakdown of the carbon bonds of the precursors graphene oxide or sheets, coke, carbon fibres by the sulphuric acid (H_2SO_4), nitric acid (HNO_3), and potassium permanganate ($KMnO_4$), etc., used as oxidation agents [146].

As an example, C. Zhou *et al.* fabricated soluble graphene quantum dots from graphene oxide through a green approach, using sodium polystyrene sulfonate as dispersant and L-ascorbic acid as reducing agent. The as-produced GQDs (5-15 nm) beside having an excitation-independent photoluminescence activity, with the maximum emission wavelength at 470 nm, showed also a high ability in the electrochemical sensing of heavy metal ions [147]. In addition to graphene or graphene oxide, also carbon nano-onions can be utilised to synthetise CDs. For instance, Y. Liu *et al.* synthetised ultraviolet and blue emitting CQDs through the chemical oxidation of carbon nano-onions [148].

Oxidative treatment is simple and effective in the fabrication of carbon dots, although green synthetic approaches have been developed in the recent years [149]–[152].

Adopting the oxidative approach, carbon nano-onions synthetized by Dr. Adalberto Camisasca and Hugh Mohan in the Prof. Silvia Giordani group were used as precursors for the synthesis of carbon dots and boron-nitrogen carbon dots.

3.3 Material and Methods

3.3.1 General synthetic route of carbon dots

To collect consistent data, all the reactions were carried out using the same methods and procedures, trying to eliminate as many variables as possible.
The products are named by the operator's name and surname initials (FZ), followed by the number of batches in an increasing number way (1, 2, 3, etc.) and listed in Table 3. Therefore, the synthetic method for FZO1, FZ02, FZ03 and FZ04, FZ05, FZ06 was kept consistent for each of the two groups (carbon dots, and nanoplastics, respectively). The general synthetic route used to produce carbon dots is following described and depicted in the Figure 20.

Batch	**NPs type**	**NPs characterization/Reagents**
FZ01	CNO-CDs	UV-Vis, DLS, zeta potential, fluorescence, TEM, ATR-FTIR
FZ02	CNO-CDs	UV-Vis, DLS, zeta potential, fluorescence, TEM, ATR-FTIR
FZ03	BN-CNO-CDs	UV-Vis, DLS, zeta potential, fluorescence, TEM, ATR-FTIR
AC36	p-CNOs	Starting material
HM03	p-BN-CNOs	Starting material

Table 3. List of the synthetised products/starting materials and related information.

The starting material, CNOs for FZ01 and FZ02, BN-CNOs for FZO3 (50 mg) was weighed accurately on a microbalance. In a fume hood, 10 mL mixture of 3:1 v/v Sulphuric Acid:Nitric Acid (7.5 mL and 2.5 mL, respectively) was prepared in a 50 mL rounded bottom flask. The acid solution was gently transferred to the flask placed in an ice-bath to limit the development of heat and fumes. The mixture containing the carbon nano-onions was left to cool down to 10 °C and sonicated for 2 hours at 37 kHz using a Fisher Scientific FB 15050 Ultra-sonic Bath to promote the fragmentation of the carbon material. Then, the reaction was refluxed at 100 °C for 3 hours under stirring conditions. After the reaction ended, the flask was left to cool down to room temperature. The solution was diluted with 20 mL of deionised water and neutralised using NaOH 8M. The neutralisation step was performed by adding small amounts of NaOH solution with

a glass pipette and checking the pH using a universal indicator paper, until a neutral green colour was observed. During this step the formation of salts, Na_2SO_4 and $NaNO_3$, was promoted placing the flask in an ice-bath and left overnight.

Afterwards, carbon dots were isolated from the neutralised solution through placing a folded filter paper (110 mm) in a funnel. The final dark brown solution was filtered with a 0.20 μm pore size Nylon filter to get rid of the unreacted starting material and impurities.

To remove the excess of salts still present in the dispersion, 10 mL of the filtered product was dialyzed using 1kDa Pur – A – Lyzer Mega dialysis kit (Sigma-Aldrich). A 1 L beaker was filled with deionised water and the dispersion was kept under constant stirring for 24 hours. The solution medium used for the dialysis was changed tree times, after 2 h, 5 h and overnight, to remove as much excess salts as possible.

Once the dialysis step was completed, the sample was recovered, transferred into a glass vial, properly labelled as reported in Table 3, covered with aluminium foil, and stored in the fridge. The samples were characterised through UV-Vis Spectroscopy, Dynamic Light Scattering and Zeta Potential at the School of Chemical Sciences of Dublin City University, while fluorescence spectroscopy was carried out at the Nano Research Facility based on DCU campus using the instrumental settings described in the following paragraphs. The data were analysed using GraphPad 9 software.

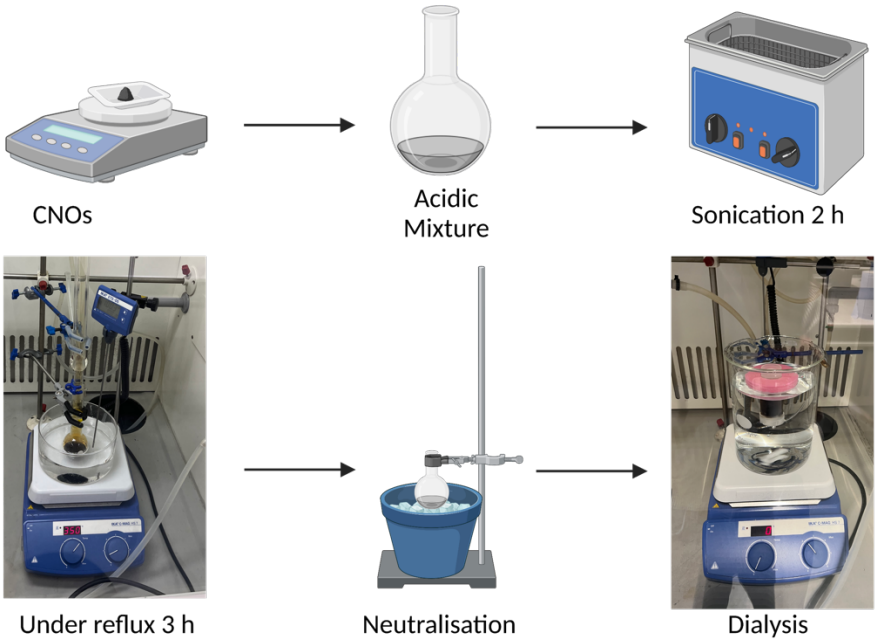

Figure 20. Visual representation of the carbon dots synthetic route from carbon nano-onions created with BioRender ©.

In addition, acetone-driven precipitation was used to try to achieve the CDs purification. To do so, after the filtration with the Nylon filter, 10 mL of the sample was added to the same amount of acetone in a centrifuge tube, until the precipitation of CDs was visible. The precipitate was repetitively washed with acetone until the supernatant resulted clear and dried. Despite several attempts, and different approaches the final product still contained visible salts not successfully separated from the brown CDs. Therefore, from the next reaction on the dialysis procedure was the only method performed for the purification of CDs.

3.3.2 General synthetic route of labelled nanoplastics

The protocol for the synthesis of carbon dots labelled polypropylene nanoplastics was based on the oil-in-water emulsion technique developed by Dr. Cassano *et al.* and described in the cited paper [52]. The synthetic route adopted is visually summarised in the Figure 21 and the products are listed in Table 4.

Batch	**NPs type**	**NPs characterization**
FZ04	CDs PP-NPs	TEM, ATR-FTIR

FZ05	CDs PP-NPs	TEM, ATR-FTIR
FZ06	BN-CDs PP-NPs	TEM, ATR-FTIR
PP	Polypropylene pellet	TEM, ATR-FTIR

Table 4. List of the synthetised products/starting material and related information.

For this purpose, 30 mg of polypropylene (12 kDa) was weighted on a microbalance and transferred into 3,5 mL of toluene in a 50 mL rounded bottom flask. The mixture was placed on an oil bath and heated at 100 °C for 1 and half hour under continuous stirring, to induce the pellets dissolution. Separately, 8 mg of sodium cholate was weighted and completely dissolved in 27 mL boiling deionised water.

To achieve the synthesis of carbon dots labelled polypropylene nanoparticles, 200 µL of CDs (FZ03 for FZ04, FZ01 for FZ05, FZ02 for FZ06) was filtered through a 0.2 µm pore size Nylon filter and added to the hydrophobic phase (toluene) just before the addition of the hydrophilic part. The resulting mixture was stirred and let to cool down to 20 °C to prevent instrumentation damage for the following step.

The two-phase system was ultrasonicated using the Branson Digital Sonifier SFX 150 with a microtip at the Department of Biotechnology of DCU. The instrumentation settings I operated at were as follow:

- 40 % of amplitude for 2 min in continuous modality mode
- 20 % of amplitude for 2 and half minutes in continuous modality mode

After ultrasonication, the emulsion was placed in an ice-bath and let to cool down for 3 minutes. The resulted milky coloured product was filtered by a qualitative paper with a particle retention of 5-13 µm to get rid of the agglomerated/nano emulsified polypropylene. Then, the solvent was evaporated through rotary evaporator and reduced to 5-10 mL.

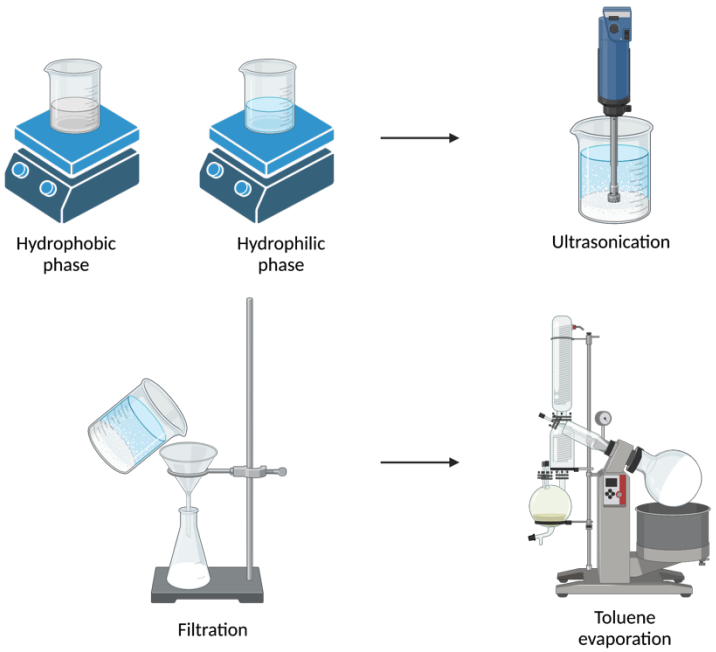

Figure 21. Visual representation of the carbon dots labelled nanoplastics synthetic route from carbon nano-onions created with BioRender ©.

3.3.3 Chemical information

Sodium Hydroxide (NaOH), Nitric Acid (HNO_3), Toluene, polypropylene (PP), sodium cholate reagents and solvents used for the experimental activity were purchased from Sigma Aldrich, while Sulfuric Acid (H_2SO_4) was obtained from Fisher Scientific. Common bench – grade reagents (Acetone and Methanol) were purchased from Brenntag Ireland.

3.3.4 UV-Vis Spectroscopy

UV-Vis absorption analysis was carried out using a Shimadzu UV-1800 instrument for all the presented work. The samples were measured in a 1 cm path-length quartz cuvette and diluted 1:10 with deionised water. The absorbance of the blank with deionised water was recorded as well in the UV-Vis scan range 800-190 nm. No baseline correction was taken. Due to time restriction FZO4, FZ05 and FZ06 were not measured. Absorption spectra were extracted with GraphPad 9 software.

3.3.5 Dynamic Light Scattering and Zeta Potential

Dynamic Light Scattering (DLS) and zeta potential analyses were performed using a Malvern Zen 3600 Zetasizer. The samples were measured in a 1 cm path-length quartz cuvette and diluted 1:10 with deionised water and filtered with 0.2 μm pore size polyether sulfone filter. For each sample, the average of 6 recorded measurement repetitions was considered. Absorption spectra were plotted with GraphPad 9 software.

3.3.6 Fluorescence Spectroscopy

A Perkin-Elmer Fluorescence Spectrometer LS55 was used to carry out the reported measurements, using a 1 cm path-length quartz cuvette. The samples were diluted 1:10 with deionised water. Due to time restriction FZ04-FZ06 were not measured with this instrument. Fluorescence excitation spectra were acquired at 510-530 nm excitation scan range, and an excitation slit of 4.5, instead the fluorescence emission spectra in 350-800 nm, with an emission slit of 7.5. The fluorescence intensity cut off 1000 a.u. The scan speed was 1200 nm/min, and 5 scan accumulation were recorded using FL WinLab software.

3.3.7 Transmission Electron Microscopy

The topography, morphology, and size of the carbon dot dispersions and labelled nanoplastics were characterized using a Transmission Electron Microscopy Philips CM10, operated at 80 kV. The nanomaterials were drop casted on the 75-mesh Formvar coated gold grids, negatively stained with phospotungstic acid (PTA) (2%, pH 7) or lanthanides, and air dried before imaging.

3.3.8 Attenuated Transmission Reflectance Microspectroscopy

Spectra of the carbon dots and nanoplastics were collected in ATR mode at the infrared beamline SISSI-Bio at Elettra Sincrotrone Trieste [67].
Data were acquired using a VERTEX70 interferometer (Bruker Optics Billerica, MA, US), equipped with a single reflection MIRacle ATR accessory, with a diamond Internal

Reflection Element (IRE), a KBr beamsplitter and a DTGS detector (Deuterated TriGlycine Sulphate). Each measurement is the average of 128 scans in the range 4000-500 cm^{-1} setting the interferometer scanner speed at 10 kHz, with a spectral resolution of 2 cm^{-1}. The Fourier Transform was carried out using a Blackman-Harris 3-Term apodization function and a zerofilling factor of 2. Data were collected and preprocessed using OPUS 7.5 software (Bruker Optics, Billerica MA US) and plotted using Origin Pro 2023 (Originlabs) after 0-1 normalization.

3.4 Results

During the Ph.D. visiting research stay at the School of Chemical Sciences, several samples were synthetised and characterised. The starting materials were already present in the laboratory and were previously synthesised by Prof. Silvia Giordani research group: purified carbon nano-onions and boron-nitrogen carbon nano-onions. The obtained carbon dots and boron-nitrogen carbon dots were used as starting material for the synthesis of labelled polypropylene nanoplastics. All the carbon dots were characterised by absorption, fluorescence spectroscopies, dynamic light scattering, zeta potential, and transmission electron microscopy. All the labelled nanoplastics instead, were characterised by transmission electron microscopy and attenuated total reflectance micro-spectroscopy (time restriction reason).

3.4.1 Characterization of carbon dots from purified carbon nano-onions

In this section results will be reported starting from the duplicate of synthesised carbon dots (FZ01, FZ02 code name) from the same source of carbon nano-onions (sample code AC36)*, followed by the characterization of the batch code FZ03, which refers to boron-nitrogen carbon dots obtained from the boron-nitrogen carbon nano-onions (HM).*

Carbon dots (FZ01), prepared starting from carbon nano-onions (sample code AC36) through oxidative treatment, was characterised by UV-Vis spectroscopy to investigate the CDs absorption properties. The analysis of the absorption spectrum, reported in Figure 22, shows that CDs present a tail in the visible range of wavelengths 400 – 800 nm, while a higher absorption in the UV region (< 400 nm). As appreciable in the graph

below, there is a peak at 230 nm and a shoulder at 265 nm, with an absorbance of 0.5 and 0.4, respectively. The absorption values in the spectrum are correlated to the π–π^* transitions of C=C bonds and n–π^* transition of carboxyl moieties (C=O), which are the most common groups absorbing in CDs spectra. The as-produced CDs characterisation results are in good agreement with the data published in the paper by A. Ventrella *et al.* [102], therefore demonstrating the reproducibility of the described method.

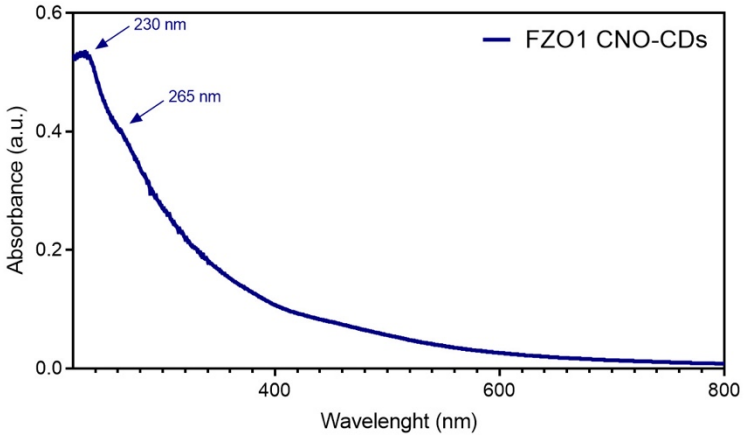

Figure 22. UV-Vis spectrum of 1:10 diluted aqueous solution of CNO-CDs.

To investigate the size distribution of the CNO-CDs sample (FZ01), the dynamic light scattering technique was performed using the instrument settings described in the section 3.3.5 The analysis summarized in the graph in Figure 23 reports the size in nanometre against the intensity distribution. The average diameter size is 7.840 nm and the peak attributed to the CDs can be observed in a range between 1-10 nm, with a 4% intensity.

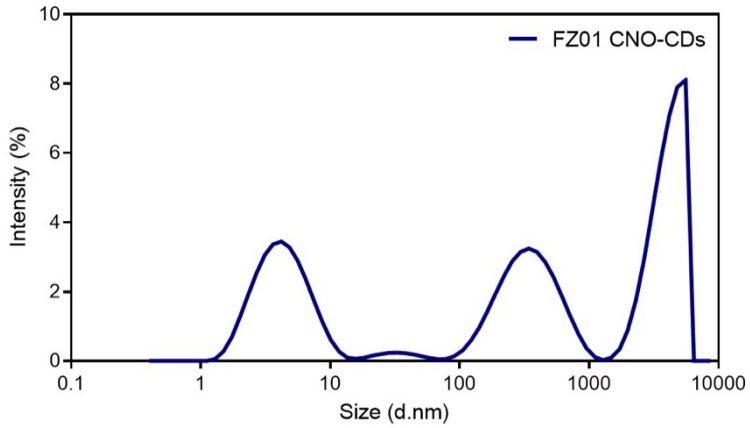

Figure 23. DLS spectrum of 1:10 diluted aqueous solution CNO-CDs.

To get rid of larger particles (>10^3 nm), several attempts were made, and among those, the successful method resulted to be the centrifugation firstly at 3000 rcf (relative centrifugal force) and secondly at 2000 rcf, each for 5 minutes. The sample was then sonicated for 15 minutes to favour the disaggregation of larger particles and characterised as shown below in Figure 24.

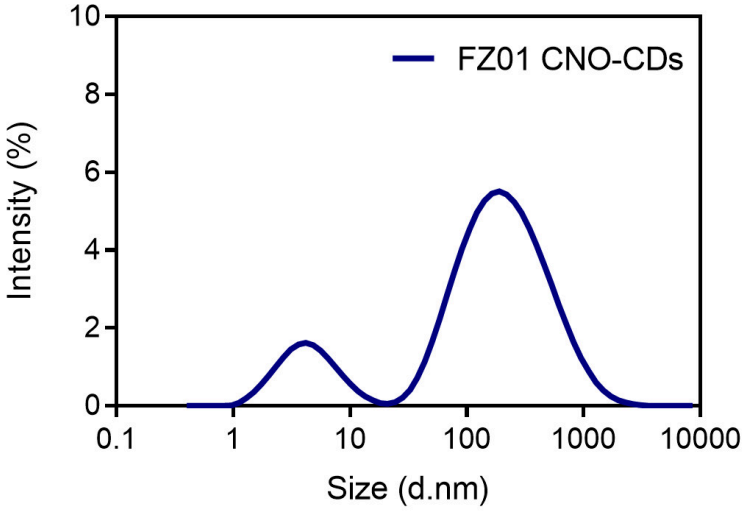

Figure 24. DLS spectrum of 1:10 diluted aqueous solution, centrifuged, sonicated, and filtered CNO-CDs.

The instrument was further used to analyse the stability of the as-synthetised CDs in aqueous solution 1:10 and the results are depicted in the Figure 25. The ζ-potential was -19.02 mV, revealing that the charges of the nanoparticles surface were negative due to the abundance of carboxyl groups derived from the oxidation method, that deprotonate in the non-buffered aqueous dispersion. The negative charge on the CDs should induce the electrostatic repulsion between the carbon dots and thus favour the stability of the dispersion.

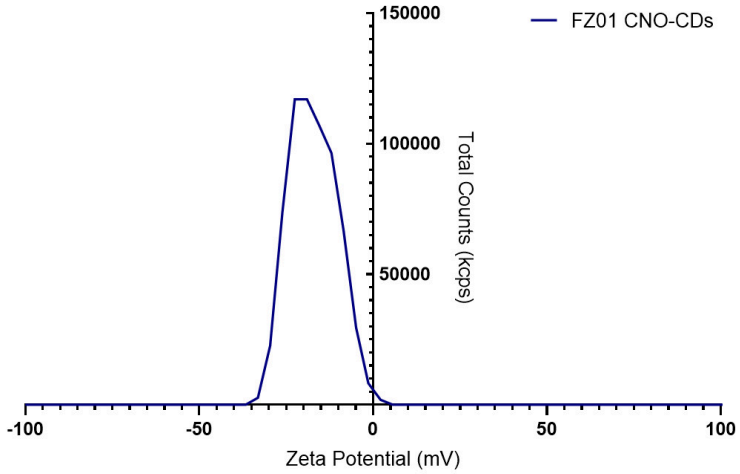

Figure 25. ζ-potential of 1:10 diluted aqueous solution, and filtered CNO-CDs.

To measure the emission properties of the sample FZ01, fluorescence spectroscopy was performed, and the results are reported in Figure 26. By exciting the specimen from 230 to 490 nm, it can be appreciated that it shows a constant fluorescence emission maximum ($\gamma_{em,max}$) centred at 527 nm at 600 a.u. of intensity, indicating fluorescence across the green region of the visible light spectrum. In addition, the results showed that the γ_{max} was independent on the excitation wavelength, but with a higher fluorescence intensity at 330 nm of excitation wavelength.

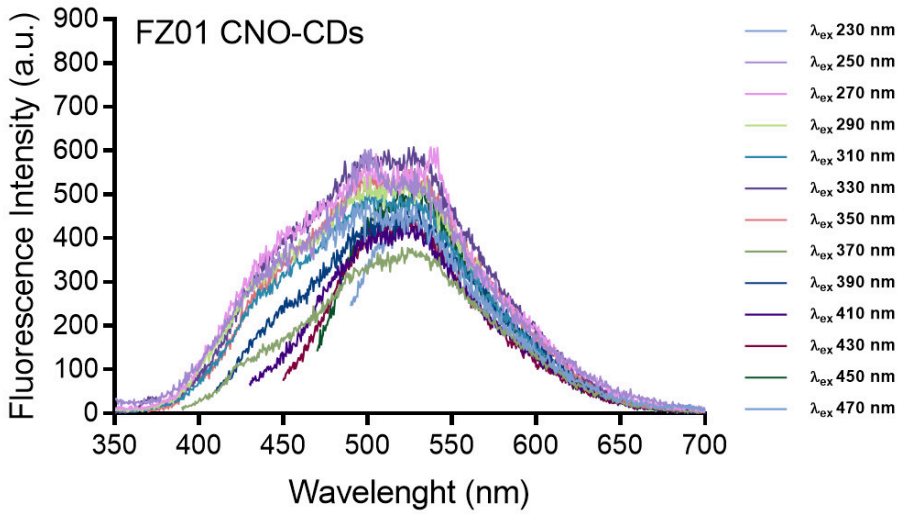

Figure 26. Fluorescence emission spectra of 1:10 diluted aqueous solution, centrifuged, sonicated, and filtered CNO-CDs.

Fluorescence excitation analyses were carried out to investigate the photoluminescent properties of the CDs. The Figure 27 depict both the excitation and emission spectra at specific excitation wavelengths. By collecting the excitation spectra, three discriminated transitions occurred at 340, 400, and 460 nm, by exciting the sample at 527 nm, with the 340 nm and 460 nm of similar intensity.

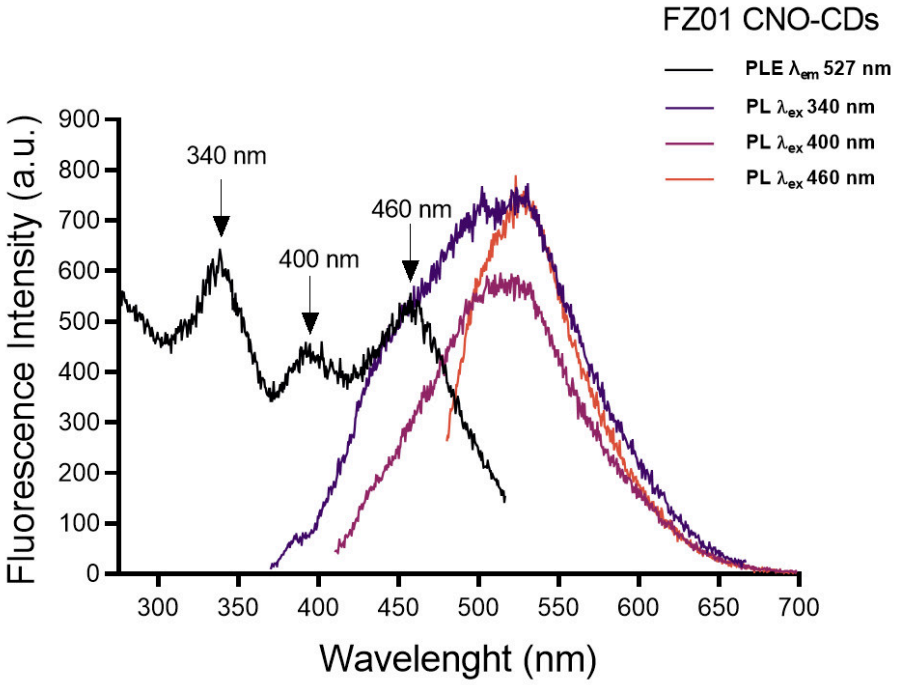

Figure 27. Fluorescence excitation spectra of 1:10 diluted aqueous solution, centrifuged, sonicated, and filtered CNO-CDs.

In Figure 28, UV-Vis spectrum of carbon dots (FZ02 sample code) exhibits strong absorbance below 400 nm, which was attribute to the overlap of n–π^* transition of carboxyl moieties (C=O) and π–π^* transitions of C=C bonds.

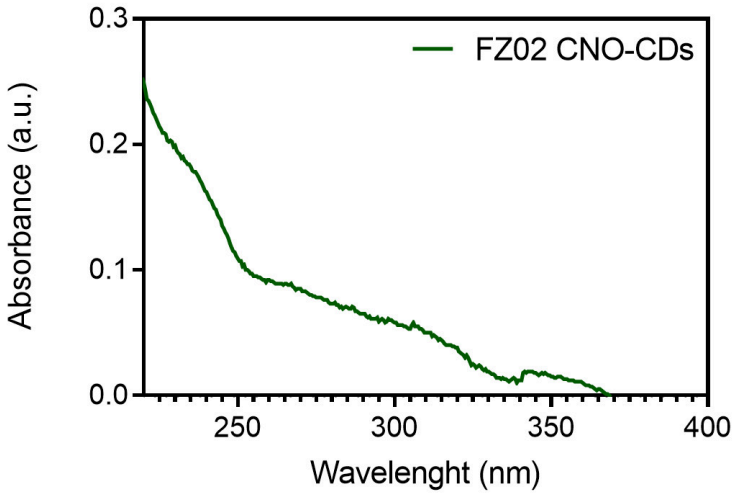

Figure 28. UV-Vis spectrum of 1:10 diluted aqueous solution of CNO-CDs.

The size distribution of CDs (sample code FZ02) was evaluated through dynamic light scattering reported in Figure 29. Once again, although it was visible the peak associated to carbon dots which gave an average size of 4 nm at 1% of Intensity, larger particles were still present and detected at a size range between 10^4 and 10^5 nm.

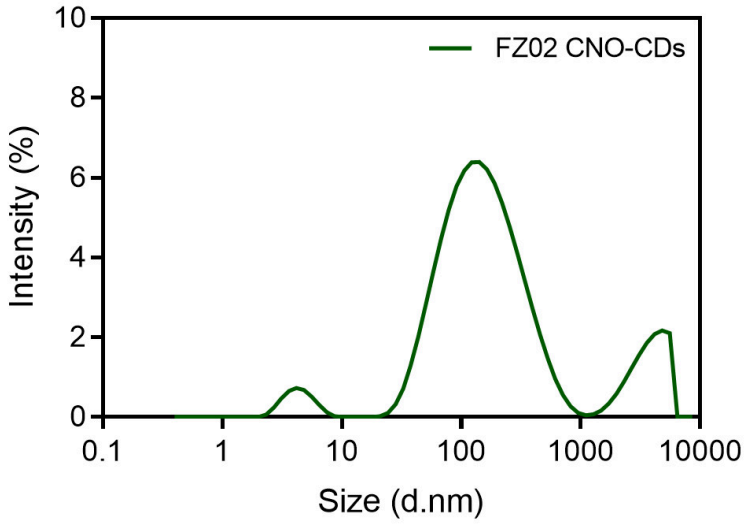

Figure 29. DLS spectrum of 1:10 diluted aqueous solution CNO-CDs.

However, based on the previously described results of carbon dots (FZ01), the sample underwent a double centrifugation at 3000, then at 2000 relative centrifugal force, 5 minutes each, sonication for 15 minutes, and filtration. The as-method revealed to be consistent and provided better results, which are shown below in Figure 30, with no visible peak at 10^4 and 10^5 nm size range.

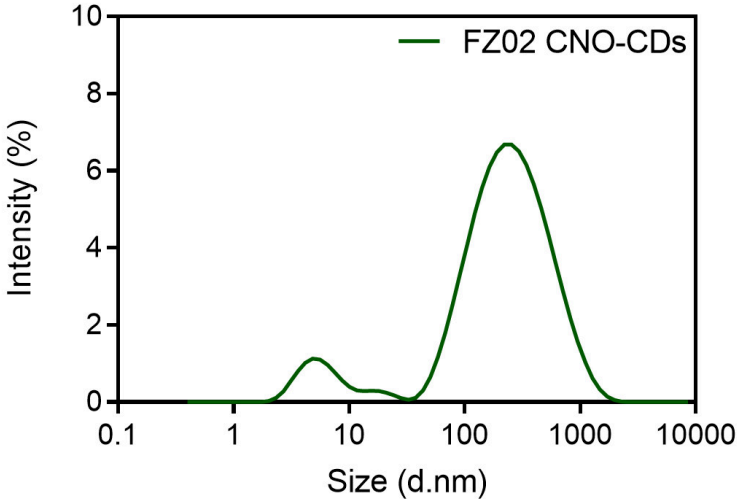

Figure 30. DLS spectrum of 1:10 diluted aqueous solution, centrifuged, sonicated, and filtered CNO-CDs.

Furthermore, ζ-potential of the carbon dots was evaluated to be -26.23 mV (Figure 31), confirming the negative surface charges of the as-synthetised nanomaterials, thus confirming their stability in aqueous solution.

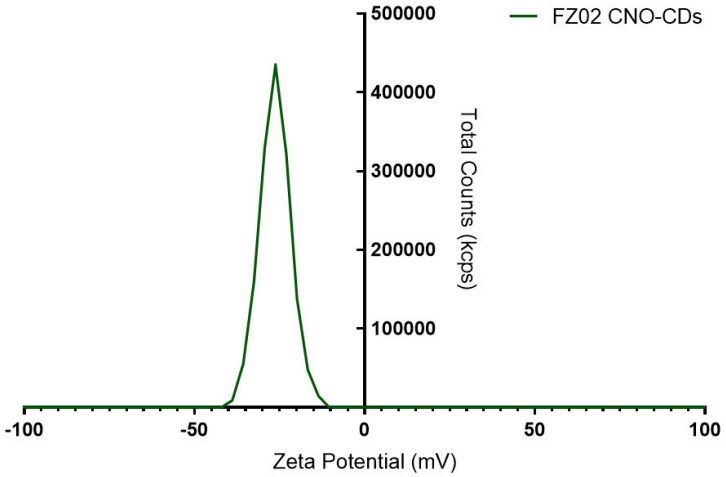

Figure 31. ζ-potential of 1:10 diluted aqueous solution, and filtered CNO-CDs.

Boron-nitrogen carbon dots (FZ03) were prepared starting from boron-nitrogen carbon nano-onions (sample code HM03) through the identic oxidative treatment protocol used for samples code name FZ01, FZ02. The conceiving idea behind the parallel synthesis of two different source-derived nanomaterials consisted of looking for a nanomaterial

characterised by a higher fluorescence property to be exploited in biological matters under imaging techniques.

BN-CDs were investigated using several techniques: UV-Vis and Fluorescence for their optical properties' determination, whereas dynamic light scattering for size distribution and zeta potential analyses. The results are following reported.

In UV-Vis spectrum of the sample (name code FZ03) shown in Figure 32, two absorption peaks at 220 nm and 340 nm are observed, the first assigned to the π–π^* transitions of C=C bonds of the aromatic domains, while the latter to the n–π^* transition of functional groups. The obtained results do confirm the findings published in literature by A. O. Chinigar *et al.* [153].

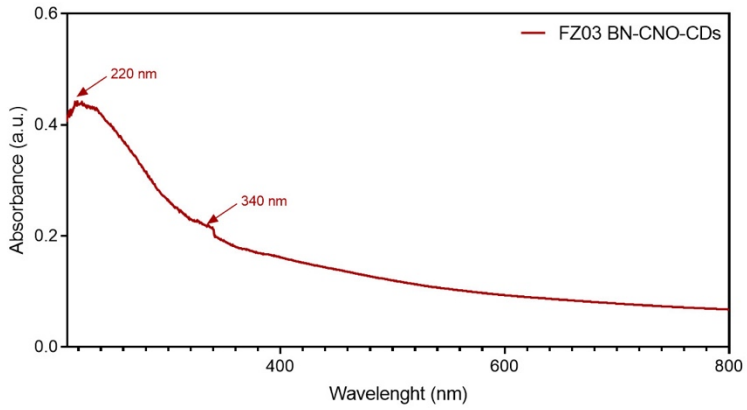

Figure 32. UV-Vis spectrum of 1:10 diluted aqueous solution of BN-CNO-CDs.

Dynamic light scattering analysis allowed the detection of the size distribution of nanoparticles, peak 1 measures 1.9 nm, while peak 2, 423.3 nm (Figure 33). The sample analysed was diluted 1:10 in aqueous solution, centrifuged at 3000, then at 2000 rcf, 5 minutes each, sonicated for 15 minutes, and filtrated as it revealed to be the best method to obtain a finer spectrum.

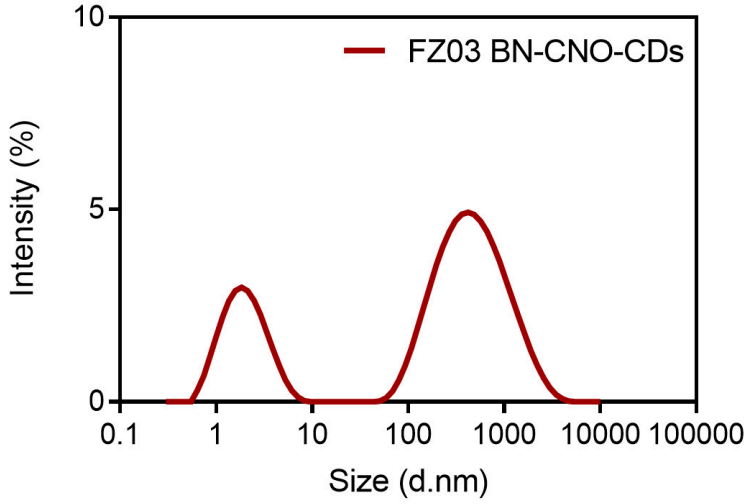

Figure 33. DLS spectrum of 1:10 diluted aqueous solution, centrifuged, sonicated, and filtered BN-CNO-CDs.

The ζ-potential of BN-CNO-CDs instead, is depicted in Figure 34. It reports a major peak at -49 mV, and a smaller shoulder peak positioned at -28 mV. The analysis demonstrated the stability of BN-CNO-CDs, in line with our previous results.

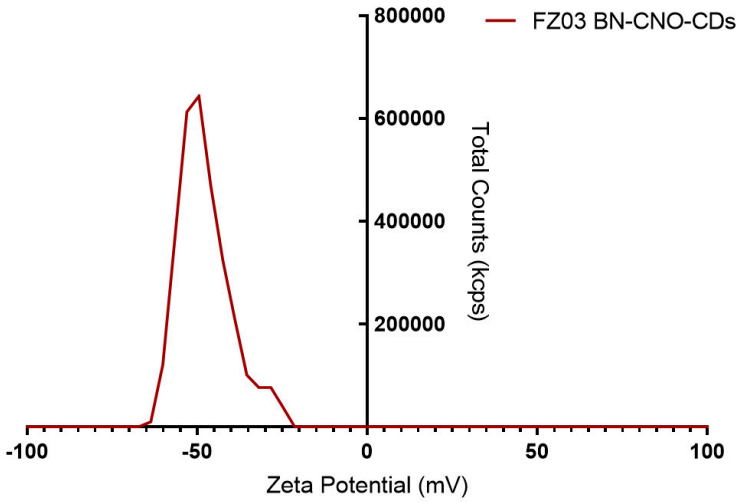

Figure 34. ζ-potential of 1:10 diluted aqueous solution, and filtered BN-CNO-CDs.

The fluorescence emission and excitation spectra of BN-CNO-CDs were acquired to further characterize the sample FZ03, with the purpose to choose the nanomaterial with the highest fluorescence properties to be utilised as label for nanoplastics synthesis. By exciting the BN-CNO-CDs from 230 to 490 nm of excitation wavelength, the fluorescence emission maximum wavelength ($\gamma_{em,max}$) resulted to fall at 527 nm at 700 a.u. of intensity, indicating fluorescence across the green region of the visible light

spectrum. Again, the γ_{max} was independent on the excitation wavelength, but with a more intense fluorescence band at 250 nm of excitation wavelength (Figure 35).

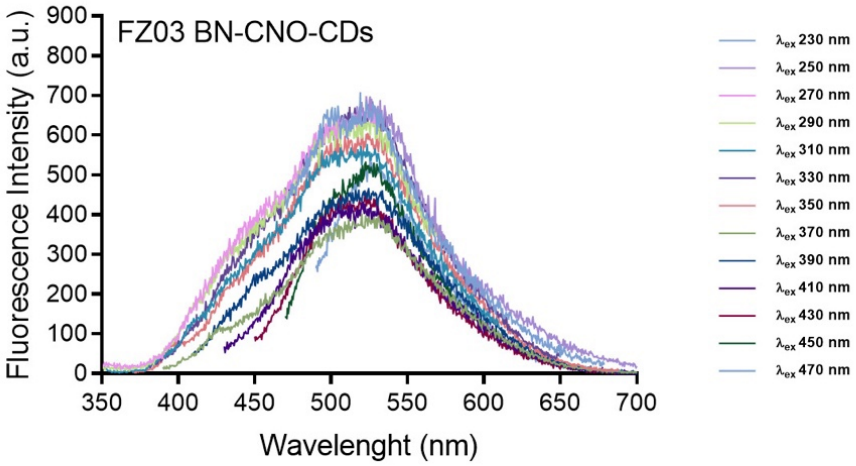

Figure 35. Fluorescence emission spectra of 1:10 diluted aqueous solution, centrifuged, sonicated, and filtered BN-CNO-CDs.

The Figure 36 shows the excitation and emission spectra at specific excitation wavelengths. By measuring the excitation spectra, three transitions were visible at 340, 400, and 460 nm, by exciting the sample at 527 nm, with the first showing higher intensity with respect to the other peaks.

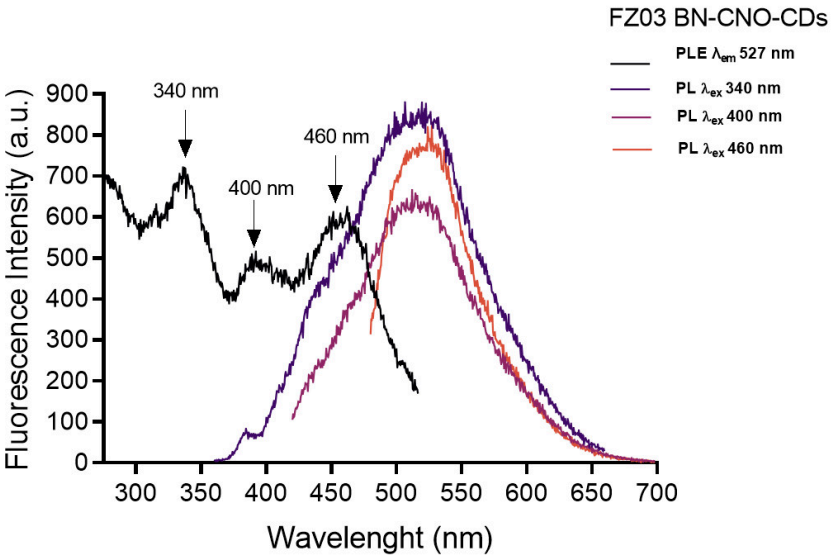

Figure 36. Fluorescence excitation spectra of 1:10 diluted aqueous solution, centrifuged, sonicated, and filtered BN-CNO-CDs.

3.4.2 Transmission Electron Microscopy

TEM was performed to confirm the size and morphology of carbon dots. Despite of the starting material (p-CNOs or p-BN-CNOs) selected for the synthesis of CDs, the TEM images revealed an average size of nanoparticles of 10 nm and a spherical morphology as visible in Figure 37. This is in line with what reported in literature [154].

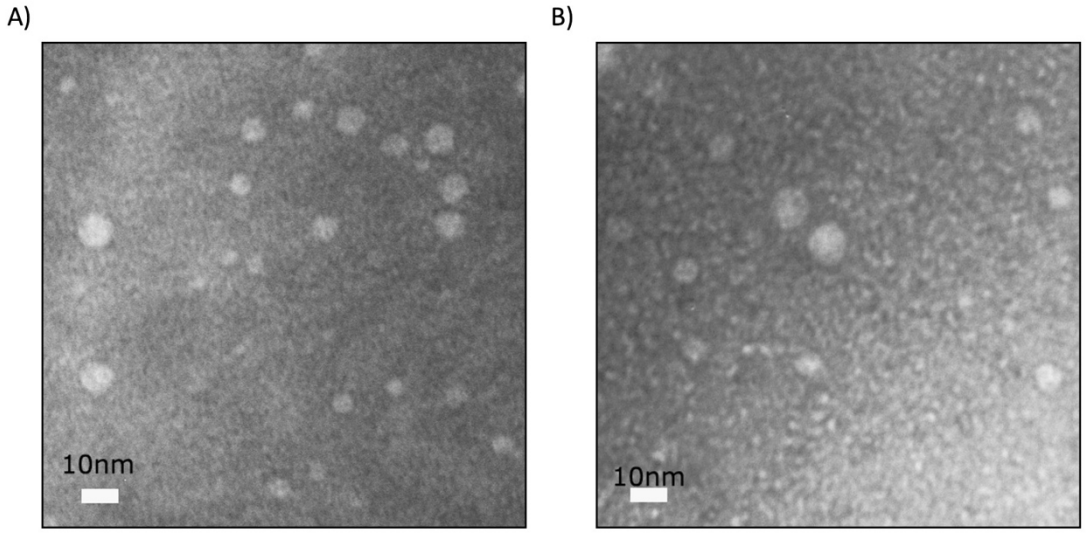

Figure 37. TEM image of CNOs-CDs A) and BN-CNOs- CDs B), with an average size of 10 nm.

TEM images acquired on polypropylene NPs and CDs labelled PP-NPs are reported in Figure 38, as representative example. It might be stated that the plastic nanoparticles are characterized by a spherical shape when measured as starting material alone (Figure 38A), whereas their morphology seems to be affected when in contact with CDs (Figure 38B). The surface appears less rounded, and it might be due either to the incorporation of the CDs in the core of the polymeric particle or to the interaction at the outer level.

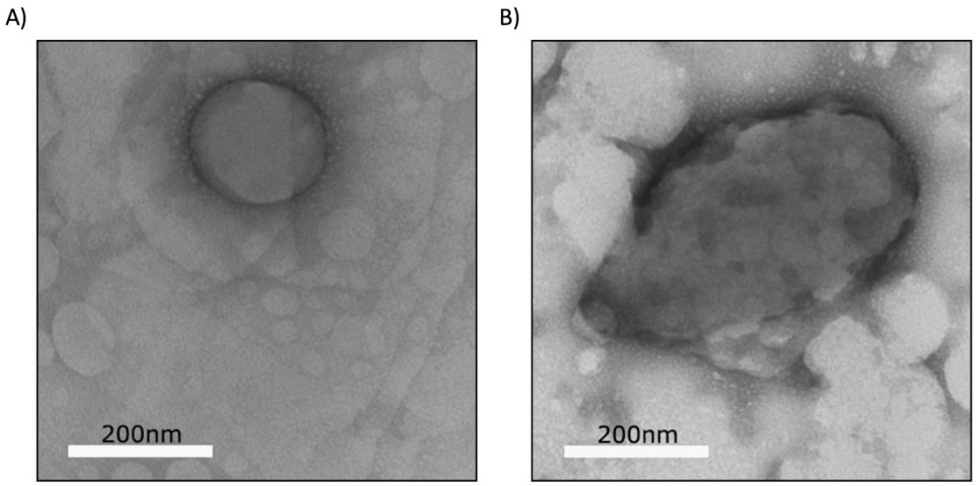

Figure 38. TEM images of polypropylene nanoplastic A), and CDs-labelled polymeric nanoplastic B).

3.4.3 Attenuated Transmission Reflectance Microspectroscopy

Carbon dots synthesised have also been characterized by FTIR ATR spectroscopy. 10 mL drop of CDs were deposited onto the diamond crystal of the ATR accessory and measured after the evaporation of the solvent. In figure 39 are shown the results for FZ01, FZ02 and FZ03.

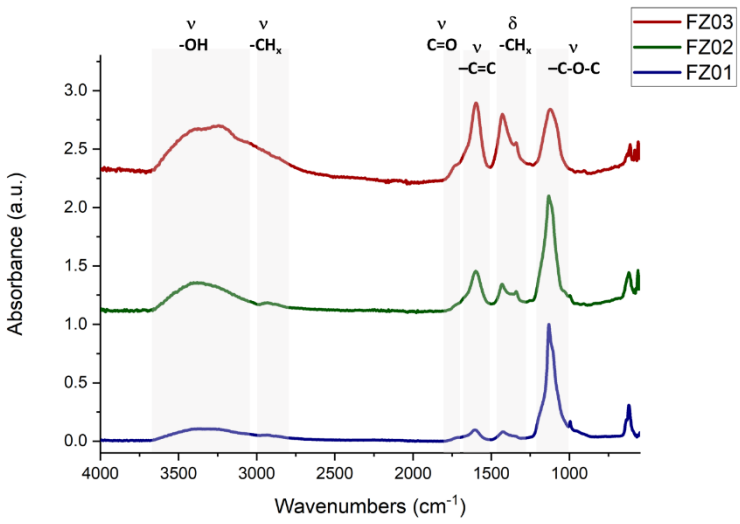

Figure 39. FTIR ATR spectra of the two CNO-CDs (FZ01 in blue, FZ02 in green) and the BN-CNO-CD (FZ03 in red). In vertical grey rectangles the spectral areas of interest, marked with the corresponding chemical moieties.

The three samples present similar spectral features, even though the ratio between the C-O-C band 1120-1130 cm^{-1} and the other bands changes. In particular, as the –OH band at increases the C-O-C band decreases, it could be related to the opening of some heterocycles and partial oxidation to hydroxyl. Between FZ01/FZ02 and FZ03 the C-O-C band redshifts 10 cm^{-1}, this can be attributed to a variation in the hydrogen bonds network. Peaks in the CH_x stretching spectral range are not strong, as expected for the spectra of CDs [155]. All three the samples present though traces of oxidation from a shoulder at 1720 cm^{-1}. The peaks at 1596 cm^{-1} and 1426 cm^{-1} can be assigned to the stretching of C=C and to the bending of the C-N, respectively. The band at 1340 cm^{-1} can be assigned to the deformations of the C-H bonds [156].

From now on, it will be reported the results of the three batches of carbon dots labelled polypropylene nanoplastics *(FZ04, FZ05, FZ06 code name), followed by the related characterization.*

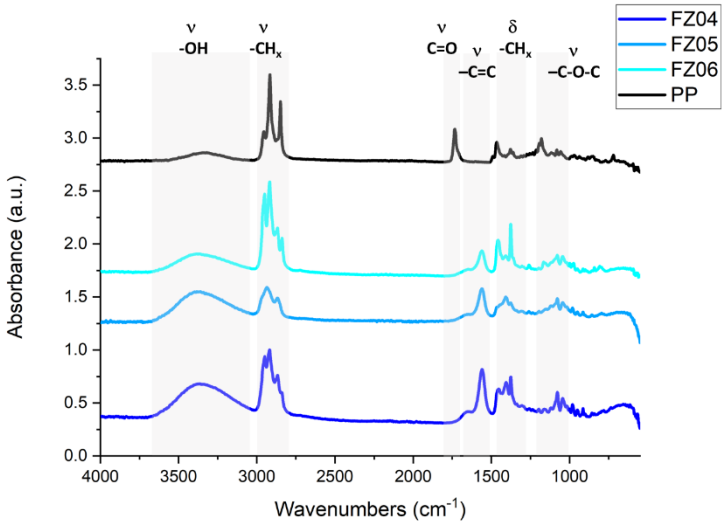

Figure 40. FTIR ATR spectra of the three CNO-CDs with NPs (FZ04 in blue, FZ05 in light blue and FZ06 in cyan) and PP NPs as a reference (PP in black). In vertical grey rectangles the spectral areas of interest, marked with the corresponding chemical moieties.

When the CDs bind to the NPs the most evident signal is the increase of the signal in the 2800 – 3000 cm^{-1} range due to the presence of the aliphatic chains of the polypropylene. In Figure 40 the three conjugates are shown below the spectrum of PP for comparison. The presented spectrum of PP is partially oxidised due, as can be seen from the presence of a strong sharp signal at 1732 cm^{-1} from the C=O and from the

decrease of the CH_3 stretching at 2955 cm^{-1}, it is plausible that the methyl moieties were oxidised to ketones or aldehydes during the solvent evaporation (toluene).

By comparing the spectra of FZ04, FZ05 and FZ06 with the one of PP, all the plastic signals are present, even though FZ04 seems to have a lower content of nanoplastics (lower signals at 2800-3000 cm^{-1} from the CH_x stretching and at 1370 cm^{-1} from the bending), instead FZ06 seems to be the one where the signals of the nanoplastic are stronger and better preserved.

In Figure 41, panel A and panel B, are shown two more detailed views of the two regions of interest, the 2800-3000 cm^{-1} A), and the fingerprint region B). A constant variation that is detectable in all the CDs labelled polypropylene nanoplastics is the shift of the band at 1600 cm^{-1} in the free CDs to 1560 cm^{-1} when attached to the NPs. Another shift regards the carbonyl band at 1720 cm^{-1} in CDs to 1670 cm^{-1} in FZ04 to FZ06. The interaction with the PP NPs causes the suppression of the strong C-O-C band centred at 1130 cm^{-1}. Even though in FZ05 the aliphatic chain of the PP is probably shortened by the reaction conditions or the purification, the particles plastic particles are linked to the CDs, since in the fingerprint region the aforementioned signals vary as happens for FZ04 and FZ06.

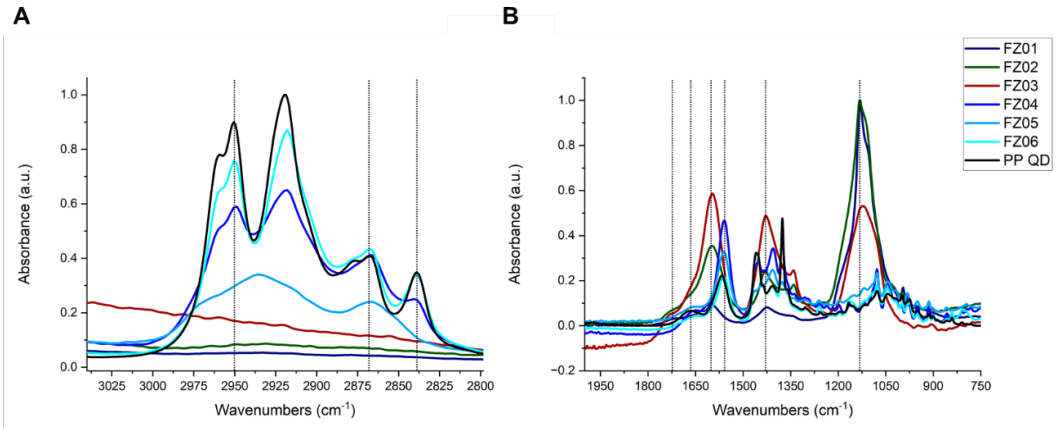

Figure 41. FTIR ATR spectra. In vertical dashed grey lines the spectral areas of interest, marked with the corresponding chemical moieties.

If the CDs signals are affected by the presence of the PP NPs, there is no evident shift in its main signals from the nanoplastic at 2950, 2870, 2840 and 1370 cm^{-1}.

3.5 Conclusions

To summarize, an alternative model of polypropylene nanoparticles was synthetized in a size range between 80-350 nm, following the chemical route published by D. Cassano *et al.* [52].

These nanoparticles were labelled with carbon dots (CDs, BN-CDs), as they both were synthetised and characterised to emit in the green range ($\gamma_{em,max}$ = 527 nm) when excited from 230 to 490 nm of excitation wavelength. The rationale behind the selection of the as-produced CDs stays in the possibility to easily detect and quantify NPs in biological specimens through advanced fluorescence micro-spectroscopies and in using a more biocompatible organic moiety for *in vitro* studies.

This work represents an excellent start point not only for the investigation of toxicological accumulation of nanoparticles across the human cells, but also for a deeper synthetic understanding of CDs fluorescence. In details, in the future it would be challenging to synthetise red emitting carbon dots labelled polypropylene nanoplastics to avoid documented eventual autofluorescence in cells [157].

CHAPTER 4 – Preliminary investigation of nano-plastics accumulation in ovarian cell line: risk for reproductive toxicity

Micro-, and nano-plastics are widely distributed in the environment, and their small size is likely to induce a toxic accumulation not only in human tissues of several organs, but they can cross cell membranes, enter cells, and behave as carriers of exogenous materials and microbes [158].

Among the multiple effects of MNPs on human health, related consequences on fertility should also be considered. About 15% of couples under reproductive age suffer from infertility in the world, which can be cause by unqualified sperm or oocyte deterioration [159]. Environmental pollutants influence both male and female reproductive function, and foetal development [160]. Therefore, based on the daily, extensive use of polymer-derived products, such as polypropylene (PP), polyvinyl chloride (PVC) MNPs, an increasing concern on human fertility is posed focusing on the recent evidence in the biological system [161]. In the female reproduction system, a pivotal role is played by the ovary, for the egg production, and the uterus for the embryo development [162].

Already several research groups are investigating the effects of micro-, nano-plastics on the reproductive system using an animal model. For instance, Wei Z. *et al.* exposed male and female C57BL/6 mice to 5.0-5.9 μm sized polystyrene microplastics (PS-MPs) for 30-44 days, demonstrating a preferred accumulation and oxidative stress in the ovary, rather than in the testis. Specifically, PS-MPs induced a decrease of both ovary size and ovary follicles. The PS-MPs exposed mice experienced a reduction in the pregnancy rate and produced less embryos, highlighting the adverse MPs impacts on reproduction and fertility [163]. The accumulation of MNPs in mice reproductive organs depends also on the nanoparticle size; Liang *et al.*, showed a higher distribution of 50, 500 nm PS-NPs in mouse testis, ovaries, and uterus, rather than larger particles of 5 μm [164].

The long-term exposure of MNPs can lead to their accumulation in mammalian reproductive organs causing apoptosis, autophagy, fibrosis, inflammation, by triggering oxidative stress and directly impairing the fertility in both sexes [165]–[169].

For a better comprehension on the harmful effects of NPs, in this study the protocol applied for THP-1 cell line (CHAPTER 2) was followed for SK-OV-3 human ovarian

cancer cell line to verify its reproducibility *in vitro* models. It represents an epithelial-like model for ovarian cells, and it has been widely used in nanomedicine and nanotoxicological studies [170].

In addition, advanced microscopy analytical techniques were carried out to investigate the distribution of labelled NPs across the ovarian cells, a preliminary case model to study the potential compromission of reproductive functions. For this purpose, part of this study was conducted at ID21 Beamline, European Synchrotron Research Facility (ESRF), Grenoble, France, in order to make advantages of the capability of the microscope to excite the label of NPs (Cadmium element), clue for its cellular localisation.

4.1 Material and Methods

4.1.1 Cell culture and sample preparation

SK-OV-3 cells is an epithelial cell line isolated from the ovary of a 64-year-old with ovarian adenocarcinoma. The cells were maintained in a sub-confluent state in complete culture medium, RPMI 1640 (Sigma-Aldrich) supplemented with 10% (v/v) foetal bovine serum (Gibco) under standard cell culture conditions (37°C, 5% CO_2 and 95% humidity). The cells were cultured in 25-cm^2 Falcon flask for 2-3 days, to be then transferred onto silicon nitride (Si_3N_4) with 100-nm-thick membranes (Silson Ltd, Warwickshire, UK) contained in 24 multi-well plates (Corning ®). To sub-culture, the cell culture medium was removed and discarded. The cell layer was washed twice with PBS 1X. Then, 1 mL of 0.25 % Trypsin \ 0.02 % EDTA solution (Gibco) was added and incubated for 1 minute to favour the cells dispersal from the flask, checked with the inverted optical microscope. After that, 5 mL of complete culture medium was added, cells were aspirated by gently pipetting and transferred to a centrifuge tube. The centrifuge was set at 1000 rotation per minute for 4 minutes. The surnatant was discarded, while the pellet was resuspended in 1 mL of complete culture medium. A 10 µL aliquot was placed into a disposable counting slide (Fast read 102 counting chambers, VWR) and cells were counted. To seed, $3 \bullet 10^4$ cells/mL were calculated for a total of 6 mL (8 wells, 350 µL each, buffers), and incubated for 24 hours. The following day, inspection with the optical microscope showed that the cells looked attached to the silicon nitride windows. Thus, apart from the control cells, i.e., untreated,

the other wells were washed with PBS twice, and incubated with the conditionate medium: 20, and 50 μg/mL of polyvinylchloride nanoplastics labelled with CdSe-QDs. After 72 hours of incubation, the medium was discarded, cells were washed twice with PBS, and 200 μL of fixative solution (4% formaldehyde prepared in PBS, Invitrogen, ThermoScientific) was added. After 20 minutes in the dark, the multi wells were washed with PBS and MilliQ, and transfer to coverslip to let them dry under the fume hood.

4.1.2 Synchrotron-based X-ray Fluorescence analysis

In order to identify the heavy elements labelling the nanoplastics (Cadmium, Cd) across the cells, and determine the distributions of other lighter elements in the sample, the cells were mapped at the ID21 beamline of the European Synchrotron Radiation Facility (ESRF), Grenoble, France. The ID21 X-ray microscope is operated in vacuum to allow the detection of light elements and minimise air absorption. An X-rays photon energy of 3.56 keV was chosen to excite the XRF K lines of S, P, Cl, and the L lines of Cd. The selected energy is just below the absorption edge of K, whose XRF K lines would otherwise overlap with Cd L lines (3.133 keV). In this way Potassium was not excited by the incoming X-ray beam and a clear Cd XRF peak could be easily identified.
A Ni reflective coating double mirrors defecting the beam in the horizontal plane ensured the harmonics rejections. To select the energy suitable for the experiment of 3.56 keV, above the Cd L absorption edge, a Si (111) double-crystal monochromator was used. The zone plate (Zone Plates Ltd, UK) focused the beam down to a microprobe of 700 nm x 300 nm (H x V) with a photon flux at 2.69 x 10^{11} photons/s. To collect the 2D fluorescent maps, the specimen was raster scanned across the micro-beam with an incident angle of 68° and output of 28°. The fluorescence photons emitted by the sample were detected by a silicon drift detector (Germany) [171]. SR-XRF data were analysed by using the freely distributed multiplatform PyMca program, developed by Sole V. *et al*. [66]

4.2 Results and Discussion

Prior XRF mapping, representative cells were selected by inspection with a visible light microscope.

The deconvolution of the collected XRF spectra was performed by using PyMCA software, producing elemental maps of P, S, Cl and Cd elements. The XRF maps are depicted with jet colorimetric scale, ranging from blue for low concentrations in the element of interest to red for the highest concentrations.

In the Panel A (Figure 42) a selected SK-OV-3 control cell is reported in both light microscope (top) and phosphorus reversed grey scale (bottom) images to highlight the morphological details. Panel B (Figure 42) shows the corresponding elemental maps: phosphorus (P) and sulphur (S) are constitutive elements of cells; thus their distribution delineates the cell shape. In particular, the P-rich zone in the central part of the cell can be attributed to the nucleus. Chloride shows a homogeneous distribution, meaning it is more concentrated in the nucleus rather than at the cellular membrane and not showing aggregates, while the counts for the cadmium XRF signal appear low, indicating a very low presence in healthy cells.

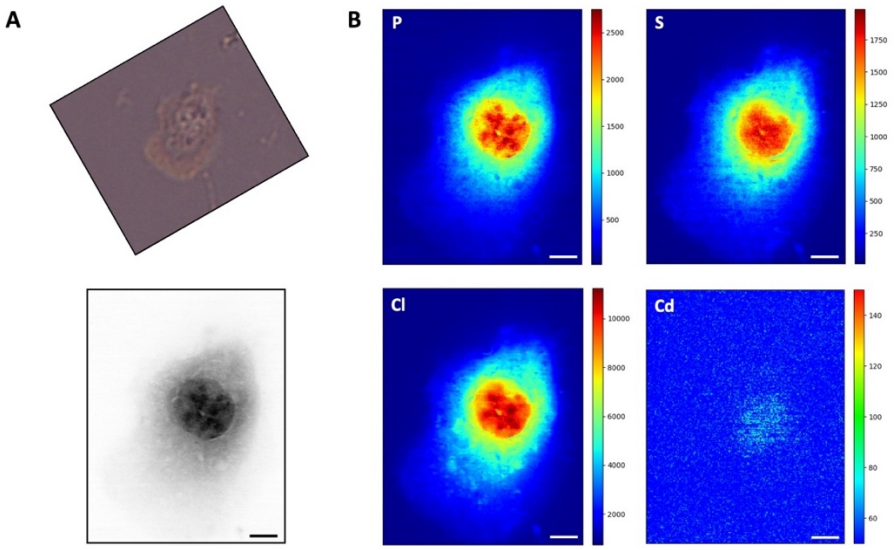

Figure 42. X-ray fluorescence analysis of untreated cells. Visible light image of the control cell on the top and the corresponding XRF phosphorus reversed grey image at the bottom A). P, S, Cl, Cd XRF maps (72 µm x 92 µm) showing the distribution of different elements. The XRF maps were acquired at 3.56 keV incident photon energy and with 400 nm spatial resolution B). Scale bar is 10 µm.

Figure 43 depicts similar panels for a SK-OV-3 cell exposed to 20 µg/mL of polyvinyl chloride nanoplastics labelled with CdSe QDs. The selected cell is shown in both light microscope (top) and phosphorus map (bottom) reversed grey scale to highlight the morphological details when exposed to nanoparticles.

Panel B in Figure 43 shows the elemental maps of the exposed cell. Chloride (Cl) map reveals chloride-rich regions, or aggregates, probably most of them at extracellular level. Cl rich zone is a hallmark of the presence of polyvinyl chloride plastic, as it contains Cl in its chemical formula. The image is represented with the colour scale that permits to appreciate the cellular Cl-aggregates, absent in the control cell (Figure 42B). Interestingly, there is a clearly co-localisation of Cl signal with the cadmium one, that is indeed from the label (CdSe QDs) linked to PVC-NPs, which are up taken into the cell.

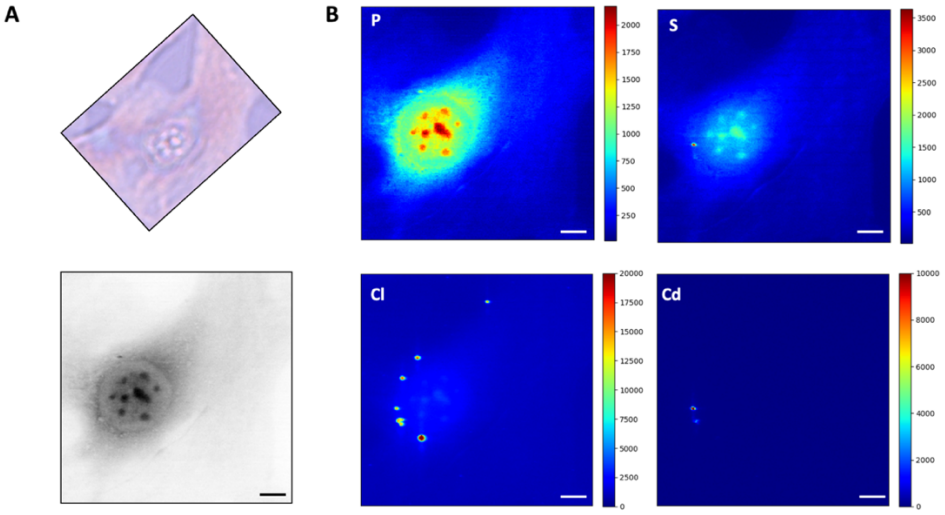

Figure 43. X-ray fluorescence analysis of treated cells with 20 µg/mL of polyvinylchloride nanoplastics labelled with CdSe QDs. Visible light image of the control cell on the top and the corresponding XRF P reversed grey scale image at the bottom A). P, S, Cl, Cd XRF maps (90 µm x 90 µm) showing the distribution of different elements. The XRF maps were acquired at 3.56 keV incident photon energy and with 400 nm spatial resolution B). Scale bar is 10 µm.

To better appreciate the co-localisation of the elements Cd and Cl, characteristic of the PVC-NPs presence in the cell, the RGB Correlator tool in PyMca software was used. Red refers to the phosphorous distribution (Panel A, Figure 44), green to chloride (Panel B, Figure 44), and blue to cadmium element (Panel C, Figure 44). The RGB image is shown in Panel D, Figure 44. The white arrows indicate the hotspots where Cd is specifically localised and it overlaps with the Cl points, appearing in violet in the panel D. This tool precisely demonstrates the cellular uptake of PVC-NPs at nanometric spatial resolution, mostly prone to be present at the plasma membrane.

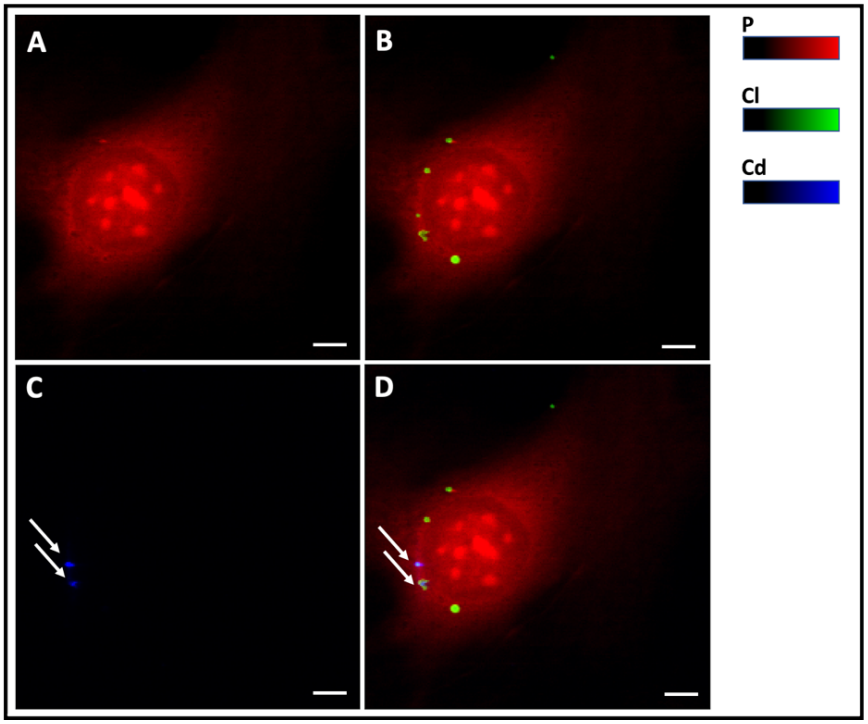

Figure 44. X-ray fluorescence analysis of treated cells with 20 µg/mL of polyvinylchloride nanoplastics labelled with CdSe QDs of Figure 43. XRF maps (90 µm x 90 µm) showing the distribution of P in red A), Cl in green B), Cd in blue C) and RGB image D). The XRF maps were acquired at 3.56 keV incident photon energy. Scale bar is 10 µm.

The measurements were repeated on several cells, to confirm the above-mentioned results. Figure 45 reports the visible light image (Panel A, top), the reversed grey image (Panel A, bottom) and the elemental maps of a group of cells exposed to 20 µg/mL of polyvinylchloride nanoplastics labelled with CdSe QDs. Also in this case, the analysis demonstrated a significant uptake of NPs, highlighted by the Cl, and Cd-rich zones in the elemental map distributions, attributable to the NPs (Cl in the polymeric chemical formula, Cd in the label placed in the NPs core).

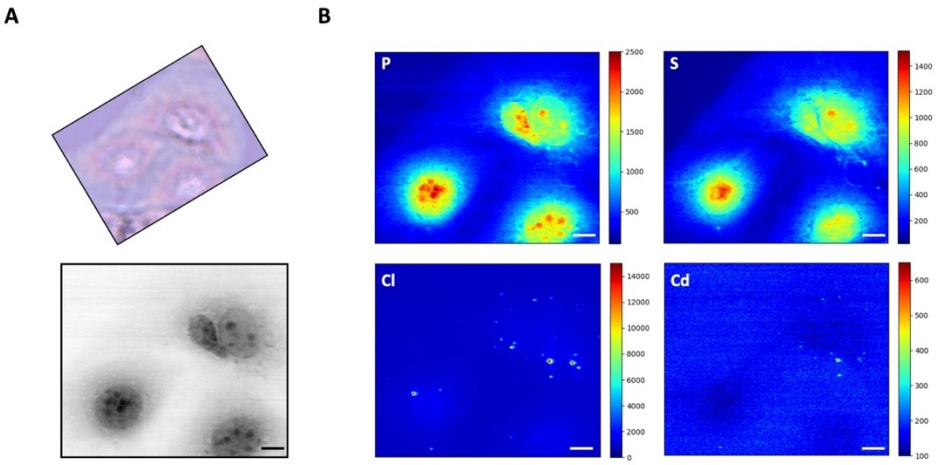

Figure 45. XRF treated cells with 20 µg/mL of polyvinylchloride nanoplastics labelled with CdSe QDs. Visible light image of the treated group of cells on the top and the corresponding XRF P reversed grey image at the bottom. A) P, S, Cl, Cd XRF maps (96 µm x 82 µm) showing the distribution of different elements. The XRF maps were acquired at 3.56 keV incident photon energy and with 400 nm spatial resolution B). Scale bar is 10 µm.

The RGB Correlator tool in PyMca software was also applied to this sample and, following the RGB legend colours, the white arrows indicate the co-presence of the elements (Cl, Cd) composing the NPs at the cellular membrane level (Figure 46).

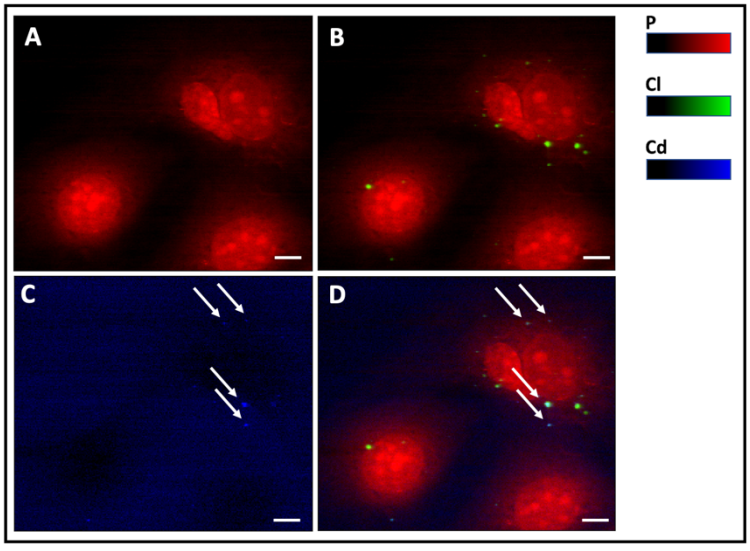

Figure 46. XRF analysis of treated cells with 20 µg/mL of polyvinylchloride nanoplastics labelled with CdSe QDs of Figure 45. XRF maps (96 µm x 82 µm) showing the distribution of P in red A), Cl in green B), Cd in blue C) and RGB image D). The XRF maps were acquired at 3.56 keV incident photon energy. Scale bar is 10 µm.

The ovarian cells were also exposed to a higher concentration of CdSe-PVC NPs, namely 50 µg/mL, to investigate a possible different cellular response to the exposure. In the Figure 47, it is possible to appreciate the presence of the NPs in the cell (see Cl and Cd XRF maps in panel B). It can be stated that, differently from what happened in 20 µg/mL CdSe-PVC NPs treated cells, nanoparticles tend to accumulate inside the cells, approaching the nuclei. The RGB co-localization shown in Figure 48 better highlights this statement.

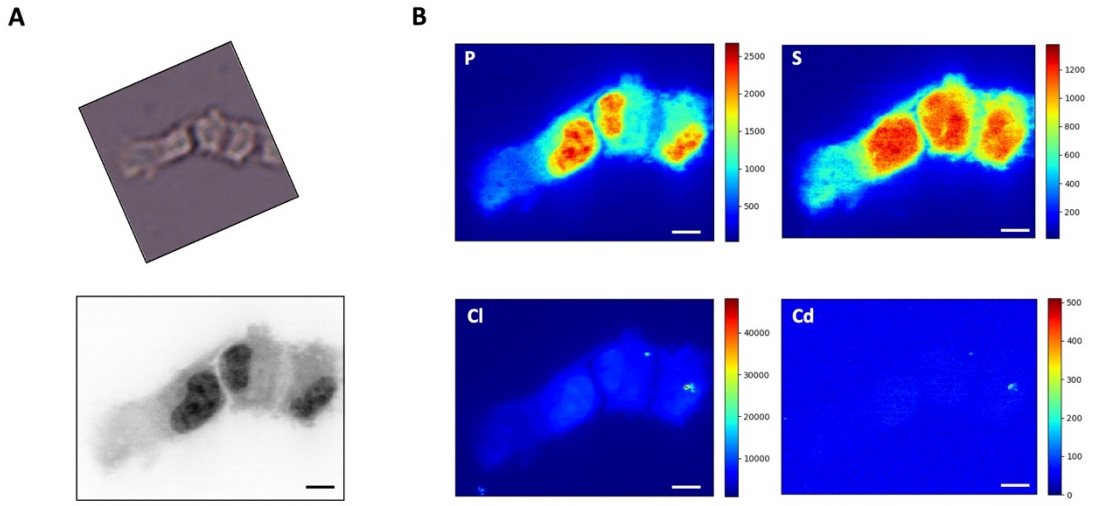

Figure 47. X-ray fluorescence analysis of treated cells with 50 µg/mL of polyvinylchloride nanoplastics labelled with CdSe QDs. Visible light image of the treated cells on the top and the corresponding XRF P reversed grey scale image at the bottom A). P, S, Cl, Cd XRF maps (92 µm x 70 µm) showing the distribution of different elements. The XRF maps were acquired at 3.56 keV incident photon energy and with 400 nm spatial resolution B). Scale bar is 10 µm.

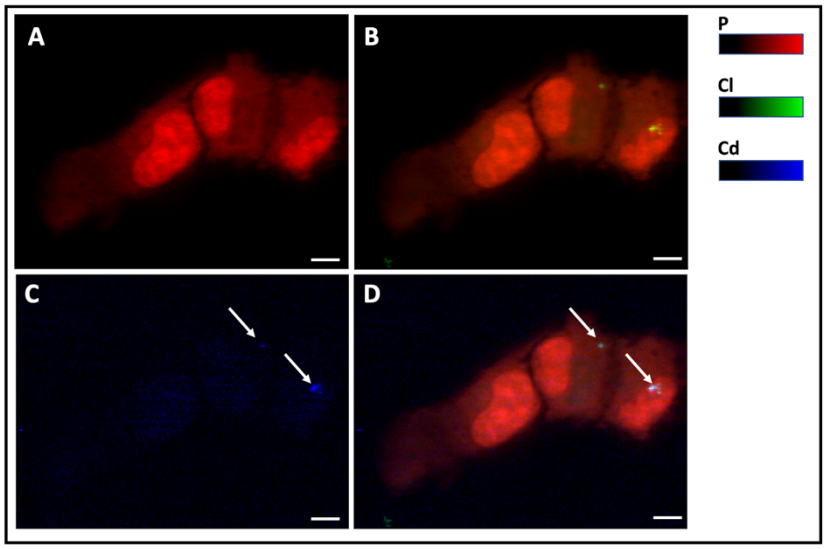

Figure 48. X-ray fluorescence analysis of treated cells with 50 µg/mL of polyvinylchloride nanoplastics labelled with CdSe QDs of Figure 47. XRF maps (92 µm x 70 µm) showing the distribution of P in red A), Cl in green B), Cd in blue C) and RGB image D). The XRF maps were acquired at 3.56 keV incident photon energy. Scale bar is 10 µm.

To increase the statistic, another group of cells exposed to 50 µg/mL CdSe-PVC NPs was measured, as reported in Figure 49, and Figure 50. In this specimen the number of distributed NPs is higher, and from the P-reversed gray scale, the cellular morphology starts to change, compared to the controls (Figure 42).

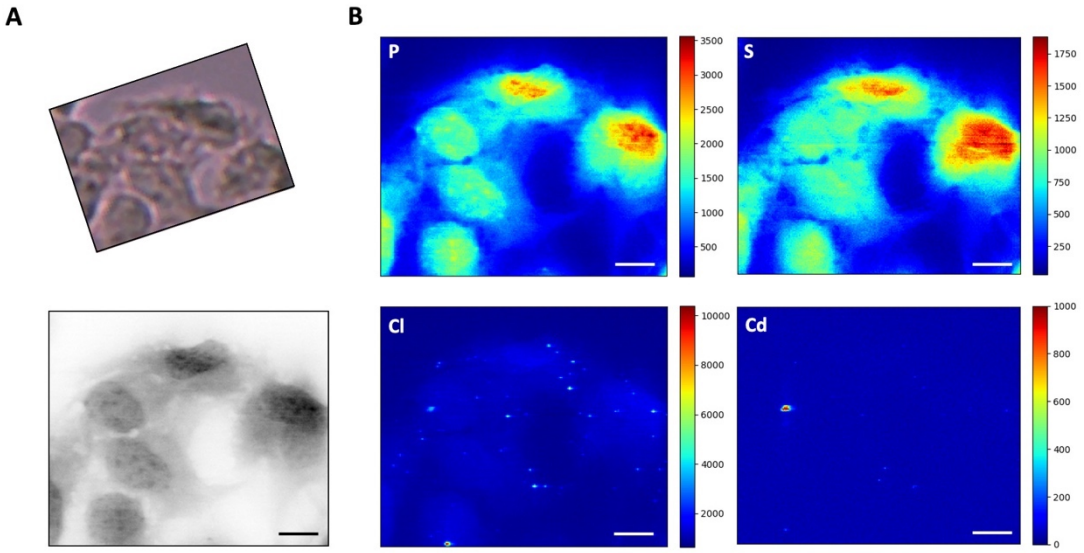

Figure 49. X-ray fluorescence analysis of treated cells with 50 µg/mL of polyvinylchloride nanoplastics labelled with CdSe QDs. Visible light image of the treated group of cells on the top and the corresponding XRF P reversed grey scale image at the bottom A). P, S, Cl, Cd XRF

maps (72 µm x 60 µm) showing the distribution of different elements. The XRF maps were acquired at 3.56 keV incident photon energy and with 300 nm spatial resolution B). Scale bar is 10 µm.

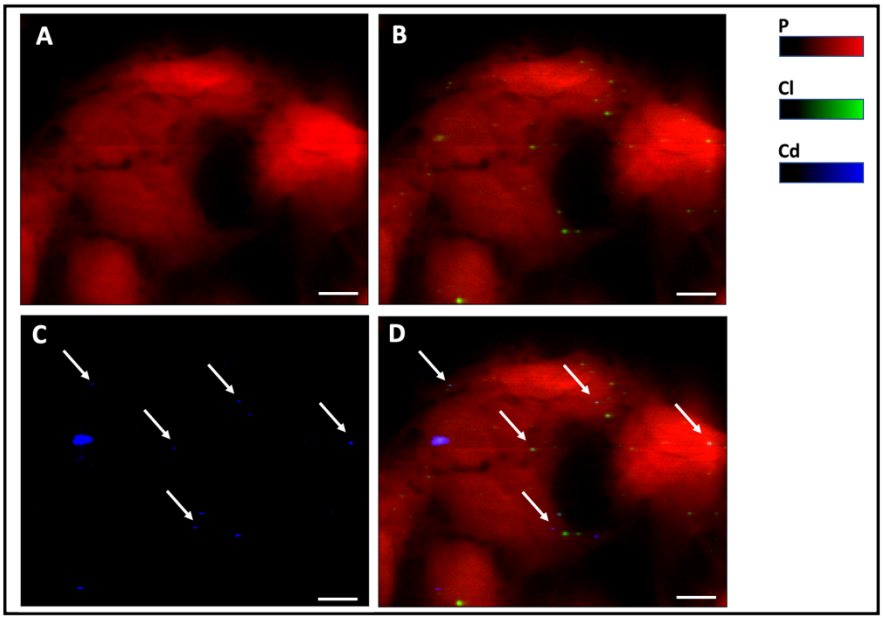

Figure 50. X-ray fluorescence analysis of treated cells with 50 µg/mL of polyvinylchloride nanoplastics labelled with CdSe QDs of Figure 49. XRF maps (72 µm x 60 µm) showing the distribution of P in red A), Cl in green B), Cd in blue C) and RGB image D). The XRF maps were acquired at 3.56 keV incident photon energy. Scale bar is 10 µm.

Although humans have been exposed to nanoparticles from an early age, the scientific concerns on their harmful effects on health has risen in the last century. Since females are particularly sensitive to nanoparticles toxicity, it may affect the reproductivity and foetal development. Therefore, it is highly demanding the studies on the cell-NPs interactions, using *in vitro* and *in vivo* models [24].

In this study the ovarian cell line (SK-OV-3) was chosen to investigate the nanoparticle toxicological accumulation, and this was inspected by X-Ray Microscopy at nanometric spatial resolution, by exciting the cadmium, element labelling the PVC-NPs at a specific excitation energy.

During the beamtime at ESRF, an average of 6-7 cells per sample conditions were analysed: untreated and treated cells with 20, and 50 µg/mL CdSe QDs-PVC NPs for 72 h of exposure time, and part of the results were reported as representative example.

XRF microscopy demonstrated to be an excellent technique to track the NPs across the ovarian cells by following the cadmium L line of one of the two elements (CdSe) linked to PVC-NPs. Despite of the NPs experimental concentration (20, 50 µg/mL), the

distribution maps revealed a co-localization of Cl, and Cd, the first referring to the nanoplastics polymer composition, the second to the CdSe-QDs, linked to the polymers. The RGB images supported the understanding of the nanoparticles' accumulation; when cells were exposed to 20 μg/mL CdSe-PVC NPs, NPs seemed to localize at the plasma membrane, whereas in the other condition, 50 μg/mL CdSe-PVC NPs, they were more likely found intracellularly.

The specificity of the Cd signal was confirmed by measuring the untreated cell, where this element was absent.

The results do confirm a possible interaction of ovarian cells with environmental nanoplastics, posing a threat in terms of reproductive toxicity. A deeper study will be further conducted to investigate the molecular mechanisms of NPs uptake and possible effects on macromolecules by Raman Spectroscopy (i.e., DNA damage).

4.3 Conclusions

Nanoplastics abundance in the environment leads to negatively affect the human body comportments due to their size-dependent cellular accessibility. The toxicity on the female reproductive system has been widely reported for aquatic animals, whereas their effects on mammalian human cell lines has not been defined yet [172].

To this aim, the present work aims at using a representative model of the female reproductive organs which have been exploited for different purposes in literature. In fact, it represents an optimal case study to investigate the potential NPs-ovarian cells interaction upon nano-pollutants exposure [173], [174].

Therefore, based on the urgent need to deal with a model of NPs which can be successfully tracked and imaged under advanced microscopy techniques to unravel the toxicological accumulation of NPs in the female body, we accurately propose an optimal strategy.

We demonstrated that NPs labelled with CdSe QDs can be followed across the ovarian cell line at nanometric spatial resolution by tuning the excitation photon energy to the suitable one for X-ray emission fluorescence Cd L line peak (one of the components of QDs). The selected energy was also able to provide the elemental distribution of phosphorus and sulphur, important for the cellular biochemical distribution and chloride and cadmium for the nanoplastics trackability. In details, the Cl XRF map distribution refers to the presence of NPs, as the element is in the chemical formula of the polymer

(PVC). In addition, the Cd map at the aggregates level, underlines the co-localisation with Cl and thus of the NPs in the cells. In fact, the Cd is contained in the core of the polymeric particle forming the fluorescent probe (CdSe QDs) needed for the imaging in biological matters. To support this evidence, Cl distribution trend in the different concentrations-treated ovarian cells was compared to the one of control cells (Figure 42B); in treated cells Cl localises in specific zones, mostly at the plasma membrane for 20 μg/mL PVC-NPs treated cells or at the intracellular level for 50 μg/mL PVC-NPs condition. In the untreated cells instead, Cd is absent. Chloride is part of the chemical formula of the polymer of PVC-NPs, whereas Cd composes the QDs, labelling the NPs. The co-localisation of Cl and Cd elements is greater evident in the corresponding RGB image shown for each figure, and it can be stated that the Cd is not as excited as Cl is, because of two important reasons: firstly, from the synthetical point of view, Cd is contained in the core of the nanoplastics in a concentration 1000 times less than the plastic polymer (Cl), therefore less concentrated element is less evident in the XRF map; secondly, from the technical point of view instead, the Cd is not well excited as the Cl is since the selected energy allows to probe Cl K lines, while for Cd only L lines, which present a much lower fluorescence yield [175].

In conclusion, the possibility to track NPs across the ovarian cell lines at nanometric spatial resolution, such as what possible at ID21 beamline, (ESRF, Grenoble, France) paves the way for further investigational studies on assessing the nanoparticles consequent impacts at the reproductive level, which will be further studied from the molecular point of view concerning the endocytosis mechanisms and toxicological endpoints.

CHAPTER 5 - GENERAL CONCLUSIONS AND FUTURE OUTLOOK

This Ph.D. work was a multidisciplinary study aimed to unravel the toxicological effect of nanomaterials in biological systems, with particular attention to investigate the harmful impacts of a new rising persistent pollutant: nanoplastics. As we have already widely discussed, the number of nano pollutants distributed in the environment is growing, and thus the human exposure risk. In the context of health safety, it is beyond important to predict the toxicological consequences. Not only adults, but also foetuses, and new-borns will need protection.

Nanoplastics are promising products in industry, but there are several concerns for human exposure routes: ingestion, skin contact, inhalation since at their size they might easily enter cells and cause related adverse effects. Our findings demonstrated that the combination of advanced synchrotron-based X-ray microscopy and fluorescence techniques (STXM and XRF) is promising to examine the toxic interaction induced by nanoplastics human exposure in the immune system (THP-1) and ovarian cell lines (SK-OV-3).

The sample preparation was not an easy task, due to a limited access to the laboratories and interaction with researchers in the first year of Ph.D, during COVID-19 pandemic.

The morphological and elemental X-ray analysis showed that in both cell models there was a NPs-cell interaction, which was confirmed by the following of the inorganic species (QDs) embedded in the polymeric core (NPs), after the exposure to nanomaterials. In both cell lines NPs tend to accumulate at the cellular level with no evidence in forming precipitates, and with a preference in the localisation at the plasma membrane or perinuclearly. Moreover, the XRF analyses were in good agreement with light fluorescence images, but at higher spatial resolution.

It was interesting to highlight that the presence of NPs induced a toxic effect in macrophages-polarised-monocytes that resulted in an impairment of lipid metabolism. The same cellular line treated with CdSe-QDs polypropylene and polyvinyl chloride NPs compared to the control showed an increase in lipid droplet contents, which was confirmed by a standard laboratory technique (lipidic staining test). This study also found that nanoplastics, at least after 72 hrs of treatment, did not significantly alter the cell viability. X-ray microscopy images (absorption and phase contrast imaging)

confirmed that the toxicity of nanomaterials was characterised by the bright vesicles' formation and, FTIR spectroscopy and imaging highlighted the lipid metabolism alterations.

We were also interested in the detection of the heavier element, Cd, which was possible to excite ad the ID21 beamline of the ESRF, Grenoble, France. The results showed a co-localisation of the linker, Cd, and the plastic polymer component, Cl, at both NPs concentration (20, 50 μg/mL) exposed ovarian cells. The present cell line was extremely informative to potentially understand the impacts of NPs in the female system, and thus a potential effect on the reproductive toxicity.

Being my Ph.D. scholarship co-financed by the Central European Research Infrastructure Consortium (CERIC), I did apply for a CERIC proposal call and got the opportunity to apply further techniques to my samples at CERIC facilities. For this purpose, I spent one month at the Laboratory for ion beam interactions at the Ruđer Bošković Institut, Zagreb, Croatia and completed the elemental characterization of the macrophagic cells analysed at TwinMic Beamline (Elettra Sincrotrone, Trieste, Italy) by using the Particle Induced X-Ray Emission technique to excite other cellular elements of interest for cell status investigation (P, Ca, K,..) reported in Appendix A.

Based on these results, we intend to broaden our scientific knowledge approaching to lipidomic and proteomic.

In addition, in the frame of the Doctor Europeus certification, I did spend part of my research activity at the Department of Chemical Sciences, Dublin City University, Dublin, Ireland. In these months, I did synthetise carbon dots starting from carbon nano-onions and boron-nitrogen carbon nano-onions and characterised them through several techniques (DLS, UV-Vis, Fluorescence). After that, CDs were labelled to polypropylene nanoplastics to produce an alternative model for *in vitro* studies, using a more biocompatible green, fluorescent probe for NPs.

Given these considerations, future studies will be intended to expand the characterisation of the as-produced model by performing and analysing data collected from TEM, and ATR FTIR. Once the NPs will be fully characterised and demonstrated to be stable, they will be used as a new model for cellular-NPs accumulation and uptake study.

Appendix A

A1. Particle Induced X-Ray Emission (PIXE) maps of PP-treated macrophages

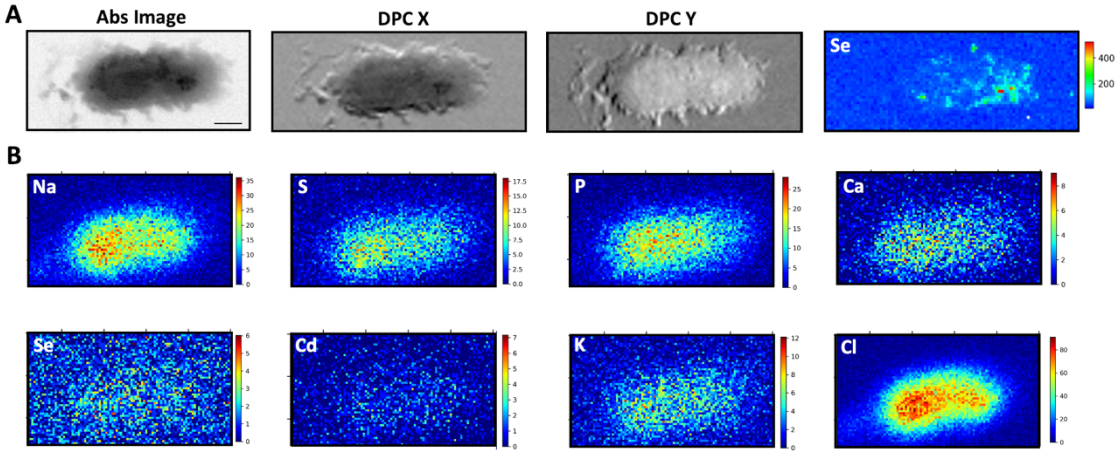

Figure A1. µXRF and PIXE microscopy of PP-NPs treated macrophage. The absorption, differential phase contrast X, and Y images were acquired at the TwinMic beamline with 1.7 keV photon energy and 450 nm spatial resolution, together with the corresponding Se (39.85 µm × 15.45 µm A), while Na, S, P, Ca, Se, Cd, K, Cl maps show the elemental distributions and were collected at 3.5 MeV H^+ at RBI, Zagreb, Croatia B). Scale bar is 5 µm.

Appendix B

B1. Raman spectra collected on nanoplastics and macrophages

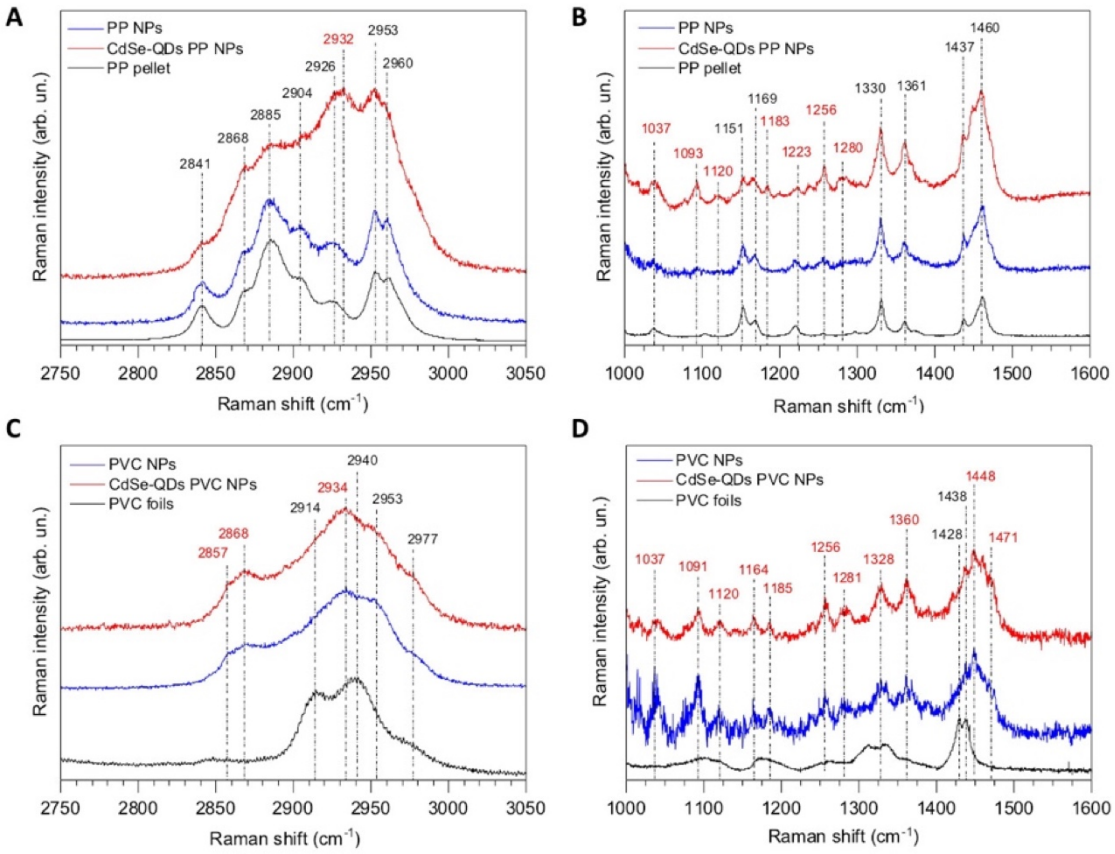

Figure B1. Panel A: Raman spectra of polypropylene-NPs (blue curve), CdSe-QDs (red curve) and polypropylene pellet (black curve) in the wavenumber range of 2750-3050 cm^{-1}. Panel B: same of Panel A in the wavenumber range of 1000-1600 cm^{-1}. Panel C: Raman spectra of polyvinyl chloride-NPs (blue curve), CdSe-QDs (red curve) and polyvinyl chloride foil (black curve) in the wavenumber range of 2750-3050 cm^{-1}. Panel D: same of Panel C in the wavenumber range of 1000-1600 cm^{-1}. All the spectra have been collected exploiting an excitation source of λ= 532 nm. Spectra are vertically shifted for a better visualization. The dotted lines highlight the vibrational bands positions.

Peak position [cm^{-1}]	Assignment	Reference
1037	PP v_{as}(C-CH_3, C-C) δ(CH)	[176]
1151	PP v_{as}(C-CH_3, C-C) δ(CH), ρ (CH_3)	[176]
1223	PP τ (CH_2), δ(CH), v_{as} (C-C)	[176]
1330	PP δ(C-H), τ (CH_2)	[176]
1361	PP δs(CH_3), δ(CH)	[176]
1460	PP δas(CH_3), δ(CH_2)	[176]
2885	PP va_s(CH_3)	[176]
2940	PVC va_s(CH_2,CH_3)	[177]
2914	PVC v_s(CH_2, CH_3)	[177]
2857	PVC v(CH_2, CH_3)	[177]
1438	PVC v_s(C-C)	[177]

v – stretching, v_s – symmetric stretching, v_{as} – asymmetric stretching, δ – bending, ρ – rocking, τ – twisting

Table B1. Peak assignations for some vibrational bands are listed.

REFERENCES

[1] *Implications of Nanotechnology for Environmental Health Research*. Washington, D.C.: National Academies Press, 2005, p. 11248. doi: 10.17226/11248.

[2] J. Hulla, S. Sahu, and A. Hayes, 'Nanotechnology: History and future', *Hum Exp Toxicol*, vol. 34, no. 12, pp. 1318–1321, Dec. 2015, doi: 10.1177/0960327115603588.

[3] K. E. Drexler, 'Engines of Creation : The Coming Era of Nanotechnology'.

[4] T. B. Bahru and E. G. Ajebe, 'A Review on Nanotechnology: Analytical Techniques Use and Applications', *IRJPAC*, pp. 1–10, Aug. 2019, doi: 10.9734/irjpac/2019/v19i430117.

[5] S. Bayda, M. Adeel, T. Tuccinardi, M. Cordani, and F. Rizzolio, 'The History of Nanoscience and Nanotechnology: From Chemical–Physical Applications to Nanomedicine', *Molecules*, vol. 25, no. 1, p. 112, Dec. 2019, doi: 10.3390/molecules25010112.

[6] N. Baig, I. Kammakakam, and W. Falath, 'Nanomaterials: a review of synthesis methods, properties, recent progress, and challenges', *Mater. Adv.*, vol. 2, no. 6, pp. 1821–1871, 2021, doi: 10.1039/D0MA00807A.

[7] S. Yadav, A. K. Sharma, and P. Kumar, 'Nanoscale Self-Assembly for Therapeutic Delivery', *Front. Bioeng. Biotechnol.*, vol. 8, p. 127, Feb. 2020, doi: 10.3389/fbioe.2020.00127.

[8] S. A. Mazari *et al.*, 'Nanomaterials: Applications, waste-handling, environmental toxicities, and future challenges – A review', *Journal of Environmental Chemical Engineering*, vol. 9, no. 2, p. 105028, Apr. 2021, doi: 10.1016/j.jece.2021.105028.

[9] Z. P. Aguilar, 'Nanotoxicology and Remediation', in *Nanomaterials for Medical Applications*, Elsevier, 2013, pp. 361–408. doi: 10.1016/B978-0-12-385089-8.00008-X.

[10] S. Sharifi, S. Behzadi, S. Laurent, M. Laird Forrest, P. Stroeve, and M. Mahmoudi, 'Toxicity of nanomaterials', *Chem. Soc. Rev.*, vol. 41, no. 6, pp. 2323–2343, 2012, doi: 10.1039/C1CS15188F.

[11] A. Brandelli, 'The interaction of nanostructured antimicrobials with biological systems: Cellular uptake, trafficking and potential toxicity', *Food Science and Human Wellness*, vol. 9, no. 1, pp. 8–20, Mar. 2020, doi: 10.1016/j.fshw.2019.12.003.

[12] N. Joudeh and D. Linke, 'Nanoparticle classification, physicochemical properties, characterization, and applications: a comprehensive review for biologists', *J Nanobiotechnol*, vol. 20, no. 1, p. 262, Jun. 2022, doi: 10.1186/s12951-022-01477-8.

[13] M. A. Gatoo, S. Naseem, M. Y. Arfat, A. Mahmood Dar, K. Qasim, and S. Zubair, 'Physicochemical Properties of Nanomaterials: Implication in Associated Toxic Manifestations', *BioMed Research International*, vol. 2014, pp. 1–8, 2014, doi: 10.1155/2014/498420.

[14] J. S. Marshall, R. Warrington, W. Watson, and H. L. Kim, 'An introduction to immunology and immunopathology', *Allergy Asthma Clin Immunol*, vol. 14, no. S2, p. 49, Sep. 2018, doi: 10.1186/s13223-018-0278-1.

[15] R. Clark and T. Kupper, 'Old Meets New: The Interaction Between Innate and Adaptive Immunity', *Journal of Investigative Dermatology*, vol. 125, no. 4, pp. 629–637, Oct. 2005, doi: 10.1111/j.0022-202X.2005.23856.x.

[16] C. Zhang, M. Yang, and A. C. Ericsson, 'Function of Macrophages in Disease: Current Understanding on Molecular Mechanisms', *Front. Immunol.*, vol. 12, p. 620510, Mar. 2021, doi: 10.3389/fimmu.2021.620510.
[17] J. Liu, Z. Liu, Y. Pang, and H. Zhou, 'The interaction between nanoparticles and immune system: application in the treatment of inflammatory diseases', *J Nanobiotechnol*, vol. 20, no. 1, p. 127, Dec. 2022, doi: 10.1186/s12951-022-01343-7.
[18] A. A. Aljabali *et al.*, 'Nanomaterials and Their Impact on the Immune System', *IJMS*, vol. 24, no. 3, p. 2008, Jan. 2023, doi: 10.3390/ijms24032008.
[19] J. H. Park and N. Oh, 'Endocytosis and exocytosis of nanoparticles in mammalian cells', *IJN*, p. 51, May 2014, doi: 10.2147/IJN.S26592.
[20] N. D. Donahue, H. Acar, and S. Wilhelm, 'Concepts of nanoparticle cellular uptake, intracellular trafficking, and kinetics in nanomedicine', *Advanced Drug Delivery Reviews*, vol. 143, pp. 68–96, Mar. 2019, doi: 10.1016/j.addr.2019.04.008.
[21] K. Habas, M. H. Brinkworth, and D. Anderson, 'Silver nanoparticle-mediated cellular responses in isolated primary Sertoli cells in vitro', *Food and Chemical Toxicology*, vol. 116, pp. 182–188, Jun. 2018, doi: 10.1016/j.fct.2018.04.030.
[22] S. Gurunathan *et al.*, 'Differential nanoreprotoxicity of silver nanoparticles in male somatic cells and spermatogonial stem cells', *IJN*, p. 1335, Feb. 2015, doi: 10.2147/IJN.S76062.
[23] L. K. Braydich-Stolle *et al.*, 'Silver Nanoparticles Disrupt GDNF/Fyn kinase Signaling in Spermatogonial Stem Cells', *Toxicological Sciences*, vol. 116, no. 2, pp. 577–589, Aug. 2010, doi: 10.1093/toxsci/kfq148.
[24] R. D. Brohi *et al.*, 'Toxicity of Nanoparticles on the Reproductive System in Animal Models: A Review', *Front. Pharmacol.*, vol. 8, p. 606, Sep. 2017, doi: 10.3389/fphar.2017.00606.
[25] 'Hou J, Wan X, Wang F, Xu G, Liu Z, Zhang T. [Effects of titanium dioxide nanoparticles on development and maturation of rat preantral follicle in vitro] [Article in Chinese]. Acad J Second Mil Med Univ. 2009;29:869–873.'.
[26] L. Preaubert *et al.*, 'Cerium dioxide nanoparticles affect *in vitro* fertilization in mice', *Nanotoxicology*, pp. 1–7, May 2015, doi: 10.3109/17435390.2015.1030792.
[27] M. Pedersen *et al.*, 'Ambient Air Pollution and Pregnancy-Induced Hypertensive Disorders: A Systematic Review and Meta-Analysis', *Hypertension*, vol. 64, no. 3, pp. 494–500, Sep. 2014, doi: 10.1161/HYPERTENSIONAHA.114.03545.
[28] K. Shirasuna *et al.*, 'Nanosilica-induced placental inflammation and pregnancy complications: Different roles of the inflammasome components NLRP3 and ASC', *Nanotoxicology*, vol. 9, no. 5, pp. 554–567, Jul. 2015, doi: 10.3109/17435390.2014.956156.
[29] B. B. Dugershaw, L. Aengenheister, S. S. K. Hansen, K. S. Hougaard, and T. Buerki-Thurnherr, 'Recent insights on indirect mechanisms in developmental toxicity of nanomaterials', *Part Fibre Toxicol*, vol. 17, no. 1, p. 31, Dec. 2020, doi: 10.1186/s12989-020-00359-x.
[30] J. Gigault *et al.*, 'Current opinion: What is a nanoplastic?', *Environmental Pollution*, vol. 235, pp. 1030–1034, Apr. 2018, doi: 10.1016/j.envpol.2018.01.024.
[31] L. Lebreton *et al.*, 'Evidence that the Great Pacific Garbage Patch is rapidly accumulating plastic', *Sci Rep*, vol. 8, no. 1, p. 4666, Mar. 2018, doi: 10.1038/s41598-018-22939-w.

[32] S. Mariano, S. Tacconi, M. Fidaleo, M. Rossi, and L. Dini, ‘Micro and Nanoplastics Identification: Classic Methods and Innovative Detection Techniques’, *Front. Toxicol.*, vol. 3, p. 636640, Feb. 2021, doi: 10.3389/ftox.2021.636640.
[33] V. Hidalgo-Ruz, L. Gutow, R. C. Thompson, and M. Thiel, ‘Microplastics in the Marine Environment: A Review of the Methods Used for Identification and Quantification’, *Environ. Sci. Technol.*, vol. 46, no. 6, pp. 3060–3075, Mar. 2012, doi: 10.1021/es2031505.
[34] M. Kedzierski *et al.*, ‘Chemical composition of microplastics floating on the surface of the Mediterranean Sea’, *Marine Pollution Bulletin*, vol. 174, p. 113284, Jan. 2022, doi: 10.1016/j.marpolbul.2021.113284.
[35] J. C. Prata, J. P. Da Costa, I. Lopes, A. C. Duarte, and T. Rocha-Santos, ‘Environmental exposure to microplastics: An overview on possible human health effects’, *Science of The Total Environment*, vol. 702, p. 134455, Feb. 2020, doi: 10.1016/j.scitotenv.2019.134455.
[36] M. B. Paul *et al.*, ‘Micro- and nanoplastics – current state of knowledge with the focus on oral uptake and toxicity’, *Nanoscale Adv.*, vol. 2, no. 10, pp. 4350–4367, 2020, doi: 10.1039/D0NA00539H.
[37] M. Al-Sid-Cheikh, S. J. Rowland, K. Stevenson, C. Rouleau, T. B. Henry, and R. C. Thompson, ‘Uptake, Whole-Body Distribution, and Depuration of Nanoplastics by the Scallop *Pecten maximus* at Environmentally Realistic Concentrations’, *Environ. Sci. Technol.*, vol. 52, no. 24, pp. 14480–14486, Dec. 2018, doi: 10.1021/acs.est.8b05266.
[38] J. J. Powell, N. Faria, E. Thomas-McKay, and L. C. Pele, ‘Origin and fate of dietary nanoparticles and microparticles in the gastrointestinal tract’, *Journal of Autoimmunity*, vol. 34, no. 3, pp. J226–J233, May 2010, doi: 10.1016/j.jaut.2009.11.006.
[39] S. L. Wright and F. J. Kelly, ‘Plastic and Human Health: A Micro Issue?’, *Environ. Sci. Technol.*, vol. 51, no. 12, pp. 6634–6647, Jun. 2017, doi: 10.1021/acs.est.7b00423.
[40] G. F. Schirinzi, I. Pérez-Pomeda, J. Sanchís, C. Rossini, M. Farré, and D. Barceló, ‘Cytotoxic effects of commonly used nanomaterials and microplastics on cerebral and epithelial human cells’, *Environmental Research*, vol. 159, pp. 579–587, Nov. 2017, doi: 10.1016/j.envres.2017.08.043.
[41] L. Wang *et al.*, ‘Environmental fate, toxicity and risk management strategies of nanoplastics in the environment: Current status and future perspectives’, *Journal of Hazardous Materials*, vol. 401, p. 123415, Jan. 2021, doi: 10.1016/j.jhazmat.2020.123415.
[42] H. Lai, X. Liu, and M. Qu, ‘Nanoplastics and Human Health: Hazard Identification and Biointerface’, *Nanomaterials*, vol. 12, no. 8, p. 1298, Apr. 2022, doi: 10.3390/nano12081298.
[43] S. Reynaud, A. Aynard, B. Grassl, and J. Gigault, ‘Nanoplastics: From model materials to colloidal fate’, *Current Opinion in Colloid & Interface Science*, vol. 57, p. 101528, Feb. 2022, doi: 10.1016/j.cocis.2021.101528.
[44] D. Magrì *et al.*, ‘Laser Ablation as a Versatile Tool To Mimic Polyethylene Terephthalate Nanoplastic Pollutants: Characterization and Toxicology Assessment’, *ACS Nano*, vol. 12, no. 8, pp. 7690–7700, Aug. 2018, doi: 10.1021/acsnano.8b01331.

[45] M. González-Pleiter *et al.*, 'Secondary nanoplastics released from a biodegradable microplastic severely impact freshwater environments', *Environ. Sci.: Nano*, vol. 6, no. 5, pp. 1382–1392, 2019, doi: 10.1039/C8EN01427B.
[46] M. Baudrimont *et al.*, 'Ecotoxicity of polyethylene nanoplastics from the North Atlantic oceanic gyre on freshwater and marine organisms (microalgae and filter-feeding bivalves)', *Environ Sci Pollut Res*, vol. 27, no. 4, pp. 3746–3755, Feb. 2020, doi: 10.1007/s11356-019-04668-3.
[47] H. El Hadri, J. Gigault, B. Maxit, B. Grassl, and S. Reynaud, 'Nanoplastic from mechanically degraded primary and secondary microplastics for environmental assessments', *NanoImpact*, vol. 17, p. 100206, Jan. 2020, doi: 10.1016/j.impact.2019.100206.
[48] P. Paik and K. K. Kar, 'High molecular weight polypropylene nanospheres: Synthesis and characterization', *J. Appl. Polym. Sci.*, vol. 105, no. 3, pp. 1133–1143, Aug. 2007, doi: 10.1002/app.26177.
[49] M. Kakugo, H. Sadatoshi, J. Sakai, and M. Yokoyama, 'Growth of polypropylene particles in heterogeneous Ziegler-Natta polymerization', *Macromolecules*, vol. 22, no. 7, pp. 3172–3177, Jul. 1989, doi: 10.1021/ma00197a046.
[50] D. M. Mitrano, A. Beltzung, S. Frehland, M. Schmiedgruber, A. Cingolani, and F. Schmidt, 'Synthesis of metal-doped nanoplastics and their utility to investigate fate and behaviour in complex environmental systems', *Nat. Nanotechnol.*, vol. 14, no. 4, pp. 362–368, Apr. 2019, doi: 10.1038/s41565-018-0360-3.
[51] F. Gagné, J. Auclair, and B. Quinn, 'Detection of polystyrene nanoplastics in biological samples based on the solvatochromic properties of Nile red: application in Hydra attenuata exposed to nanoplastics', *Environ Sci Pollut Res*, vol. 26, no. 32, pp. 33524–33531, Nov. 2019, doi: 10.1007/s11356-019-06501-3.
[52] D. Cassano, R. La Spina, J. Ponti, I. Bianchi, and D. Gilliland, 'Inorganic Species-Doped Polypropylene Nanoparticles for Multifunctional Detection', *ACS Appl. Nano Mater.*, vol. 4, no. 2, pp. 1551–1557, Feb. 2021, doi: 10.1021/acsanm.0c03039.
[53] W. Zhang, Q. Wang, and H. Chen, 'Challenges in characterization of nanoplastics in the environment', *Front. Environ. Sci. Eng.*, vol. 16, no. 1, p. 11, Jan. 2022, doi: 10.1007/s11783-021-1445-z.
[54] C. Fang, Y. Luo, and R. Naidu, 'Microplastics and nanoplastics analysis: Options, imaging, advancements and challenges', *TrAC Trends in Analytical Chemistry*, p. 117158, Jul. 2023, doi: 10.1016/j.trac.2023.117158.
[55] S. Mariano, S. Tacconi, M. Fidaleo, M. Rossi, and L. Dini, 'Micro and Nanoplastics Identification: Classic Methods and Innovative Detection Techniques', *Front. Toxicol.*, vol. 3, p. 636640, Feb. 2021, doi: 10.3389/ftox.2021.636640.
[56] L. D. B. Mandemaker and F. Meirer, 'Spectro-Microscopic Techniques for Studying Nanoplastics in the Environment and in Organisms', *Angew Chem Int Ed*, vol. 62, no. 2, Jan. 2023, doi: 10.1002/anie.202210494.
[57] H. Cai, E. G. Xu, F. Du, R. Li, J. Liu, and H. Shi, 'Analysis of environmental nanoplastics: Progress and challenges', *Chemical Engineering Journal*, vol. 410, p. 128208, Apr. 2021, doi: 10.1016/j.cej.2020.128208.
[58] V. Kumar, E. Singh, S. Singh, A. Pandey, and P. C. Bhargava, 'Micro- and nano-plastics (MNPs) as emerging pollutant in ground water: Environmental impact, potential risks, limitations and way forward towards sustainable management', *Chemical Engineering Journal*, vol. 459, p. 141568, Mar. 2023, doi: 10.1016/j.cej.2023.141568.

[59] A. Gianoncelli, G. Kourousias, L. Merolle, M. Altissimo, and A. Bianco, 'Current status of the TwinMic beamline at Elettra: a soft X-ray transmission and emission microscopy station', *J Synchrotron Rad*, vol. 23, no. 6, pp. 1526–1537, Nov. 2016, doi: 10.1107/S1600577516014405.
[60] A. Gianoncelli, G. R. Morrison, B. Kaulich, D. Bacescu, and J. Kovac, 'Scanning transmission x-ray microscopy with a configurable detector', *Appl. Phys. Lett.*, vol. 89, no. 25, p. 251117, Dec. 2006, doi: 10.1063/1.2422908.
[61] P. Marmorato *et al.*, 'Cellular distribution and degradation of cobalt ferrite nanoparticles in Balb/3T3 mouse fibroblasts', *Toxicology Letters*, vol. 207, no. 2, pp. 128–136, 2011, doi: https://doi.org/10.1016/j.toxlet.2011.08.026.
[62] A. Gianoncelli *et al.*, 'Morphological and Chemical Investigation of Ovarian Structures in a Bovine Model by Contrast-Enhanced X-ray Imaging and Microscopy', *IJMS*, vol. 24, no. 4, p. 3545, Feb. 2023, doi: 10.3390/ijms24043545.
[63] J. Schindelin *et al.*, 'Fiji: an open-source platform for biological-image analysis', *Nat Methods*, vol. 9, no. 7, pp. 676–682, Jul. 2012, doi: 10.1038/nmeth.2019.
[64] A. Gianoncelli *et al.*, 'Soft X-ray Microscopy Techniques for Medical and Biological Imaging at TwinMic—Elettra', *Applied Sciences*, vol. 11, no. 16, p. 7216, Aug. 2021, doi: 10.3390/app11167216.
[65] A. Gianoncelli, G. Kourousias, A. Stolfa, and B. Kaulich, 'Recent developments at the TwinMic beamline at ELETTRA: an 8 SDD detector setup for low energy X-ray Fluorescence', *J. Phys.: Conf. Ser.*, vol. 425, no. 18, p. 182001, Mar. 2013, doi: 10.1088/1742-6596/425/18/182001.
[66] V. A. Solé, E. Papillon, M. Cotte, Ph. Walter, and J. Susini, 'A multiplatform code for the analysis of energy-dispersive X-ray fluorescence spectra', *Spectrochimica Acta Part B: Atomic Spectroscopy*, vol. 62, no. 1, pp. 63–68, Jan. 2007, doi: 10.1016/j.sab.2006.12.002.
[67] Giovanni Birarda, Diana Bedolla, Federica Piccirilli, Chiaramaria Stani, Hendrik Vondracek, and Lisa Vaccari, 'Chemical analyses at micro and nano scale at SISSI-Bio beamline at Elettra-Sincrotrone Trieste', presented at the Proc.SPIE, Mar. 2022, p. 1195707. doi: 10.1117/12.2607751.
[68] L. Rubio, I. Barguilla, J. Domenech, R. Marcos, and A. Hernández, 'Biological effects, including oxidative stress and genotoxic damage, of polystyrene nanoparticles in different human hematopoietic cell lines', *Journal of Hazardous Materials*, vol. 398, p. 122900, Nov. 2020, doi: 10.1016/j.jhazmat.2020.122900.
[69] H. S. Lam, A. Proctor, J. Nvalala, M. D. Morris, and W. G. Smith, 'Quantitative determination of low density lipoprotein oxidation by FTIR and chemometric analysis', *Lipids*, vol. 39, no. 7, pp. 687–692, Jul. 2004, doi: 10.1007/s11745-004-1283-6.
[70] S. T. H. Sherazi, S. A. Mahesar, M. I. Bhanger, F. R. Van De Voort, and J. Sedman, 'Rapid Determination of Free Fatty Acids in Poultry Feed Lipid Extracts by SB-ATR FTIR Spectroscopy', *J. Agric. Food Chem.*, vol. 55, no. 13, pp. 4928–4932, Jun. 2007, doi: 10.1021/jf063554f.
[71] A. Oleszko *et al.*, 'Application of FTIR-ATR Spectroscopy to Determine the Extent of Lipid Peroxidation in Plasma during Haemodialysis', *BioMed Research International*, vol. 2015, pp. 1–8, 2015, doi: 10.1155/2015/245607.
[72] K. Kochan, H. Peng, B. R. Wood, and V. S. Haritos, 'Single cell assessment of yeast metabolic engineering for enhanced lipid production using Raman and AFM-IR imaging', *Biotechnol Biofuels*, vol. 11, no. 1, p. 106, Dec. 2018, doi: 10.1186/s13068-018-1108-x.

[73] G. Barraza-Garza *et al.*, 'Infrared Spectroscopy as a Tool to Study the Antioxidant Activity of Polyphenolic Compounds in Isolated Rat Enterocytes', *Oxidative Medicine and Cellular Longevity*, vol. 2016, pp. 1–10, 2016, doi: 10.1155/2016/9245150.
[74] A. Pielesz, D. Biniaś, W. Waksmańska, and R. Bobiński, 'Lipid bands of approx. 1740 cm−1 as spectral biomarkers and image of tissue oxidative stress', *Spectrochimica Acta Part A: Molecular and Biomolecular Spectroscopy*, vol. 286, p. 121926, Feb. 2023, doi: 10.1016/j.saa.2022.121926.
[75] 'M.P. McDonald, I.M. Ward, The assignment of the infra-red absorption bands and the measurement of tacticity in polypropylene, Polymer, Volume 2, 1961, Pages 341-355, ISSN 0032-3861, https://doi.org/10.1016/0032-3861(61)90037-4.'.
[76] 'Jian Fang, Li Zhang, David Sutton, Xungai Wang, and Tong Lin. 2012. Needleless melt-electrospinning of polypropylene nanofibres. J. Nanomaterials 2012, Article 16 (January 2012), 9 pages. https://doi.org/10.1155/2012/382639'.
[77] 'Krimm, S. and Liang, C.Y. (1956), Infrared spectra of high polymers. IV. Polyvinyl chloride, polyvinylidene chloride, and copolymers. J. Polym. Sci., 22: 95-112. https://doi.org/10.1002/pol.1956.1202210012'.
[78] 'Mantsch HH, Chapman D. Infrared spectroscopy of biomolecules. New York: Wiley-Liss, Inc (1996). p. 279.'.
[79] 'Mantsch HH, McElhaney RN. Phospholipid phase transitions in model and biological membranes as studied by infrared spectroscopy. Chem Phys Lipids (1991) 57:213–226. doi: Doi: 10.1016/0009-3084(91)90077-o'.
[80] S. Rak, T. De Zan, J. Stefulj, M. Kosović, O. Gamulin, and M. Osmak, 'FTIR spectroscopy reveals lipid droplets in drug resistant laryngeal carcinoma cells through detection of increased ester vibrational bands intensity', *Analyst*, vol. 139, no. 13, pp. 3407–3415, 2014, doi: 10.1039/C4AN00412D.
[81] M. Jackson and H. H. Mantsch, 'Protein secondary structure from FT-IR spectroscopy: correlation with dihedral angles from three-dimensional Ramachandran plots', *Can. J. Chem.*, vol. 69, no. 11, pp. 1639–1642, Nov. 1991, doi: 10.1139/v91-240.
[82] A. Barth, 'Infrared spectroscopy of proteins', *Biochimica et Biophysica Acta (BBA) - Bioenergetics*, vol. 1767, no. 9, pp. 1073–1101, Sep. 2007, doi: 10.1016/j.bbabio.2007.06.004.
[83] C. Stani, L. Vaccari, E. Mitri, and G. Birarda, 'FTIR investigation of the secondary structure of type I collagen: New insight into the amide III band', *Spectrochimica Acta Part A: Molecular and Biomolecular Spectroscopy*, vol. 229, p. 118006, Mar. 2020, doi: 10.1016/j.saa.2019.118006.
[84] P. Zucchiatti *et al.*, 'Contribution of Ribonucleic Acid (RNA) to the Fourier Transform Infrared (FTIR) Spectrum of Eukaryotic Cells', *Anal. Chem.*, vol. 88, no. 24, pp. 12090–12098, Dec. 2016, doi: 10.1021/acs.analchem.6b02744.
[85] D. R. Whelan, K. R. Bambery, D. McNaughton, L. Puskar, and B. R. Wood, 'Monitoring the Conformation and Concentration of DNA in Live Cells using Fourier Transform Infrared Spectroscopy', *Biophysical Journal*, vol. 106, no. 2, p. 206a, Jan. 2014, doi: 10.1016/j.bpj.2013.11.1210.
[86] L. Pascolo *et al.*, 'Differential protein folding and chemical changes in lung tissues exposed to asbestos or particulates', *Sci Rep*, vol. 5, no. 1, p. 12129, Jul. 2015, doi: 10.1038/srep12129.
[87] H. A. Leslie, M. J. M. Van Velzen, S. H. Brandsma, A. D. Vethaak, J. J. Garcia-Vallejo, and M. H. Lamoree, 'Discovery and quantification of plastic particle

pollution in human blood', *Environment International*, vol. 163, p. 107199, May 2022, doi: 10.1016/j.envint.2022.107199.
[88] J. Qiao *et al.*, 'Perturbation of gut microbiota plays an important role in micro/nanoplastics-induced gut barrier dysfunction', *Nanoscale*, vol. 13, no. 19, pp. 8806–8816, 2021, doi: 10.1039/D1NR00038A.
[89] M. Busch, G. Bredeck, A. A. M. Kämpfer, and R. P. F. Schins, 'Investigations of acute effects of polystyrene and polyvinyl chloride micro- and nanoplastics in an advanced in vitro triple culture model of the healthy and inflamed intestine', *Environmental Research*, vol. 193, p. 110536, Feb. 2021, doi: 10.1016/j.envres.2020.110536.
[90] J. Deng *et al.*, 'Microplastics released from food containers can suppress lysosomal activity in mouse macrophages', *Journal of Hazardous Materials*, vol. 435, p. 128980, Aug. 2022, doi: 10.1016/j.jhazmat.2022.128980.
[91] M. Xu *et al.*, 'Internalization and toxicity: A preliminary study of effects of nanoplastic particles on human lung epithelial cell', *Science of The Total Environment*, vol. 694, p. 133794, Dec. 2019, doi: 10.1016/j.scitotenv.2019.133794.
[92] M. Hesler *et al.*, 'Multi-endpoint toxicological assessment of polystyrene nano- and microparticles in different biological models in vitro', *Toxicology in Vitro*, vol. 61, p. 104610, Dec. 2019, doi: 10.1016/j.tiv.2019.104610.
[93] M. Busch *et al.*, 'Assessing the NLRP3 Inflammasome Activating Potential of a Large Panel of Micro- and Nanoplastics in THP-1 Cells', *Biomolecules*, vol. 12, no. 8, p. 1095, Aug. 2022, doi: 10.3390/biom12081095.
[94] A. Tavakolpournegari *et al.*, 'Hazard assessment of different-sized polystyrene nanoplastics in hematopoietic human cell lines', *Chemosphere*, vol. 325, p. 138360, Jun. 2023, doi: 10.1016/j.chemosphere.2023.138360.
[95] L. Zupin *et al.*, 'Upside-Down Preference in the Forskolin-Induced In Vitro Differentiation of 50B11 Sensory Neurons: A Morphological Investigation by Label-Free Non-Linear Microscopy', *IJMS*, vol. 24, no. 9, p. 8354, May 2023, doi: 10.3390/ijms24098354.
[96] I. Florance, S. Ramasubbu, A. Mukherjee, and N. Chandrasekaran, 'Polystyrene nanoplastics dysregulate lipid metabolism in murine macrophages in vitro', *Toxicology*, vol. 458, p. 152850, Jun. 2021, doi: 10.1016/j.tox.2021.152850.
[97] M. K. Alam *et al.*, 'Spectroscopic evaluation of living murine macrophage cells before and after activation using attenuated total reflectance infrared spectroscopy', *Vibrational Spectroscopy*, vol. 34, no. 1, pp. 3–11, Jan. 2004, doi: 10.1016/j.vibspec.2003.07.002.
[98] G. Birarda, D. E. Bedolla, E. Mitri, S. Pacor, G. Grenci, and L. Vaccari, 'Apoptotic pathways of U937 leukemic monocytes investigated by infrared microspectroscopy and flow cytometry', *Analyst*, vol. 139, no. 12, pp. 3097–3106, 2014, doi: 10.1039/C4AN00317A.
[99] D. Ortiz, M. Munoz, J. Nieto-Sandoval, C. Romera-Castillo, Z. M. De Pedro, and J. A. Casas, 'Insights into the degradation of microplastics by Fenton oxidation: From surface modification to mineralization', *Chemosphere*, vol. 309, p. 136809, Dec. 2022, doi: 10.1016/j.chemosphere.2022.136809.
[100] 'Pignatello JJ, Oliveros E, MacKay A. Advanced Oxidation Processes for Organic Contaminant Destruction Based on the Fenton Reaction and Related Chemistry. Critical Reviews in Environmental Science and Technology (2006) 36:1–84. doi: 10.1080/10643380500326564.'.

[101] R. J. Tidy, V. Lam, N. Fimognari, J. C. Mamo, and M. J. Hackett, 'FTIR studies of the similarities between pathology induced protein aggregation in vivo and chemically induced protein aggregation ex vivo', *Vibrational Spectroscopy*, vol. 91, pp. 68–76, Jul. 2017, doi: 10.1016/j.vibspec.2016.09.016.
[102] A. Ventrella, A. Camisasca, A. Fontana, and S. Giordani, 'Synthesis of green fluorescent carbon dots from carbon nano-onions and graphene oxide', *RSC Adv.*, vol. 10, no. 60, pp. 36404–36412, 2020, doi: 10.1039/D0RA06172G.
[103] F. Zingaro *et al.*, 'Morphological and lipid metabolism alterations in macrophages exposed to model environmental nanoplastics traced by high-resolution synchrotron techniques', *Front. Immunol.*, vol. 14, p. 1247747, Sep. 2023, doi: 10.3389/fimmu.2023.1247747.
[104] P. Zhu *et al.*, 'Carbon Dots in Biomedicine: A Review', *ACS Appl. Bio Mater.*, vol. 5, no. 5, pp. 2031–2045, May 2022, doi: 10.1021/acsabm.1c01215.
[105] R. M. S. Sendão, J. C. G. Esteves Da Silva, and L. Pinto Da Silva, 'Applications of Fluorescent Carbon Dots as Photocatalysts: A Review', *Catalysts*, vol. 13, no. 1, p. 179, Jan. 2023, doi: 10.3390/catal13010179.
[106] X. Sun and Y. Lei, 'Fluorescent carbon dots and their sensing applications', *TrAC Trends in Analytical Chemistry*, vol. 89, pp. 163–180, Apr. 2017, doi: 10.1016/j.trac.2017.02.001.
[107] E. A. Stepanidenko, E. V. Ushakova, A. V. Fedorov, and A. L. Rogach, 'Applications of Carbon Dots in Optoelectronics', *Nanomaterials*, vol. 11, no. 2, p. 364, Feb. 2021, doi: 10.3390/nano11020364.
[108] A. M. M. Hasan, Md. A. Hasan, A. Reza, Md. M. Islam, and Md. A. B. H. Susan, 'Carbon dots as nano-modules for energy conversion and storage', *Materials Today Communications*, vol. 29, p. 102732, Dec. 2021, doi: 10.1016/j.mtcomm.2021.102732.
[109] H. Li, Z. Kang, Y. Liu, and S.-T. Lee, 'Carbon nanodots: synthesis, properties and applications', *J. Mater. Chem.*, vol. 22, no. 46, p. 24230, 2012, doi: 10.1039/c2jm34690g.
[110] K. Ghosal and A. Ghosh, 'Carbon dots: The next generation platform for biomedical applications', *Materials Science and Engineering: C*, vol. 96, pp. 887–903, Mar. 2019, doi: 10.1016/j.msec.2018.11.060.
[111] P. G. Luo *et al.*, 'Carbon "quantum" dots for optical bioimaging', *J. Mater. Chem. B*, vol. 1, no. 16, p. 2116, 2013, doi: 10.1039/c3tb00018d.
[112] X. Xu *et al.*, 'Electrophoretic Analysis and Purification of Fluorescent Single-Walled Carbon Nanotube Fragments', *J. Am. Chem. Soc.*, vol. 126, no. 40, pp. 12736–12737, Oct. 2004, doi: 10.1021/ja040082h.
[113] Y.-P. Sun *et al.*, 'Quantum-Sized Carbon Dots for Bright and Colorful Photoluminescence', *J. Am. Chem. Soc.*, vol. 128, no. 24, pp. 7756–7757, Jun. 2006, doi: 10.1021/ja062677d.
[114] S. Zhu, Y. Song, X. Zhao, J. Shao, J. Zhang, and B. Yang, 'The photoluminescence mechanism in carbon dots (graphene quantum dots, carbon nanodots, and polymer dots): current state and future perspective', *Nano Res.*, vol. 8, no. 2, pp. 355–381, Feb. 2015, doi: 10.1007/s12274-014-0644-3.
[115] N. Vasimalai *et al.*, 'Green synthesis of fluorescent carbon dots from spices for in vitro imaging and tumour cell growth inhibition', *Beilstein J. Nanotechnol.*, vol. 9, pp. 530–544, Feb. 2018, doi: 10.3762/bjnano.9.51.
[116] S. Zhu *et al.*, 'Surface Chemistry Routes to Modulate the Photoluminescence of Graphene Quantum Dots: From Fluorescence Mechanism to Up-Conversion

Bioimaging Applications', *Adv. Funct. Mater.*, vol. 22, no. 22, pp. 4732–4740, Nov. 2012, doi: 10.1002/adfm.201201499.
[117] L. Li and T. Dong, 'Photoluminescence tuning in carbon dots: surface passivation or/and functionalization, heteroatom doping', *J. Mater. Chem. C*, vol. 6, no. 30, pp. 7944–7970, 2018, doi: 10.1039/C7TC05878K.
[118] A. Sciortino *et al.*, 'The interaction of photoexcited carbon nanodots with metal ions disclosed down to the femtosecond scale', *Nanoscale*, vol. 9, no. 33, pp. 11902–11911, 2017, doi: 10.1039/C7NR03754F.
[119] K. Holá *et al.*, 'Graphitic Nitrogen Triggers Red Fluorescence in Carbon Dots', *ACS Nano*, vol. 11, no. 12, pp. 12402–12410, Dec. 2017, doi: 10.1021/acsnano.7b06399.
[120] Y. Ding *et al.*, 'Synthesis of short-chain passivated carbon quantum dots as the light emitting layer towards electroluminescence', *RSC Adv.*, vol. 7, no. 46, pp. 28754–28762, 2017, doi: 10.1039/C7RA02421E.
[121] M. Alafeef, I. Srivastava, T. Aditya, and D. Pan, 'Carbon Dots: From Synthesis to Unraveling the Fluorescence Mechanism', *Small*, p. 2303937, Sep. 2023, doi: 10.1002/smll.202303937.
[122] K. Jiang *et al.*, 'Red, Green, and Blue Luminescence by Carbon Dots: Full-Color Emission Tuning and Multicolor Cellular Imaging', *Angew. Chem. Int. Ed.*, vol. 54, no. 18, pp. 5360–5363, Apr. 2015, doi: 10.1002/anie.201501193.
[123] L. Bao, C. Liu, Z. Zhang, and D. Pang, 'Photoluminescence-Tunable Carbon Nanodots: Surface-State Energy-Gap Tuning', *Advanced Materials*, vol. 27, no. 10, pp. 1663–1667, Mar. 2015, doi: 10.1002/adma.201405070.
[124] J. Wang, P. Zhang, C. Huang, G. Liu, K. C.-F. Leung, and Y. X. J. Wáng, 'High Performance Photoluminescent Carbon Dots for In Vitro and In Vivo Bioimaging: Effect of Nitrogen Doping Ratios', *Langmuir*, vol. 31, no. 29, pp. 8063–8073, Jul. 2015, doi: 10.1021/acs.langmuir.5b01875.
[125] H. Huang *et al.*, 'Histidine-Derived Nontoxic Nitrogen-Doped Carbon Dots for Sensing and Bioimaging Applications', *Langmuir*, vol. 30, no. 45, pp. 13542–13548, Nov. 2014, doi: 10.1021/la503969z.
[126] Y. Zhang, X. Zhang, Y. Shi, C. Sun, N. Zhou, and H. Wen, 'The Synthesis and Functional Study of Multicolor Nitrogen-Doped Carbon Dots for Live Cell Nuclear Imaging', *Molecules*, vol. 25, no. 2, p. 306, Jan. 2020, doi: 10.3390/molecules25020306.
[127] S. Guo *et al.*, 'Fluorescent Carbon Dots Shuttling between Mitochondria and the Nucleolus for *in Situ* Visualization of Cell Viability', *ACS Appl. Bio Mater.*, vol. 4, no. 1, pp. 928–934, Jan. 2021, doi: 10.1021/acsabm.0c01408.
[128] P. Kumar, G. Bhatt, R. Kaur, S. Dua, and A. Kapoor, 'Synthesis and modulation of the optical properties of carbon quantum dots using microwave radiation', *Fullerenes, Nanotubes and Carbon Nanostructures*, vol. 28, no. 9, pp. 724–731, Sep. 2020, doi: 10.1080/1536383X.2020.1752679.
[129] X. Qin, W. Lu, A. M. Asiri, A. O. Al-Youbi, and X. Sun, 'Green, low-cost synthesis of photoluminescent carbon dots by hydrothermal treatment of willow bark and their application as an effective photocatalyst for fabricating Au nanoparticles–reduced graphene oxide nanocomposites for glucose detection', *Catal. Sci. Technol.*, vol. 3, no. 4, p. 1027, 2013, doi: 10.1039/c2cy20635h.
[130] L. Zeng *et al.*, 'The bioelectrochemical synthesis of high-quality carbon dots with strengthened electricity output and excellent catalytic performance', *Nanoscale*, vol. 11, no. 10, pp. 4428–4437, 2019, doi: 10.1039/C8NR10510C.

[131] Q.-L. Zhao, Z.-L. Zhang, B.-H. Huang, J. Peng, M. Zhang, and D.-W. Pang, 'Facile preparation of low cytotoxicity fluorescent carbon nanocrystals by electrooxidation of graphite', *Chem. Commun.*, no. 41, p. 5116, 2008, doi: 10.1039/b812420e.
[132] V. Nguyen, L. Yan, H. Xu, and M. Yue, 'One-step synthesis of multi-emission carbon nanodots for ratiometric temperature sensing', *Applied Surface Science*, vol. 427, pp. 1118–1123, Jan. 2018, doi: 10.1016/j.apsusc.2017.08.133.
[133] S. Pramanik, S. Chatterjee, G. Suresh Kumar, and P. Sujatha Devi, 'Egg-shell derived carbon dots for base pair selective DNA binding and recognition', *Phys. Chem. Chem. Phys.*, vol. 20, no. 31, pp. 20476–20488, 2018, doi: 10.1039/C8CP02872A.
[134] M. P. Sk, A. Jaiswal, A. Paul, S. S. Ghosh, and A. Chattopadhyay, 'Presence of Amorphous Carbon Nanoparticles in Food Caramels', *Sci Rep*, vol. 2, no. 1, p. 383, Apr. 2012, doi: 10.1038/srep00383.
[135] P. Suvarnaphaet and S. Pechprasarn, 'Graphene-Based Materials for Biosensors: A Review', *Sensors*, vol. 17, no. 10, p. 2161, Sep. 2017, doi: 10.3390/s17102161.
[136] Z. Gan, L. Liu, L. Wang, G. Luo, C. Mo, and C. Chang, 'Bright, stable, and tunable solid-state luminescence of carbon nanodot organogels', *Phys. Chem. Chem. Phys.*, vol. 20, no. 26, pp. 18089–18096, 2018, doi: 10.1039/C8CP02069H.
[137] A. Marinovic, L. S. Kiat, S. Dunn, M.-M. Titirici, and J. Briscoe, 'Carbon-Nanodot Solar Cells from Renewable Precursors', *ChemSusChem*, vol. 10, no. 5, pp. 1004–1013, Mar. 2017, doi: 10.1002/cssc.201601741.
[138] D. Ozyurt, M. A. Kobaisi, R. K. Hocking, and B. Fox, 'Properties, synthesis, and applications of carbon dots: A review', *Carbon Trends*, vol. 12, p. 100276, Sep. 2023, doi: 10.1016/j.cartre.2023.100276.
[139] B. N. Kumara, P. Kalimuthu, and K. S. Prasad, 'Synthesis, properties and potential applications of photoluminescent carbon nanoparticles: A review', *Analytica Chimica Acta*, vol. 1268, p. 341430, Aug. 2023, doi: 10.1016/j.aca.2023.341430.
[140] H. Zhu, X. Wang, Y. Li, Z. Wang, F. Yang, and X. Yang, 'Microwave synthesis of fluorescent carbon nanoparticles with electrochemiluminescence properties', *Chem. Commun.*, no. 34, p. 5118, 2009, doi: 10.1039/b907612c.
[141] Z. Ma, H. Ming, H. Huang, Y. Liu, and Z. Kang, 'One-step ultrasonic synthesis of fluorescent N-doped carbon dots from glucose and their visible-light sensitive photocatalytic ability', *New J. Chem.*, vol. 36, no. 4, p. 861, 2012, doi: 10.1039/c2nj20942j.
[142] R. Kumar, V. B. Kumar, and A. Gedanken, 'Sonochemical synthesis of carbon dots, mechanism, effect of parameters, and catalytic, energy, biomedical and tissue engineering applications', *Ultrasonics Sonochemistry*, vol. 64, p. 105009, Jun. 2020, doi: 10.1016/j.ultsonch.2020.105009.
[143] H. Li *et al.*, 'Fluorescent carbon nanoparticles: electrochemical synthesis and their pH sensitive photoluminescence properties', *New J. Chem.*, vol. 35, no. 11, p. 2666, 2011, doi: 10.1039/c1nj20575g.
[144] M. L. Desai, S. Jha, H. Basu, R. K. Singhal, T.-J. Park, and S. K. Kailasa, 'Acid Oxidation of Muskmelon Fruit for the Fabrication of Carbon Dots with Specific Emission Colors for Recognition of Hg^{2+} Ions and Cell Imaging', *ACS Omega*, vol. 4, no. 21, pp. 19332–19340, Nov. 2019, doi: 10.1021/acsomega.9b02730.

[145] S. Ross, R.-S. Wu, S.-C. Wei, G. M. Ross, and H.-T. Chang, 'The analytical and biomedical applications of carbon dots and their future theranostic potential: A review', *Journal of Food and Drug Analysis*, vol. 28, no. 4, pp. 678–696, Dec. 2020, doi: 10.38212/2224-6614.1154.
[146] W. Chen, G. Lv, W. Hu, D. Li, S. Chen, and Z. Dai, 'Synthesis and applications of graphene quantum dots: a review', *Nanotechnology Reviews*, vol. 7, no. 2, pp. 157–185, Apr. 2018, doi: 10.1515/ntrev-2017-0199.
[147] C. Zhou, W. Jiang, and B. K. Via, 'Facile synthesis of soluble graphene quantum dots and its improved property in detecting heavy metal ions', *Colloids and Surfaces B: Biointerfaces*, vol. 118, pp. 72–76, Jun. 2014, doi: 10.1016/j.colsurfb.2014.03.038.
[148] Y. Liu and D. Y. Kim, 'Ultraviolet and blue emitting graphene quantum dots synthesized from carbon nano-onions and their comparison for metal ion sensing', *Chem. Commun.*, vol. 51, no. 20, pp. 4176–4179, 2015, doi: 10.1039/C4CC07618D.
[149] Xie, Cheng, Liu, and Han, 'Green Hydrothermal Synthesis of N-doped Carbon Dots from Biomass Highland Barley for the Detection of Hg2+', *Sensors*, vol. 19, no. 14, p. 3169, Jul. 2019, doi: 10.3390/s19143169.
[150] M. Jayanthi, S. Megarajan, S. B. Subramaniyan, R. K. Kamlekar, and A. Veerappan, 'A convenient green method to synthesize luminescent carbon dots from edible carrot and its application in bioimaging and preparation of nanocatalyst', *Journal of Molecular Liquids*, vol. 278, pp. 175–182, Mar. 2019, doi: 10.1016/j.molliq.2019.01.070.
[151] V. N. Mehta, S. S. Chettiar, J. R. Bhamore, S. K. Kailasa, and R. M. Patel, 'Green Synthetic Approach for Synthesis of Fluorescent Carbon Dots for Lisinopril Drug Delivery System and their Confirmations in the Cells', *J Fluoresc*, vol. 27, no. 1, pp. 111–124, Jan. 2017, doi: 10.1007/s10895-016-1939-4.
[152] K. K, B. M. V, and N. P, 'A green approach for synthesis of highly fluorescent carbon dots from waste engine oil: A strategy for waste to value added products', *Diamond and Related Materials*, vol. 121, p. 108724, Jan. 2022, doi: 10.1016/j.diamond.2021.108724.
[153] A. O. Chinigar, A. Shomali, and H. Valizadeh, 'Boron/Nitrogen Co-doped carbon quantum dots as a high sensitive and selective fluorescent sensor for PO43- detection', *Org.Commun.*, vol. 13, no. 1, pp. 9–18, Mar. 2020, doi: 10.25135/acg.oc.76.20.01.1530.
[154] A. Kurdekar, L. A. A. Chunduri, E. P. Bulagonda, M. K. Haleyurgirisetty, V. Kamisetti, and I. K. Hewlett, 'Comparative performance evaluation of carbon dot-based paper immunoassay on Whatman filter paper and nitrocellulose paper in the detection of HIV infection', *Microfluid Nanofluid*, vol. 20, no. 7, p. 99, Jul. 2016, doi: 10.1007/s10404-016-1763-9.
[155] Y. Xu, D. Li, M. Liu, F. Niu, J. Liu, and E. Wang, 'Enhanced-quantum yield sulfur/nitrogen co-doped fluorescent carbon nanodots produced from biomass Enteromorpha prolifera: synthesis, posttreatment, applications and mechanism study', *Sci Rep*, vol. 7, no. 1, p. 4499, Jul. 2017, doi: 10.1038/s41598-017-04754-x.
[156] 'Infrared and Raman Characteristic Group Frequencies: Tables and Charts. 3rd ed By George Socrates (The University of West London, Middlesex, U.K.). J. Wiley and Sons: Chichester. 2001. xviii + 348 pp. $185.00. ISBN: 0-471-85298-

8.', *J. Am. Chem. Soc.*, vol. 124, no. 8, pp. 1830–1830, Feb. 2002, doi: 10.1021/ja0153520.
[157] Z. Zhu *et al.*, 'Red carbon dots: Optical property regulations and applications', *Materials Today*, vol. 30, pp. 52–79, Nov. 2019, doi: 10.1016/j.mattod.2019.05.003.
[158] I. Fiorentino *et al.*, 'Energy independent uptake and release of polystyrene nanoparticles in primary mammalian cell cultures', *Experimental Cell Research*, vol. 330, no. 2, pp. 240–247, Jan. 2015, doi: 10.1016/j.yexcr.2014.09.017.
[159] N. E. Skakkebæk *et al.*, 'Environmental factors in declining human fertility', *Nat Rev Endocrinol*, vol. 18, no. 3, pp. 139–157, Mar. 2022, doi: 10.1038/s41574-021-00598-8.
[160] A. Bruinink, J. Wang, and P. Wick, 'Effect of particle agglomeration in nanotoxicology', *Arch Toxicol*, vol. 89, no. 5, pp. 659–675, May 2015, doi: 10.1007/s00204-015-1460-6.
[161] X. Yang, Y. B. Man, M. H. Wong, R. B. Owen, and K. L. Chow, 'Environmental health impacts of microplastics exposure on structural organization levels in the human body', *Science of The Total Environment*, vol. 825, p. 154025, Jun. 2022, doi: 10.1016/j.scitotenv.2022.154025.
[162] Y. He and R. Yin, 'The reproductive and transgenerational toxicity of microplastics and nanoplastics: A threat to mammalian fertility in both sexes', *J of Applied Toxicology*, p. jat.4510, Jun. 2023, doi: 10.1002/jat.4510.
[163] Z. Wei, Y. Wang, S. Wang, J. Xie, Q. Han, and M. Chen, 'Comparing the effects of polystyrene microplastics exposure on reproduction and fertility in male and female mice', *Toxicology*, vol. 465, p. 153059, Jan. 2022, doi: 10.1016/j.tox.2021.153059.
[164] B. Liang *et al.*, 'Underestimated health risks: polystyrene micro- and nanoplastics jointly induce intestinal barrier dysfunction by ROS-mediated epithelial cell apoptosis', *Part Fibre Toxicol*, vol. 18, no. 1, p. 20, Dec. 2021, doi: 10.1186/s12989-021-00414-1.
[165] J. Hou *et al.*, 'Polystyrene microplastics lead to pyroptosis and apoptosis of ovarian granulosa cells via NLRP3/Caspase-1 signaling pathway in rats', *Ecotoxicology and Environmental Safety*, vol. 212, p. 112012, Apr. 2021, doi: 10.1016/j.ecoenv.2021.112012.
[166] S. Li, Y. Ma, S. Ye, Y. Su, D. Hu, and F. Xiao, 'Endogenous hydrogen sulfide counteracts polystyrene nanoplastics-induced mitochondrial apoptosis and excessive autophagy via regulating Nrf2 and PGC-1α signaling pathway in mouse spermatocyte-derived GC-2spd(ts) cells', *Food and Chemical Toxicology*, vol. 164, p. 113071, Jun. 2022, doi: 10.1016/j.fct.2022.113071.
[167] H. Wu, T. Xu, T. Chen, J. Liu, and S. Xu, 'Oxidative stress mediated by the TLR4/NOX2 signalling axis is involved in polystyrene microplastic-induced uterine fibrosis in mice', *Science of The Total Environment*, vol. 838, p. 155825, Sep. 2022, doi: 10.1016/j.scitotenv.2022.155825.
[168] R. An *et al.*, 'Polystyrene microplastics cause granulosa cells apoptosis and fibrosis in ovary through oxidative stress in rats', *Toxicology*, vol. 449, p. 152665, Feb. 2021, doi: 10.1016/j.tox.2020.152665.
[169] Z. Liu, Q. Zhuan, L. Zhang, L. Meng, X. Fu, and Y. Hou, 'Polystyrene microplastics induced female reproductive toxicity in mice', *Journal of Hazardous Materials*, vol. 424, p. 127629, Feb. 2022, doi: 10.1016/j.jhazmat.2021.127629.

[170] P. Mohammadi Ghalaei, J. Varshosaz, and H. Sadeghi Aliabadi, ‘Evaluating Cytotoxicity of Hyaluronate Targeted Solid Lipid Nanoparticles of Etoposide on SK-OV-3 Cells’, *Journal of Drug Delivery*, vol. 2014, pp. 1–7, Apr. 2014, doi: 10.1155/2014/746325.
[171] M. Salomé *et al.*, ‘The ID21 Scanning X-ray Microscope at ESRF’, *J. Phys.: Conf. Ser.*, vol. 425, no. 18, p. 182004, Mar. 2013, doi: 10.1088/1742-6596/425/18/182004.
[172] L. Zeng *et al.*, ‘The ovarian-related effects of polystyrene nanoplastics on human ovarian granulosa cells and female mice’, *Ecotoxicology and Environmental Safety*, vol. 257, p. 114941, Jun. 2023, doi: 10.1016/j.ecoenv.2023.114941.
[173] J. P. Abriata *et al.*, ‘Development, characterization and biological in vitro assays of paclitaxel-loaded PCL polymeric nanoparticles’, *Materials Science and Engineering: C*, vol. 96, pp. 347–355, Mar. 2019, doi: 10.1016/j.msec.2018.11.035.
[174] Y.-L. Wang, C.-M. Zheng, Y.-H. Lee, Y.-Y. Cheng, Y.-F. Lin, and H.-W. Chiu, ‘Micro- and Nanosized Substances Cause Different Autophagy-Related Responses’, *IJMS*, vol. 22, no. 9, p. 4787, Apr. 2021, doi: 10.3390/ijms22094787.
[175] M. O. Krause, ‘Atomic radiative and radiationless yields for *K* and *L* shells’, *Journal of Physical and Chemical Reference Data*, vol. 8, no. 2, pp. 307–327, Apr. 1979, doi: 10.1063/1.555594.
[176] V. Nava, M. L. Frezzotti, and B. Leoni, ‘Raman Spectroscopy for the Analysis of Microplastics in Aquatic Systems’, *Appl Spectrosc*, vol. 75, no. 11, pp. 1341–1357, Nov. 2021, doi: 10.1177/00037028211043119.
[177] V. Ludwig *et al.*, ‘Analysis by Raman and infrared spectroscopy combined with theoretical studies on the identification of plasticizer in PVC films’, *Vibrational Spectroscopy*, vol. 98, pp. 134–138, Sep. 2018, doi: 10.1016/j.vibspec.2018.08.004.

ABBREVIATION LIST

μXRM: X-ray microscopy

XRF: X-ray fluorescence

FTIR: Fourier Transform Infrared micro-spectroscopy

STXM: Scanning Transmission X-ray Microscopy

LEXRF: Low-Energy X-ray Fluorescence

CdSe-QDs: Cadmium Selenide Quantum Dots

PP: Polypropylene

PVC: Polyvinyl chloride

NPs: Nanoplastics

JRC: Joint Research Centre

ESRF: European Synchrotron Radiation Facility

CERIC: Central European Infrastructure Consortium

PIXE: Particle Induced X-Ray Emission

TEM: Transmission Electron Microscopy

NNI: National Nanotechnology Initiative

NMs: Nanomaterials

NP: Nanoparticles

PAMPs: Pathogen-Associated Molecular Patterns

LPS: Lipopolysaccharides

DNA: Deoxyribonucleic Acid

PRR: Pathogen-Recognition Receptors

TLR: Toll-like Receptors

M1: Macrophage Phenotype 1

M2: Macrophage Phenotype 2

IFN- γ: Interferon-gamma

FCγ: FC Gamma Receptor

Ag: Silver

TiO_2: Titanium Dioxide

CeO_2: Cerium Dioxide

PM: Particulate Matter

ROS: Reactive Oxygen Species

MNPs: Micro-/Nano-Plastics

MPs: Microplastics

PP: Polypropylene

PS: Polystyrene

PVC: Polyvinylchloride

PA: Nylon

CA: Cellulose Acetate

PET: Thermoplastic Polyester

ATP: Adenosine Triphosphate

SEM: Scanning Electron Microscopy

EDS: Energy Dispersive Spectroscopy

AFM: Atomic Force Microscopy

GC-MS: Gas Chromatography-Mass Spectroscopy

LDIR: Laser Direct Infrared Spectroscopy

RAMAN: Raman Spectroscopy

ZP: Zone Plate

OSA: Order-sorting aperture

CCD: Charge-Coupled Device

$CoFe_2O_4$: Cobalt ferrite

W: Tungsten

RPMI 1640: Roswell Park Memorial Institute 1640

FBS: Foeatal Bovine Serum

SiC: Silicon Carbide

PMA: Phorbol 12-Myristate 13-Acetate

RM: Resting Macrophages

PBS: Phosphate Buffered Saline, Dulbecco's formula

CM: Complete Medium

MTT: 3-(4,5-dimethylthiazol-2-yl)-2,5-diphenyl tetrazolium bromide

DMSO: Dimethyl-sulfoxide

ELISA: Enzyme-Linked Immunosorbent Assay

PFA: Paraformaldehyde

MCT: Mercury Cadmium Telluride

MIR: Mid-Infrared Region

FPA: Focal Plane Array

CO: Carbonyl Group

C=O: Carboxyl Moieties

FFAs: Free Fatty Acids

TAGs: Triacylglycerols

PCA: Principal Component Analysis

LD: Lipid Droplet

PP_M1: Macrophages Phenotype M1 treated with Polypropylene Nanoplastics

PVC_M1: Macrophages Phenotype M1 treated with Polyvinylchloride Nanoplastics

Ctrl_M1: Macrophages Phenotype M1 untreated

ν: Stretching

δ: Bending

s: Symmetric,

as: Asymmetric

PO_2^-: Phosphate group

RNA: RiboNucleic Acid

PC1: Principal Component 1

PC2: Principal Component 2

PC3: Principal Component 3

CDs: Carbon dots

CNOs: Carbon nano-onions

BN-CNOs: Boron-Nitrogen carbon nano-onions

GQDs: Graphene quantum dots

CNDs: Carbon nanodots

PDs: Polymer dots

CQDs: Carbon quantum dots

PL: Photoluminescence

HOMO: Highest Occupied Molecular Orbit

LUMO: Lowest Unoccupied Molecular Orbit

N-CDs: Nitrogen doped CDs

p-CNOs: Purified-carbon nano onions

p-(BN)CNOs: Purified-Boron Nitrogen carbon nano onions

H_2SO_4: Sulphuric acid

HNO_3: Nitric acid

$KMnO_4$: Potassium permanganate

UV-Vis: Ultraviolet-Visible

DLS: Dynamic Light Scattering

ATR: Attenuated Transmission Reflectance Micro-spectroscopy

NaOH: Sodium hydroxide

Na_2SO_4: Sodium Sulfate

$NaNO_3$: Sodium Nitrate

IRE: Internal Reflection Element

KBr: Potassium Bromide

DTGS: Deuterated TriGlycine Sulphate

Rcf: Relative centrifugal force

ζ-potential: Zeta-potential

$\gamma_{em,}$max: Fluorescence emission maximum wavelength

a.u.: Arbitrary Unit

Si_3N_4: Silicon Nitride

EDTA: Ethylenediaminetetraacetic acid

SR-XRF: Synchrotron Radiation X-ray Fluorescence

RGB: Red, Green, and Blue